Localization of Near-Surface Anomalies Using Seismic Rayleigh Waves

by

Chao Qiang (Jon) Xu

Submitted in partial fulfillment of the requirements
for the degree of Doctor of Philosophy

at

Dalhousie University
Halifax, Nova Scotia
April 2010

[students - insert a blank page here, FGS will create this page for you]

DALHOUSIE UNIVERSITY

DATE: April 15, 2010

AUTHOR: Chao Qiang (Jon) Xu

TITLE: Localization of Near-Surface Anomalies Using Seismic Rayleigh Waves

DEPARTMENT OR SCHOOL: Department of Civil and Resource Engineering

DEGREE: PhD CONVOCATION: May YEAR: 2010

Permission is herewith granted to Dalhousie University to circulate and to have copied for non-commercial purposes, at its discretion, the above title upon the request of individuals or institutions.

_____
Signature of Author

For my mother and all my loves

TABLE OF CONTENTS

LIST OF TABLES

LIST OF FIGURES

ABSTRACT

The presence of subsurface anomalies, such as cavities, faults, unknown tunnels, etc., either natural or man-made, can cause public safety hazards. The detection of these features requires the development of new methods. Seismic Rayleigh surface wave imaging is a relatively new non-destructive testing technique (NDT) which generates subsurface images without drilling boreholes into the ground, and in recent years has been widely used for soil characterization in geotechnical investigations. In the last decade, some researchers have applied the technique to near-surface imaging and showed the possibility and potential for engineering applications.

This research presents the development of a technique to process seismic Rayleigh waves to detect and image subsurface anomalies. This study conducted investigations of Rayleigh wave behaviors and developed a new strategy for Rayleigh wave isolation from raw field data. The strategy applies wavelet transforms, instead of the conventional spectral analysis of surface waves (SASW) method, or popular multichannel analysis of surface waves (MASW) techniques, to pair-channel analysis of the isolated Rayleigh wave data for dispersion calculation. Finally, a simple steady inversion technique was applied to yield shear velocity as a function of both depth and distance, and shear velocity field images (SVF), for near surface section display.

This research consists of development, computer programming, field tests, data processing and interpretation. Three sites in different scenarios were used for seismic investigations: old mining tunnels in medium dipping coal seams in Stellarton coalfield, mining cavities in steeply dipping gold-bearing veins in West Waverley Gold District and an anomaly in nearly horizontal strata in Liverpool. All these sites are in the province of Nova Scotia, Canada. The results from seismic surface wave technique introduced in this research can be evaluated by field observations, documents and borehole logs. The satisfactory interpretations and success of this investigation shows that this technique is suitable for engineering application for subsurface investigations.

LIST OF ABBREVIATIONS AND SYMBOLS USED

α	Compressional wave velocity
β	Shear wave velocity
ε	Strain
ω	Angular frequency
υ	Poisson's ratio
σ	Stress
λ	Wavelength
κ	Wavenumber
a	Scale of CWT
b	Shift of CWT
CWT	Continuous wavelet transform
E, G, K	Young's modulus, shear modulus, and bulk modulus
f-k domain	Frequency-wavenumber domain
GPR	Ground penetration radar
Hz	Hertz
MASW	Multichannel spectral analysis of surface waves
NDT	Non-destructive testing technique
P-wave	Compressional wave
SASW	Spectral analysis of surface waves
SNR	Signal to noise ratio
SSRM	Steady state Rayleigh waves method
STFT	Short time Fourier transform
SVF	Shear velocity field
S-wave	Shear wave
x-t domain	Space-time domain

GLOSSARY

Aliasing: an effect of inappropriate sampling frequency or inappropriate spacing configuration in data acquisition, in the manner of distortion or artifact of the signal reconstructed from samples, which is different than the original continuous signal

Dispersion: the dependence of phase velocity on the frequency of seismic wave

Near-surface anomaly: deviation or departure from the common property, form, or structure of a surrounding background in shallow surface

Noise: any unwanted type of energy in a signal

Phase velocity: the speed at which the phase of any one frequency component of the wave travels

Seismic Rayleigh waves: also called ground roll in seismic exploration, one type of surface waves traveling as ripples with motions similar to those of waves on the ocean surface

Shear velocity field: an imaging of shear wave velocity in depth and offset plane

Short time Fourier Transform: a Fourier-related transform used to determine the sinusoidal frequency and phase content of local sections of a signal as it changes over time

Wavelet: a small localized wave of energy concentrated in time or space

Wavelet transform: representation of a signal by wavelets, which localizes a signal both in space and scaling (or frequency)

Wavenumber: a wave property having SI units of reciprocal metres (m^{-1}), inversely related to wavelength having SI units of metres.

ACKNOWLEDGEMENTS

I would like to extend thanks and gratitude to the people who have offered help and collaborated with me in the work represented in this thesis.

First, thanks go to my supervisor Dr. Stephen Butt. No words can express my gratitude to him. He directed me into an amazing world of non-destructive imaging that has great promise in engineering practice. His knowledge, guidance, academic attitude, continuous encouragement and support are of the utmost importance for my research and the completion of this thesis. I am lucky to have worked with him and his association will definitely benefit my career.

Dr. Patrick Ryall from the Dalhousie Earth Sciences Department has been giving his constant invaluable support since I met him from his Applied Geophysics Class when I studied for my M.A.Sc program. He transmitted not only geophysical knowledge but also scientific attitude. Many times he went to field tests together with me for microgravity surveying, seismic investigations, data processing and interpretation. He contributed a lot of time to my research proposal critique and my thesis revision.

Dr. Craig Lake helped with review of geotechnical knowledge and practice, offered me the chance of understanding the potential application of seismic techniques to geotechnical engineering, and gave me many helpful recommendations about the thesis and future work.

I enjoyed the time working together in the field with colleagues William Pay, Mathew Vance, Lucas Dickie, Brad Baxter and Matthew Hilladay for data acquisition. We discussed, cooperated and learned from each other. At the same time, we developed knowledge and skills. They have contributed a lot to field work and are acknowledged here.

Technologists Mr. Darrell Adams in Mineral Resources, Mr. Chris Hill in Electrical Engineering and Mr. Charles Walls in Earth Science gave a lot help in seismic equipment maintenance and modifications. Many administrative staff in Department of Civil and Resource Engineering, Graduate Studies of Engineering and the Department of Earth Science also gave me a lot of useful help.

This research was supported by C-CORE, Conestoga Rover Associates (CRA), NSERC, Inspec-Sol, the Atlantic Innovation Fund, Pioneer Coal Ltd., Subsurface Imaging Technology Inc. (SIT) and the Natural Sciences and Engineering Research Council of Canada. All these collaborators are sincerely appreciated.

CHAPTER 1: INTRODUCTION

This chapter gives the background and motivation of the thesis and specifically defines the problems that lead to and will be solved in this research. It reviews site investigation techniques for geotechnical engineering and the development of seismic surface wave methods. It presents strategies to achieve these objectives in this research and development. It also pinpoints the specific contribution and scientific value of the thesis. The outline of this dissertation is also presented in this chapter.

Motivation and Objectives

An anomaly is defined as deviation or departure from the common order, form, or rule of a surrounding background. In this research, the anomaly is used to include: geological structures, natural or man-made cavities, tunnels and sinkholes in the shallow subsurface. These anomalies impose significant impact on human living and engineering practice.

It is a standard procedure in petroleum reservoir engineering practice to use seismic exploration for potential reservoir identification before drilling boreholes. A processed seismic reflection image represents a geological section, on which borehole logs can be added for further validation and more detailed information. Without seismic reflection exploration, it would be impractical to identify suitable targets for drilling in oil and gas exploration. In geotechnical engineering practice, one of the most important steps, site investigation, includes drilling holes, laboratory tests and in-situ tests. Either borings or in-situ tests are done at discrete selected locations, that is, these tests are not continuous,

so the interpretation of the data from these techniques might be misleading. For example, a boring close to a fault might not show any information about the fault. Therefore, if soil variation is significant, which is common in the shallow subsurface, or some anomaly such as cavities exists, these conventional techniques in geotechnical engineering will give rise to inestimable uncertainty and risk.

Although several geophysical techniques have come into practice, most of these geophysical methods are only suitable for specific cases. To date, geophysical techniques for site investigation in geotechnical engineering are not well accepted or popular in geotechnical engineering practice.

This research is motivated by the need to develop and implement robust techniques for site investigation and localizing subsurface anomalies. This research aims at developing technology that can generate accurate high-resolution images of subsurface anomalies with inexpensive and rapid operation. The techniques start with seismic data analysis both in the space-time domain (x-t domain) and the frequency-wavenumber domain (f–k domain). A strategy of filtering is then put forward and a filter package is designed for Rayleigh wave isolation. Next, continuous wavelet transforms are applied for dispersion calculation, and finally these dispersions are mapped into shear wave velocity vs. depth along offset to produce 2-D shear velocity field images (SVF). This technique is then validated by several field trials covering different subsurface situations.

Optimization of field data acquisition configuration is considered, and a strategy of minimization of imaging uncertainty is also discussed in this thesis.

The software is developed in Matlab by the author. Computer programs include:

i) Field data transfer and seismic data demultiplexing,

ii) Superposition of several shot lines to form a long seismic section,

iii) Shot gather display in conventional variable-area amplititude and new adjustable 3-D section, and SVF display function,

iv) Seismic data analysis such as *x-t* filtering, bandpass frequency filtering and *f-k* filtering, bedrock imaging by plus-minus refraction method, etc.

v) Dispersion calculation using optional continuous wavelets, and SVF mapping

Discussion of requirements and limitations will be covered in different steps of this study. Refraction and back scattering is also studied as complements to this seismic surface wave method.

Overview of Techniques for Site Investigation in Geotechnical Engineering

Most human activities are limited to the surface and shallow subsurface on the Earth. Mining, civil and environmental engineering require subsurface site investigation for a proposed engineering field. Subsurface site investigation is one of the most fundamental tasks of geotechnical engineering.

To meet the requirements of bearing capacity and settlement of a foundation, slope stability of an open pit, ground control for underground mining, or any other engineering requirements, different available ex-situ testing and in-situ testing techniques are widely used to determine i) the locations and thicknesses of the soil strata, ii) the location of the

groundwater table as well as any other groundwater related characteristics, iii) the locations of the bedrock and, iv) special problems and concerns such as subsurface cavities.

Conventional Techniques for Site Investigation

Conventional site investigations include site exploration, laboratory testing and in-situ testing. Brief introductions to these techniques are given here.

Site exploration employs drilling exploratory borings and/or digging exploratory trenches to determine soil stratigraphic and bedrock profiles, and to obtain samples. Exploratory borings and sampling for laboratory tests are expensive and time consuming. A rough guideline for average arrangement of exploratory borings for medium sized buildings is one borehole per 200 – 400 m^2 (Coduto, 2001). Borings generally should go down at least to such a depth that the change in vertical effective stress due to the new construction is less than 10% of the original vertical effective stress. If fill is present, the borings will have to go below the original ground surface. If soft soils are present, the borings must reach firmer soils below. For heavy structures, at least some of the borings should be carried down to bedrock (Coduto, 2001).

Laboratory testing, or ex-situ testing, is designed to determine the relevant engineering properties of the soil by testing soil or rock samples obtained from the field at a soil mechanics laboratory. In the laboratory, several routine tests are performed on soil samples to ascertain the general characteristics including moisture content, density,

plastic limit and liquid limit, grain-size, shear strength consolidation, Young's modulus E, shear modulus G, bulk modulus K, Poisson's ratio υ, etc.

In-situ testing techniques are designed for field tests and soil evaluation. These techniques are conducted at the field sites. In-situ tests are especially useful in soils that are difficult to sample such as clean sand. The commonly used methods are standard penetration test (SPT), cone penetration test (CPT) and vane shear test (VST). Pressuremeter test (PMT) and dilatometer test (DMT), which are more complicated but more accurate, are becoming popular in practice. Empirical corrections and calibrations are usually used to convert in-situ testing results to appropriate engineering properties, which can be used to estimate whether the engineering property requirements are met at a specific site.

The site investigation is time consuming due to many different phases, and always involves uncertainty and risk. The main reason for the uncertainty is that only a few spots are selected for sampling or testing and then used to estimate and characterize the whole site. Soil variation contributes uncertainty in site investigation. In an area of complicated geological history, it is possible that some hazardous subsurface anomalies, such as subsurface cavities, fault zones, etc. may not be detected, with dangerous consequences. The other reason is that empirical estimation is usually used to determine the engineering properties of the investigated site. Measurement errors also give rise to uncertainty to geotechnical parameters. Although the uncertainty and risk can be reduced by making a pattern of much denser borings, retrieving more samples and conducting more tests, there is no way of totally eliminating the uncertainty, and moreover, these endeavors will

significantly increase investigation costs. It is always a challenge to determine the most cost-effective site investigation.

Geophysical Techniques for Site Investigation

With regards to site investigation, some non-destructive geophysical techniques have come into geotechnical engineering practice, such as the seismic refraction method, electrical resistivity method, gravity method, ground penetration radar (GPR), seismic surface wave method, and so on.

Seismic refraction

Seismic refraction is a relatively inexpensive geophysical method for finding the depths to approximately horizontal seismic interfaces on all scales of site investigations. In practice, it is a powerful approach for bedrock profiling. This method exploits a particular case of refraction in which the refracted waves travel along an interface and then propagate back to the surface as head waves. This occurs at a subsurface interface where the upper formation has a lower wave velocity than the lower formation, which is typically soil-bedrock interface. Figure 1.1 shows the principle of seismic refraction. The incident wave traveling at V_1 strikes the refractor at a critical angle i_c such that the refracted waves travels along the interface at velocity V_2 and then are refracted back to the upper layer at the same critical angle i_c.

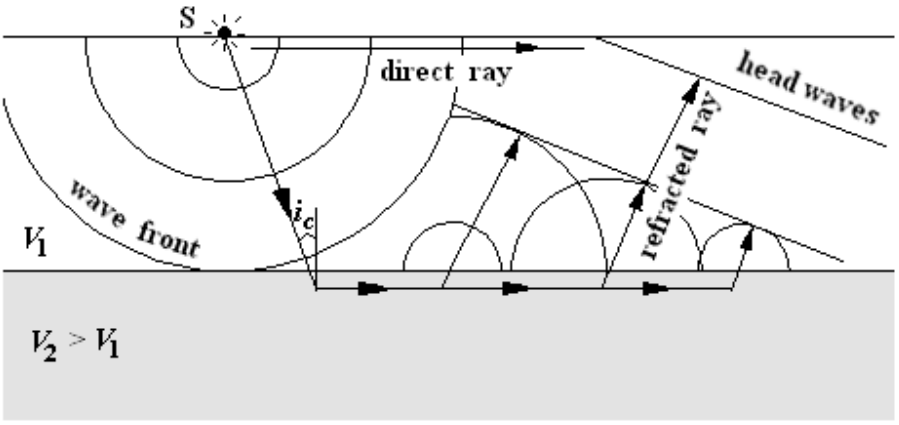

Figure 1.1 Schematic illustration shows wave fronts and head waves: the ray paths of the incident wave traveling at V_1 strike the refractor at a critical angle i_c, and the refracted waves travel along the interface at velocity V_2, then are refracted back to the upper layer at the same critical angle i_c (after Mussett and Khan, 2000).

Figure 1.2 is a travel-time seismic refraction record. At short distances, the direct arrivals come first and then at greater distances the refracted waves arrive earlier than the direct waves because the refractor has a greater velocity V_2 than the top layer V_1. The black dots show the corresponding breaks picked from the direct and refracted waves. From the travel-time curves, there are three important parameters, the slopes of the best-fit lines of direct arrivals and refracted waves, which are respectively reciprocals of V_1 and V_2, and the intercept on the time axis t_i. All these three parameters can be measured from the time-distance curves.

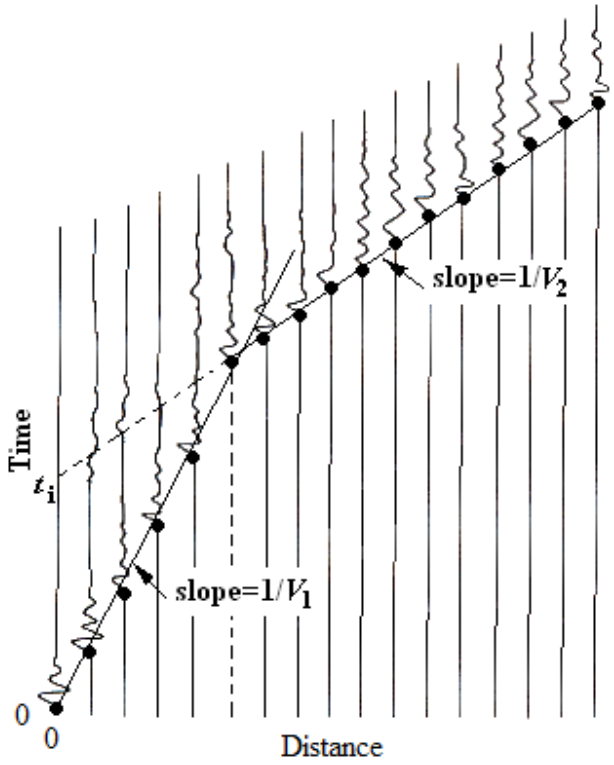

Figure 1.2 Travel-time record and first arrival picking for direct waves and head waves from the single horizontal refractor

The depth of the bedrock, *z,* can be determined from Equation (1.1).

$$z = \frac{V_1 V_2}{2\left(V_2^2 - V_1^2\right)^{1/2}} t_i \qquad (1.1)$$

In practice, an overall observational scheme, which often includes on-end shots into individual reversed profile lines, is usually applied to obtain refraction coverage along a survey line.

Due to the dependence of seismic velocity on the elasticity and density of the material through which the energy is passing, seismic refraction surveys provide a measure of material strengths and so can consequently be used as an aid in assessing bedrock quality. The technique has been successfully applied to mapping depth to base of backfilled

quarries, depth of landfills, thickness of overburden and the topography of groundwater. However, for a medium of stiffness decrease with depth, or velocity decrease with depth, there is no refraction. In the case of a sandwich medium with weak layer in the middle, the middle layer will not be detected resulting in an incorrect interpretation of refraction events (Ryall 2004).

Electrical resistivity method

Electrical resistivity is an intrinsic property of all materials. It is defined as the resistance in ohms between two opposite faces of a unit cube of a material. The electrical resistivity method involves the measurement of the apparent resistivity of soils and rocks as a function of position. The resistivity of soil is a complicated function of porosity, permeability, ionic content of the pore fluids, and clay mineralization.

Current is injected into the earth through a pair of current electrodes, and the potential difference is measured between a pair of potential electrodes, which is used to compute apparent resistivity at an assumed depth based on the electrode arrangement.

The application includes determination of overburden thickness, water table, clay layers and other highly conductive subsurface features. However, the resistivity is subject to so many factors such as water content, salinity, temperature, porosity, clays, metallic minerals and so on that it is often difficult to interpret the results unambiguously. The difficulty in interpretation of resistivity limits the application of this method.

Gravity method

The gravitational acceleration of the Earth g, or gravitation attraction on a mass on the Earth' surface is given:

$$g = G\frac{M}{R^2} \qquad (1.2)$$

where G = gravitational constant ($6.67\times10^{-11}m^3kg^{-1}s^{-2}$), R = the Earth radius (6370 km) and M= mass of the Earth.

Because the Earth is not homogeneous, the gravity is not constant. The gravity changes with geology and location. After the effects of drift and influence of latitude, elevation and terrain have been removed, a Bouguer gravity profile related to geological structure is usually produced. Overburden depth, thin sheets, slabs, dikes, faults, buried objects and cavities in the near surface will affect gravity profile. Figure 1.3 shows gravity effects of a buried sphere (a) and a cavity (b) (Ryall 2004).

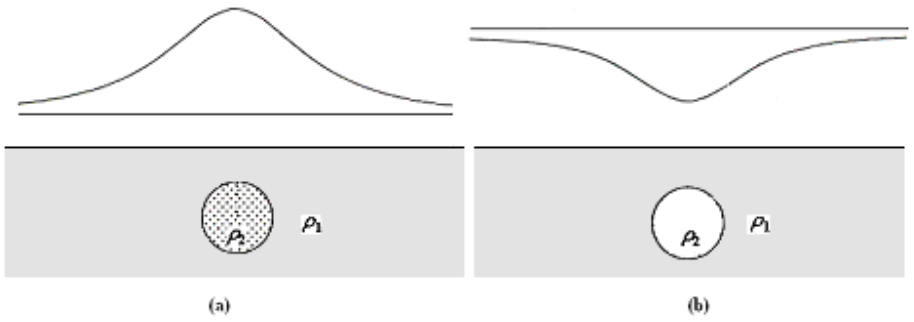

Figure 1.3 Gravity profiles corresponding with density variations: (a) $\rho_2 > \rho_1$; (b) $\rho_2 < \rho_1$

Some success with locating near surface cavities using gravity method has been reported (Butt et al, 2005, Xu and Butt, 2006).

However, calculated gravity anomalies from small-scale near surface structures may be near or below the limits of resolution of the gravimeters. Besides this limitation, in an area of complicated geology and topography, there are so many factors affecting the gravity that it is difficult to make accurate corrections and differentiate all these factors form gravity profile. In addition, elevation correction requires accurate elevation survey for each station, at which the gravity is measured.

Ground penetration radar (GPR)

GPR is the highest frequency (ranging from 25 to 2000 MHz) electromagnetic method (EM). Like seismic reflection, it depends on reflection of a pulse of waves. When radar waves meet an interface with sharp conductivity contrast, there will be strong reflection. GPR measures the two-way times (TWT). It uses pulses of very high frequency e-m waves to reflect from the interface of electrical discontinuities to produce a section analogous to a reflection seismic section. The wavelength ranges from a few tens centimetres to a few metres depending on both the frequency used and the medium velocity. The high frequency pulses produce good resolution, but at the cost of reduced penetration.

The penetration of GPR is a concern for its application. The penetration depth of GPR depends on the frequency and the electrical conductivity of the medium being studied. GPR can penetrate up to tens of metres in pure limestone, dry sand, or sand saturated

with fresh water of low conductivity, but only centimetres into damp clay or salty water of high conductivity.

GPR offers high resolution, but unfortunately, its limit in conductivity-dependent penetration limits it usefulness, especially in high conductivity soil and rocks.

Trial GPR surveys, which were done as part of this investigation, appeared to be limited by these factors and were not pursued further.

Overview of Seismic Surface Wave Methods

The surface wave methods are a novel geophysical approach for in-situ measurements of mechanical properties of a medium based on the dynamic information of Rayleigh waves when they propagate in a medium.

The development of surface wave methods has been long and slow. Rayleigh waves were first described in the second half of the 19th century (Rayleigh, 1887) as solution of the free vibration problem for an elastic halfspace. In the 1950s, with the discovery of dispersive property of Rayleigh waves in layered media, the use of surface waves for the characterization of the subsurface was introduced by seismologists for the investigation of the Earth's crust and upper mantle (Thomson 1950, Ewing et al 1957, Haskall 1953), and the geotechnical scale application was promoted in 1980s when the SASW method was introduced by Nazarian and Stokoe (1984). Since then, with improving computer technology, surface wave methods have entered a record-breaking period when researchers, engineers, mathematicians and geophysicists are working on surface waves,

which previously had been considered only as an undesired noise called ground roll, as a potential tool for underground explorations (Szelwis and Behle 1984, Mokhtar et al 1988, Park et al 1999, Lai and Rix 1999, Foti 2000, Xia et al 2004, Nasseri-Moghaddam et al 2004, Xu and Butt 2006, Bohlen and Saenger 2006, Nasseri-Moghaddam et al 2007, Xu et al 2008, Tallavo et al 2009). Some researchers work on optimization for field configuration, some on surface seismic data processing, some on numerical modeling and some on inversion and explanation. Multi-channel analysis of surface waves (MASW), which has the merits of good SNR and saving time in field data acquisition, reliable processing through transform mapping and simultaneous inversion, is the state-of-the-art surface wave technique. MASW is of the most interest among researchers and has been widely used in soil characterizations.

Anomaly Detection - Challenge in Geotechnical Engineering

As stated earlier, there are many types of near-surface anomalies and some of these pose hazard to people and overlaying infrastructure. Mine subsidence, due to collapse of overburden into underground mined spaces, has not only been a concern for civil and environmental engineering, but might also present potential hazards to public safety. Construction in these areas requires subsurface maps for detailed information of the anomaly distributions. The extraction of ore removes support from the overlying strata causing them to sag into the created void space (Figure 1.4). The sag is propagated upward toward the surface, with the maximum surface subsidence no greater than the thickness of the ore mined. However, the lateral extent of subsidence at the surface is

greater than the extent of underground mining. The surface position of the boundary between areas of subsidence and no subsidence is defined by the "angle of draw." This is the angle between a vertical line drawn upward to the surface from the edge of the underground opening and a line drawn from the edge of the opening to the point of zero surface subsidence. The angle of draw usually varies from 25° to 35°. The larger the angle of draw the greater will be the basin on the surface in which subsidence should occur. Subsidence usually occurs gradually when it is concurrent with mining. After cessation of mining, subsidence may continue to occur in a steady, gradual manner, or it may stop for a period, to be followed by failure at some later date.

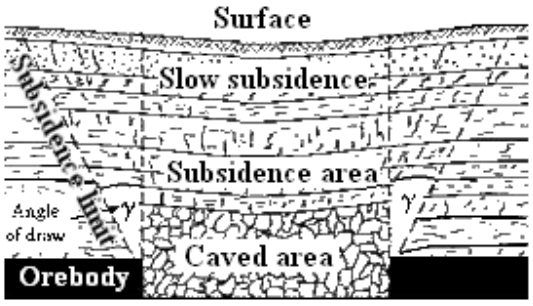

Figure 1.4 Development of mine subsidence (after Qiu, 1986)

The presence of subsurface cavities often leads to restrictions in land utilization and can pose a variety of problems for both the current and future users of that land. Responsible engineering practice requires the positive identification and location of cavities prior to final engineering design and construction. In some cases, confirmation of features marked on existing plans and maps is all that is required, but often it is necessary to

undertake a broader based search to determine the sub-surface structure, especially at previously undeveloped sites.

Mine subsidence is common in Nova Scotia and most provinces of Canada. Nova Scotia has a long mining history of almost 200 years. Gold, coal and copper were mined extensively for more than 150 years. The Canadian Environmental Law Association (CELA) estimates that there are more than 300 abandoned mines in Nova Scotia, most of which have not been examined by field inspection or tested for physical and/or chemical stability. In Canada there are more than 10,000 abandoned mines and 6,000 abandoned tailing sites. It is likely that in historical coal mining areas, there are many more undocumented or 'bootleg' mines that are typically shallow (less than 30 m deep), unmarked and pose a significant hazard for ground subsidence.

In slope stability studies, the most common failure types are plane failure, wedge failure and rotational failure resulting from one or more weak planes or layers. It is crucial to localize these weak planes or layers in slope stability analysis and its safety evaluation.

Clearly, there is an urgent need for an inexpensive, reliable, rapid and robust technology to perform this non-destructive evaluation during the initial environmental evaluation of abandoned mine sites, generally termed targets in this research.

Based on the initial comparison by Aminnedjad and Butt (2003), seismic Rayleigh wave methods were determined to have the best potential to meet the research objectives of near-surface anomaly detection since they do not require boreholes to be drilled and can provide seismic information that can be applied to geotechnical assessment, such as wave velocities. The limited depth penetration of surface wave method (30 to 40 metres) is not

a significant limitation since most subsidence related problems are due to the shallow workings within this depth limit. Surface waves can be generated with simple sledgehammer, a weight drop, or by using a powerful bulldozer. Refraction Microtremor (ReMi) method has been reported to be a faster and better method to penetrate to 100 metres depth in term of 1-denmention shear velocity profile (Louie 2001). This technique is limited to horizontal layers, and also has limitations identifying boundaries between soil layers within the earth and therefore may miss thin layers of anomalous velocity. As a result, this method may not work well for void localization purpose. Xu and Butt (2006) developed two surface wave approaches, time delay mapping (TDM) and shear velocity mapping (SVM), for detection and imaging of the targets. Later field tests showed these methods are sensitive to noise in urban areas or near traffic, and it is time consuming and subjective to remove this noise. Based on these previously developed techniques, this research focuses on improvement and develops a potential practical solution.

Contents of Research and Thesis Outline

To accomplish the defined objectives for this investigation, an intensive literature review (Chapter 2) was conducted on elastic wave equation, plane waves and Rayleigh waves. This part derives the relationship between Rayleigh wave velocity and shear wave velocity, explain how Rayleigh wave velocities are associated with engineering properties and the principle of Rayleigh wave imaging. Rayleigh wave behaviors in vertically layered media, lateral variations and anomalies will be emphasized. In Chapter 3, Filtering techniques and filter designs are given. Different filtering strategies are

applied in different stages of seismic data processing to pick out Rayleigh waves. In Chapter 4, seismic data analysis is conducted in *x-t* domain and *f-k* domain. Dispersion phenomena is discussed and numerical modeling will be applied for vertically layered media. Anomaly effects will be presented and discussed. Chapter 5 relates methodology including wavelet techniques, dispersion estimation using wavelet transforms, inversion procedure and 2-D SVF mapping method. Chapter 6 presents seismic data analysis, processing and imaging of several field trails using the approaches described in Chapters 4 and 5. Refraction method for bedrock imaging and backscattering for anomaly detection would also be applied if possible. Chapter 7 draws some conclusions and makes recommendations for future work.

Special Contributions

There are three main parts in this section. The first is a comprehensive investigation of the anomaly detection problem in subsurface imaging. Field studies were set in a variety of geological conditions. The second contribution is to apply the filtering strategies for Rayleigh wave isolation. Based on literature review, there have not been any publications which use Rayleigh waves from a seismic section in the way of this research.

The third is pair-channel based dispersion estimation for multichannel seismic data. In MASW methods, most researchers apply transform techniques (*f-k*, p-τ, waveform transform) to derive a dispersion curve from one shot gather and assume that stacking a multichannel gather improves the reliability and stability of the calculated dispersion curve. This is correct for vertically layered media without lateral variation, dipping or

anomaly. However, when any adverse condition (lateral variation, dipping or anomaly) exists, it is impossible for the conventional MASW method to give a dispersion curve that can represent the physical section covered by the multichannel geophone spread. This limitation has been addressed in this thesis.

CHAPTER 2: SEISMIC WAVE PROPAGATION AND RAYLEIGH WAVES

This chapter introduces the theory of seismic wave propagation and the properties of seismic Rayleigh waves. Seismic waves are generally grouped into two main categories: body waves and surface waves. Surface waves are generated only in presence of a free boundary and they can be essentially of two types: Rayleigh waves and Love waves. Rayleigh waves are always generated when a free surface exists in a continuous body, while Love waves can be generated only in presence of a soft superficial layer over a stiffer halfspace and they are produced through energy trapping in the softer layer for multiple reflections.

Wave Propagation in Linear Elastic Medium

The theory of elasticity, Hooke's law and Newton's second law can be used to derive a general wave equation.

The relation between stresses and strains is the fundamental principle of theory of elasticity. Stress is defined as force per unit area, and strains are change in shape and dimension when an elastic body is subjected to stresses. Figure 2.1 represents the stresses acting on each of the six faces of a small element of volume.

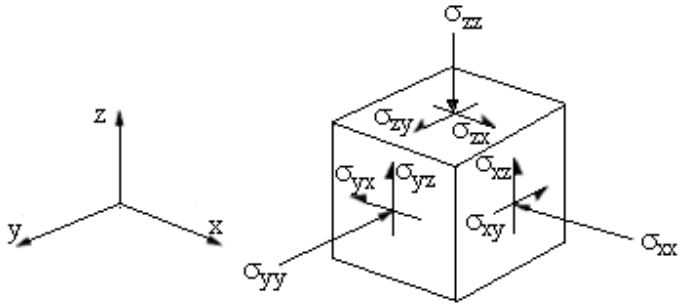

Figure 2.1 Components of stresses

The stresses can be resolved into six components. Subscripts denote Cartesian axes e.g. σ_{xy} denotes a stress parallel to y axis acting on the surface perpendicular to x axis. A stress with the same two subscripts is a normal stress; otherwise, it is a shear stress. Correspondingly, we take ε_{xx} ,ε_{yy} ,ε_{zz} separately for the normal strain in the *x, y and z* directions, and ε_{xy} , ε_{zx} , and ε_{zy} for shear strains, then strains can be defined as Equation (2.1) in terms of derivatives of the displacement *u*. The elementary strains can be expressed as:

$$\varepsilon_{xx} = \frac{1}{2}\left(\frac{\partial u_x}{\partial x} + \frac{\partial u_x}{\partial x}\right) = \frac{\partial u_x}{\partial x}$$
$$\varepsilon_{yy} = \frac{1}{2}\left(\frac{\partial u_y}{\partial y} + \frac{\partial u_y}{\partial y}\right) = \frac{\partial u_y}{\partial y}$$
$$\varepsilon_{zz} = \frac{1}{2}\left(\frac{\partial u_z}{\partial z} + \frac{\partial u_z}{\partial z}\right) = \frac{\partial u_z}{\partial z}$$

$$\varepsilon_{xy} = \frac{1}{2}\left(\frac{\partial u_y}{\partial x} + \frac{\partial u_x}{\partial y}\right)$$
$$\varepsilon_{zx} = \frac{1}{2}\left(\frac{\partial u_z}{\partial x} + \frac{\partial u_x}{\partial z}\right) \qquad (2.1a)$$
$$\varepsilon_{zy} = \frac{1}{2}\left(\frac{\partial u_y}{\partial z} + \frac{\partial u_z}{\partial y}\right)$$

or

$$\varepsilon_{ij} = \frac{1}{2}\left(u_{i,j} + u_{j,i}\right) \qquad (2.1b)$$

In addition to strains, the element is subjected to simple rotation about the three axes. The rotation is given by:

$$\theta_x = \frac{1}{2}\left(\frac{\partial u_z}{\partial y} - \frac{\partial u_y}{\partial z}\right)$$
$$\theta_y = \frac{1}{2}\left(\frac{\partial u_x}{\partial z} - \frac{\partial u_z}{\partial x}\right) \qquad (2.2)$$
$$\theta_z = \frac{1}{2}\left(\frac{\partial u_y}{\partial x} - \frac{\partial u_x}{\partial y}\right)$$

Hooke's law states the relationship between stresses and stains as $\sigma_{ij} = \alpha_{ijkl}\varepsilon_{kl}$, where α is a 4^{th} order tensor. In general, Hooke's law leads to complicated relations for a system with several stresses, but when a medium is isotropic, it can be expressed in a simple way

$$\begin{aligned} \sigma_{ii} &= \lambda\Delta + 2\mu\varepsilon_{ii} \\ \sigma_{ij} &= \mu\varepsilon_{ij} \quad \text{i} \neq \text{j} \end{aligned} \tag{2.3}$$

where i, j = x, y, z; λ, μ = Lamé constants, and Δ = change in volume per unit volume called the dilatation represented by

$$\begin{aligned} \Delta &= \varepsilon_{xx} + \varepsilon_{yy} + \varepsilon_{zz} \\ &= \frac{\partial u_x}{\partial x} + \frac{\partial u_y}{\partial y} + \frac{\partial u_z}{\partial z} \end{aligned} \tag{2.4}$$

For i≠j, the relation between stresses and strains can be written as $\varepsilon_{ij}=\sigma_{ij}/\mu$. It is evident that the larger μ, the smaller ε_{ij}. Therefore μ is a measure of the resistance to shear strains and is often referred to as shear modulus.

Besides Lamé constants, other elastic constants are also often used to express stress-strain relationship such as Young's modulus E, Poisson's ratio υ, bulk modulus K. Table 2.1 lists all these elastic constants and Table 2.2 summarizes the most widely used pairs of parameters with the relative cross relationships.

Newton's second law of motion states that the force equals the mass times the acceleration, so along any direction of the three axes, we have

$$\rho\frac{\partial^2 u}{\partial t^2} = \frac{\partial \sigma_i}{\partial x} + \frac{\partial \sigma_i}{\partial y} + \frac{\partial \sigma_i}{\partial z} \tag{2.5}$$

where σ_i is the stress tensor and i is any of x, y or z, u is the displacement of a particle of the medium, and ρ is the density.

Table 2. 1 Definition of elastic constants (Foti 2000)

Name	Symbol	Definition	Notes
Young's modulus	E	$\frac{\text{longitudinal stress}}{\text{longitudinal strain}}$	Free transversal deformation
Shear modulus	G	$\frac{\text{shear stress}}{\text{shear strain}}$	
Poisson's ratio	υ	$\frac{\text{longitudinal strain}}{\text{transversal strain}}$	Free transversal deformation
Bulk modulus	K	$\frac{\text{differential change in pressure}}{\text{volumetric strain}}$	

Table 2. 2 Relationship between elastic constants (Foti, 2000)

	λ, μ	G, υ	E, υ	K, G
λ	λ	$\frac{2G\upsilon}{1-2\upsilon}$	$\frac{\upsilon E}{(1+\upsilon)(1-2\upsilon)}$	$K-\frac{2}{3}G$
$\mu \equiv G$	μ	G	$\frac{E}{2(1+\upsilon)}$	G
K	$\frac{(3\lambda+2\mu)}{3}$	$\frac{2G(1+\upsilon)}{3(1-2\upsilon)}$	$\frac{E}{3(1-2\upsilon)}$	K
E	$\frac{\mu(3\lambda+2\mu)}{\lambda+\mu}$	$2(1+\upsilon)G$	E	$\frac{9KG}{3K+G}$
υ	$\frac{\lambda}{2(\lambda+\mu)}$	υ	υ	$\frac{3K-2G}{2(3K+G)}$

Differentiating equation 2.4 and substituting in 2.5 can eliminate stresses and express strains in term of displacement: set body forces equal to zero and get the Navier's equation of motion:

$$\mu\left(\frac{\partial^2 \boldsymbol{u}_x}{\partial \boldsymbol{x}^2}+\frac{\partial^2 \boldsymbol{u}_x}{\partial \boldsymbol{y}^2}+\frac{\partial^2 \boldsymbol{u}_x}{\partial \boldsymbol{z}^2}\right)+(\lambda+\mu)\left(\frac{\partial^2 \boldsymbol{u}_x}{\partial \boldsymbol{x}^2}+\frac{\partial^2 \boldsymbol{u}_y}{\partial \boldsymbol{x}\partial \boldsymbol{y}}+\frac{\partial^2 \boldsymbol{u}_z}{\partial \boldsymbol{x}\partial z}\right)=\rho\frac{\partial^2 \boldsymbol{u}_x}{\partial \boldsymbol{t}^2}$$
$$\mu\left(\frac{\partial^2 \boldsymbol{u}_y}{\partial \boldsymbol{y}^2}+\frac{\partial^2 \boldsymbol{u}_y}{\partial \boldsymbol{x}^2}+\frac{\partial^2 \boldsymbol{u}_y}{\partial z^2}\right)+(\lambda+\mu)\left(\frac{\partial^2 \boldsymbol{u}_y}{\partial \boldsymbol{y}^2}+\frac{\partial^2 \boldsymbol{u}_x}{\partial \boldsymbol{x}\partial \boldsymbol{y}}+\frac{\partial^2 \boldsymbol{u}_z}{\partial \boldsymbol{y}\partial z}\right)=\rho\frac{\partial^2 \boldsymbol{u}_y}{\partial \boldsymbol{t}^2} \quad (2.6a)$$
$$\mu\left(\frac{\partial^2 \boldsymbol{u}_z}{\partial z^2}+\frac{\partial^2 \boldsymbol{u}_z}{\partial \boldsymbol{x}^2}+\frac{\partial^2 \boldsymbol{u}_z}{\partial \boldsymbol{y}^2}\right)+(\lambda+\mu)\left(\frac{\partial^2 \boldsymbol{u}_z}{\partial z^2}+\frac{\partial^2 \boldsymbol{u}_x}{\partial \boldsymbol{x}\partial z}+\frac{\partial^2 \boldsymbol{u}_y}{\partial \boldsymbol{y}\partial z}\right)=\rho\frac{\partial^2 \boldsymbol{u}_z}{\partial \boldsymbol{t}^2}$$

or compactly in vector notation as

$$\mu\nabla^2 u+(\lambda+\mu)\frac{\partial\Delta}{\partial x_i}=\rho\frac{\partial^2 u}{\partial t^2} \quad (2.6b)$$

where $\nabla^2 \boldsymbol{u}$ = Laplacian of $u=\left(\frac{\partial^2 u}{\partial x^2}+\frac{\partial^2 u}{\partial y^2}+\frac{\partial^2 u}{\partial z^2}\right)$, x_i= *x, y* or *z* respectively for *i* = *x, y* or *z* axis.

Equations (2.6) are called the general wave propagation equation, which represents a system related with three elastic constants (ρ, λ, μ). For practical purposes in seismology these parameters are not constants; in the Earth they are functions of position *r* and vary significantly, in particular with depth.

Seismic Waves

Solution of the general wave equation 2.6 yields a number of wave types. The first category is body waves of which they are two types - compressional waves and shear waves. Brown and Mussett (1981) gave detailed classification of seismic waves in their book. Compressional P-wave is the fastest travelling of all seismic waves. The particle motion of P-waves is extension (dilation) and compression along the propagating

direction. P-waves travel through all media that support seismic waves. Airwaves or noise in gasses, including the atmosphere, are P-waves. Compressional waves in fluids, e.g. water and air, are commonly referred to as acoustic waves. Particle motion associated with the passage of the P-wave involves oscillation about a fixed point in the direction of wave travel (Figure 2.2).

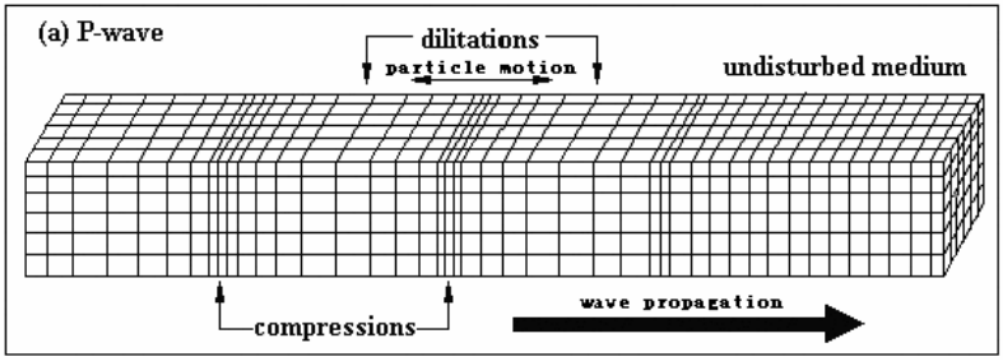

Figure 2.2 Compressional Waves (after Brown & Mussett, 1981)

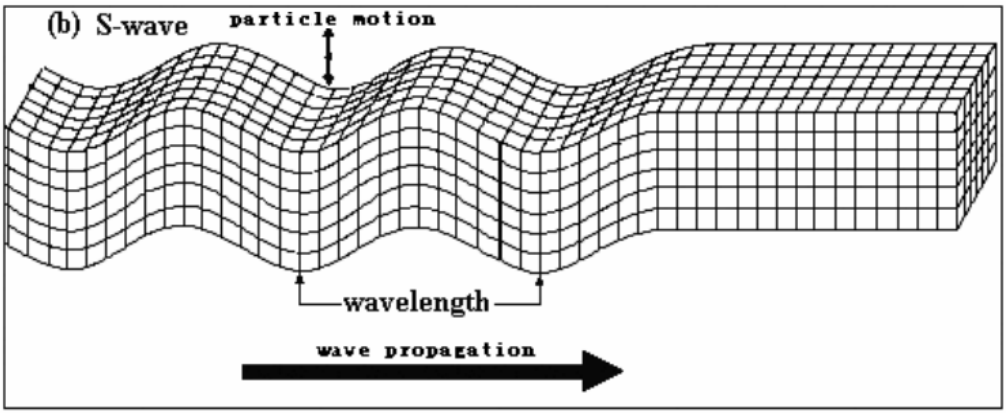

Figure 2.3 Shear Waves (after Brown & Mussett, 1981)

Transverse or Shear wave (S-wave) travels slightly slower than P-waves in solids. S-waves have particle motion perpendicular to the propagating direction, and can only

transit in material that has shear strength. S-waves do not exist in liquids and gasses, as these media have no shear strength. Figure 2.3 shows individual particle motion involves oscillation about a fixed point in a plane at right angles to the direction of wave travel.

The second category of elastic waves are surface waves. Surface waves are generated only in the presence of a free boundary and they can be essentially of two types: Rayleigh waves and Love waves. Rayleigh waves travel along the boundary with particle motion in an elliptical plane perpendicular to the wave propagation direction (Figure 2.4).

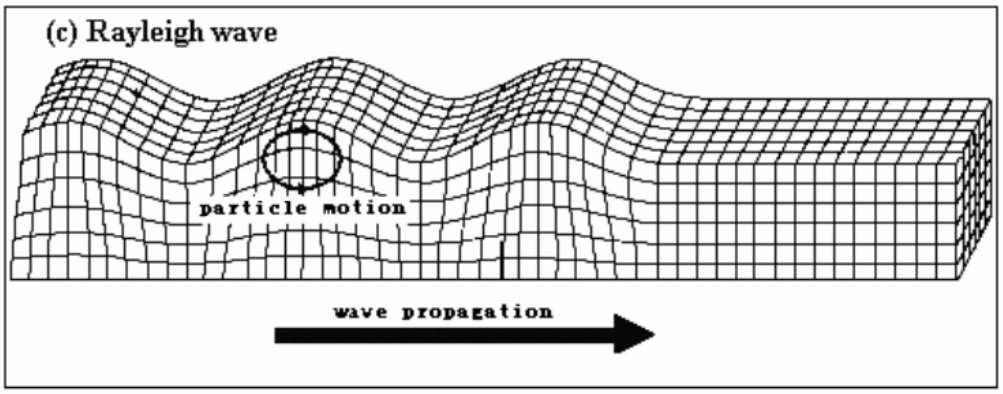

Figure 2.4 Rayleigh Waves (after Brown & Mussett, 1981*)*

The depth of material influenced by the Rayleigh wave is approximately equal to one wavelength (Xu 2004).

Love waves are polarized shear waves with an associated oscillatory particle motion parallel to the boundary and perpendicular to the direction of travel (Figure 2.5). Love waves are also dispersive and can be used in a similar way to Rayleigh waves to study the boundary conditions.

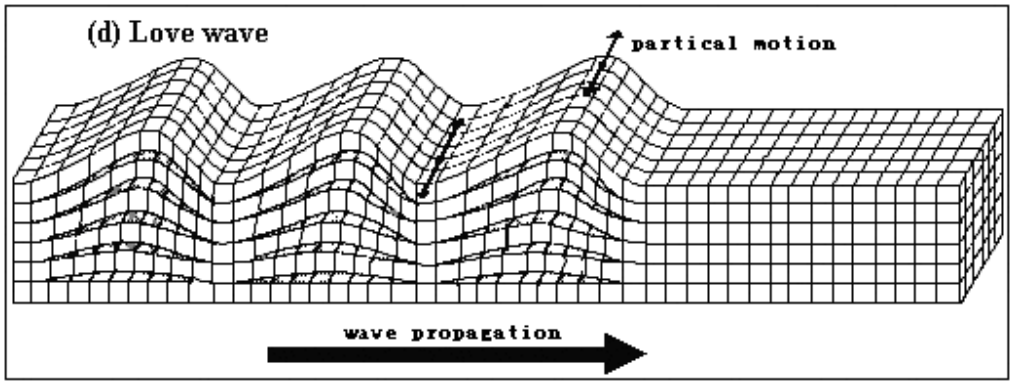

Figure 2.5 Love Wave (after Brown & Mussett, 1981)

Plane Waves

Although waves are spherical about a point source, at large distance one may simplify the solution and consider the waves to be plane waves. Considering the wave equation as a function of x in space and t in time get plane waves. Figure 2.6 is the schematic definition of a plane sine wave. The large arrow is a vector which is the direction of ray path, which describes i) the direction of wave propagation by its orientation perpendicular to the wave fronts, and ii) the wavelength. Assume a wave front as a line along the crest of the wave, which is a surface through all points of equal phase. In other words, at the wave front, all

particles move in the same phase. Rays or ray paths are perpendicular to the wave fronts and they point in the direction of wave propagation.

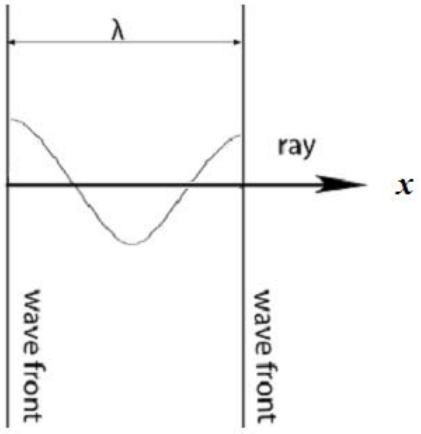

Figure 2.6 Definition sketch for a plane sine wave. The wave fronts are constant phase surfaces separated by one wavelength. The ray path is normal to the wave fronts and its length is the wavenumber λ

For plane waves, the wave Equation (2.6) can be simplified as

$$\frac{\partial^2 u}{\partial x^2} = \frac{1}{c^2}\frac{\partial^2 u}{\partial t^2} \qquad (2.7)$$

where c is velocity of the wave propagation. Equation (2.7) can be solved as d'Alembert's solution

$$u(x,t)=g(x-ct)+h(x+ct) \qquad (2.8)$$

where g and h are arbitrary functions. The function $g(x - ct)$ represents a disturbance propagating in the positive x direction with speed c. The function $h(x+ct)$ represents a

disturbance propagating in the negative x axis: this part of the solution is ignored in the following, but it must be taken into account when dealing with wave interference.

Equation (2.8) can be easily checked by respective second-order differential of the equation over x and t,

$$\frac{\partial u}{\partial x} = g'(x - ct) + h'(x + ct) \qquad (2.9)$$

$$\frac{\partial^2 u}{\partial x^2} = g''(x - ct) + h''(x + ct) \qquad (2.10)$$

$$\frac{\partial u}{\partial t} = -cg'(x - ct) + ch'(x + ct) \qquad (2.11)$$

$$\frac{\partial^2 u}{\partial t^2} = c^2 g''(x - ct) + c^2 h''(x + ct) \qquad (2.12)$$

In Fourier analysis, a wavelet can always be decomposed into a finite series of harmonic waves, so Equation (2.8) can be represented by

$$u(x,t) = A\cos\kappa(x - ct) \qquad (2.13a)$$

$$u(x,t) = Ae^{i\kappa(x-ct)} \qquad (2.13b)$$

where A = amplitude of wave u,

κ = wavenumber, the number of wave cycles per length unit

$\kappa(x–ct)$ is the phase which governs the position of a given characteristic point (e.g., a peak or a trough) of the wave and satisfies

$$\kappa(x–ct) = \text{const} \qquad (2.14)$$

For a fixed time, harmonic waves should repeat every wavelength along the direction of propagation so they should satisfy

$$\begin{aligned} Ae^{ik\cdot x} &= Ae^{ik\cdot(x+\lambda n)} \\ &= Ae^{ik\cdot x}e^{ik\lambda k} \end{aligned} \qquad (2.15)$$

where λ is the wavelength, then

Equation (2.15) is true if

$$e^{ik\lambda n} = 1 = e^{i2\pi n} \qquad (2.16)$$

or

$$n\lambda k = 2\pi n$$

$$k = \frac{2\pi}{\lambda} \qquad (2.17)$$

For a fixed point, when t varies, then

$$\begin{aligned} \boldsymbol{T} &= \lambda/\boldsymbol{c} \\ \boldsymbol{f} &= 1/\boldsymbol{T} = \boldsymbol{c}/\lambda \\ \boldsymbol{c} &= \boldsymbol{f}\lambda \end{aligned} \qquad (2.18)$$

where T is the period.

Finally, in theory only homogeneous and isotropic media can maintain regular wave propagation as plane waves, while in practice, at distances sufficiently far from the source, waves can be considered as plane waves from a point source.

Rayleigh Waves

Rayleigh waves are the result of incident P and SV plane waves interacting at the free surface and traveling parallel to that surface as illustrated in Figure 2.7. The two interfering components propagate along the surface with the same velocity but they have different exponential laws of attenuation with depth and null stress along the free surface.

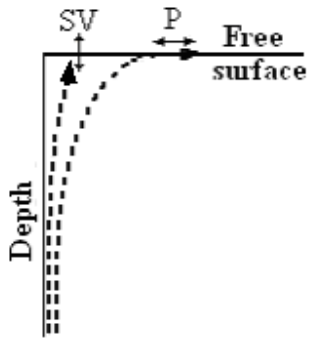

Figure 2.7 Rayleigh waves are produced from the superposition of two separate components: one longitudinal and the other transverse

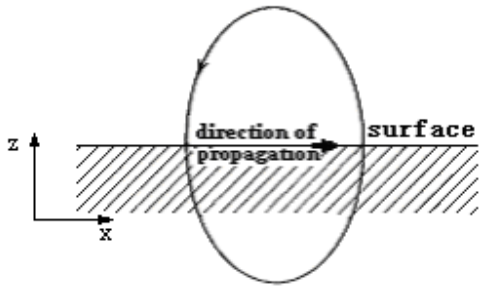

Figure 2.8 Particle motion on the surface during the passage of a Rayleigh waves in an elastic homogeneous halfspace (after Telford et al 1990)

The horizontal and vertical components of motion in the vertical *xz*-plane shown in Figure 2.8 are out of phase exactly 90°, and the vertical component has larger amplitude

than the horizontal one, as a result, Rayleigh waves travel along the boundary with particle motion in an elliptical plane perpendicular to the wave propagation direction.

Penetration depth in the Earth is important in Rayleigh wave studies. A Rayleigh wave's amplitude decreases exponentially with depth. These waves have a two-dimensional cylindrical geometry spread pattern that decreases with radius r from the source proportional to $1/\sqrt{r}$ (Lay and Wallace, 1995). This means that Rayleigh waves are usually the largest amplitude waves on a broadband seismometer. Rayleigh waves are also dispersive waves, that is, different frequencies propagate at different velocities in an inhomogeneous medium. This property allows lower frequencies to sample deeper material and different frequencies to arrive at different time, which makes them a valuable tool for determining the near surface structure of a region. In seismology, an earthquake's surface waves are observed to be dispersive which can be directly attributed to the velocity variations with depth in the Earth's interior and thus provide a powerful method of studying the structure of the lithosphere and asthenosphere. In engineering practice, it is easy to generate Rayleigh waves which penetrate tens of metres to obtain a depth profile of a medium. This phenomenon will be discussed in detail in the next section.

Rayleigh Wave Properties in Infinite Homogeneous Elastic Media

The simplest case of Rayleigh wave propagation is in a semi-infinite homogeneous elastic medium. Solution of the Rayleigh wave equation has been the subject of intensive

studies (Rahman & Barber., 1995, Nkemzi 1997, Malischewsky 2000, Royer 2001). The general idea can be summarized as imposition of the boundary conditions of null stress at the free surface on the general wave Equation (2.6) and derivation of the Rayleigh wave equation (Foti 2000):

$$(2-\frac{V_R^{\ 2}}{V_S^{\ 2}}) = 4(1-\frac{V_R^{\ 2}}{V_P^{\ 2}})^{1/2}(1-\frac{V_R^{\ 2}}{V_S^{\ 2}})^{1/2} \qquad (2.19)$$

The ratio between the two body wave velocities can be expressed as a function of the Poisson Ratio υ alone:

$$\frac{V_S}{V_P} = \sqrt{\frac{\mu}{\lambda+2\mu}} = \sqrt{\frac{1-2\upsilon}{2(1-\upsilon)}} \qquad (2.20)$$

where μ = shear modulus

Substituting Equation (2.20) in terms of V_P into (2.19) for V_R yields an approximate solution can be obtained:

$$\frac{V_R}{V_S} = \frac{0.862+1.14\upsilon}{1+\upsilon} \qquad (2.21)$$

Hence, Rayleigh wave velocity (V_R) could be expressed in terms of the S-wave velocity (V_S). Figure 2.9 summarizes the relationship between P-wave velocity S-wave velocity and that between Rayleigh wave velocity and S-wave velocity. It is evident that Rayleigh waves are closely related to S-waves and that Rayleigh wave velocity is slightly smaller than S-wave velocity.

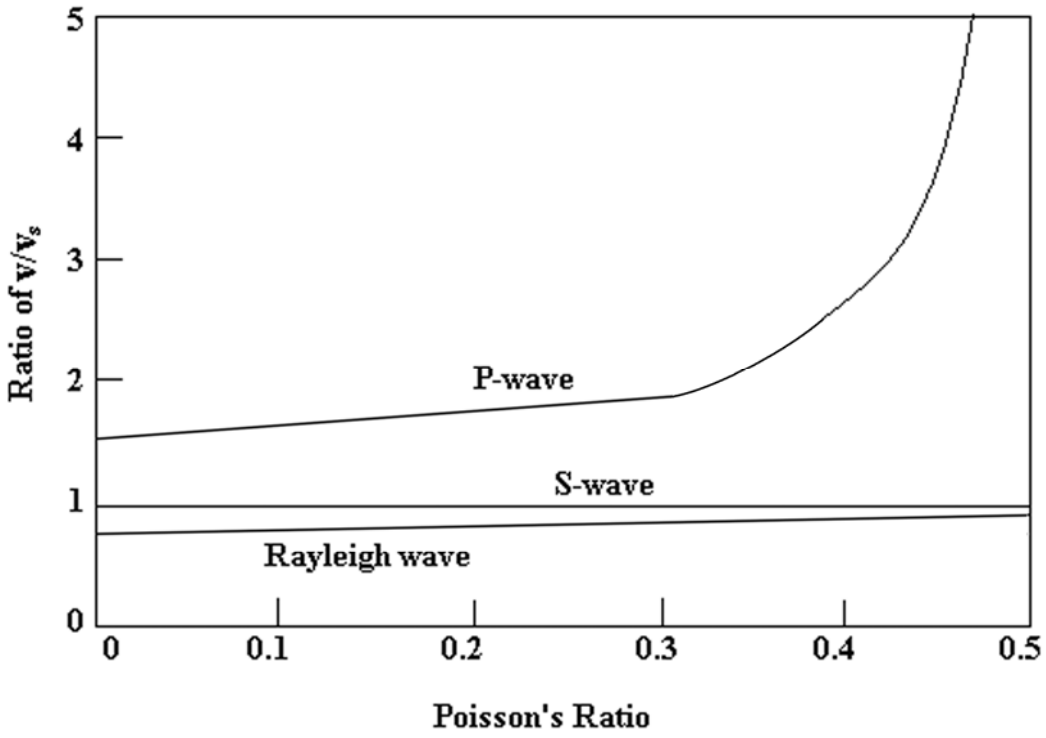

Figure 2.9 Ratio of P and Rayleigh wave velocity to S velocity with Poisson's ratio (after Richart et al 1970)

In soil and rock media, there is a range of Poisson's Ratio between 0 and 0.5, so the range of variation of V_R/V_S is:

$$0.86 < \frac{V_R}{V_S} < 0.96 \qquad (2.22)$$

or Rayleigh waves propagate at a theoretical speed range of about 86% to 96% of V_S. It is apparent that the difference between shear wave velocity and Rayleigh wave velocity is limited within a small range.

Al-Shayea (1994) shows that for υ = 0.25 the particle motion becomes a prograde (clockwise) ellipse with the change of sign of the horizontal component at a depth of z/λ_R ≈ 0.18, where λ_R is the wavelength of the Rayleigh wave. This reversion depth of displacement direction can be shown in a schematic diagram, Figure 2.10, which has normalized depth: $z/\lambda_R = kz/2\pi$. The vertical component has its maximum amplitude value of (0.67/0.62) ≈108.2% of its amplitude at the surface, at a depth of $z/\lambda_R \approx 0.1$. At a depth of $z/\lambda_R = 1.0$, the horizontal component decays to -12.9% of its value at the surface, and the vertical component decays to 23.6% of its value at the surface. At a depth of z/λ_R = 2.0, the above values reduce to -1.4% and 2.5% respectively. For a higher value of V_P/V_S for unconsolidated water saturated soils, or higher Poisson's ratio, the amplitude decay is somewhat smaller. The interference of the horizontal component, which is $\pi/2$ out of phase with the vertical component, makes the vertical motion of particles at the surface arch-type in shape rather than sinusoidal. This motion becomes purely sinusoidal at a depth of $z/\lambda_R \approx 0.18$, where the horizontal component is zero and then the shape is an inverted arch-type beyond that depth. In the theoretical case of a homogeneous halfspace there is no intrinsic length scale and V_R is independent of frequency. Actual field observations of Figure 2.10 agree roughly with the elliptical type of motion. Differences in type of motion are attributed to the Earth being layered and anisotropic rather than an ideal, homogeneous, isotropic, elastic medium.

Rayleigh waves are a range of low velocity, low frequency waves with a spectrum that is not sharply peaked and hence contain a broad range of wavelengths with a large variation of penetration. Penetration shows an exponential fall off as illustrated by Figure 2.10. This explains why most of the energy is confined to a zone of one wavelength thickness.

Higher frequency components of Rayleigh waves, which correspond to wavelengths that are shorter in comparison with the surface layer thickness, carry velocity information about the top layers, whereas longer wavelengths are associated with low frequencies at deeper penetration.

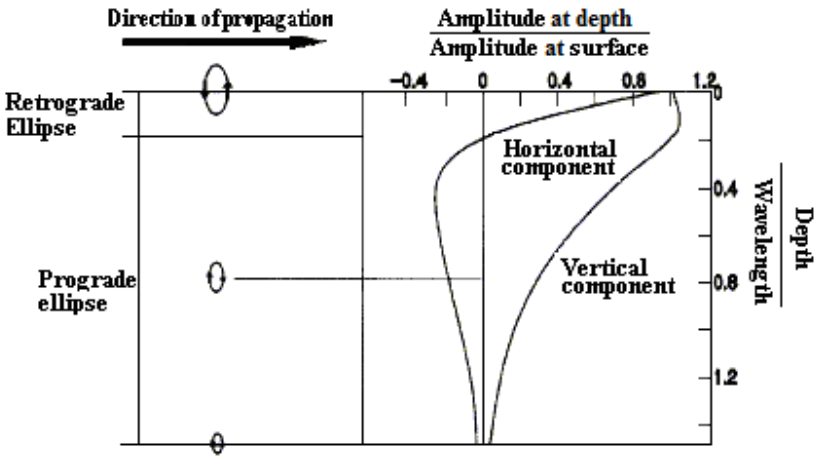

Figure 2.10 The motion of particle and attenuation of amplitude with depth for Rayleigh waves (after Richart et al 1970)

Rayleigh Wave Properties in Layered Media

In many places the mechanical properties vary considerably with depth near the surface. One assumption for seismological purposes is that a stratified medium has homogeneous linear elastic layers, and each layer is characterized by its thickness, elastic parameters and density (Figure 2.11).

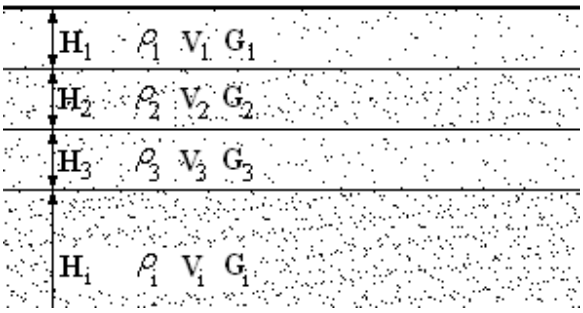

Figure 2.11 Model of a horizontally layered medium

Dispersion

Geometrical dispersion is the most important property related to Rayleigh wave propagation in layered media, i.e. Rayleigh wave phase velocity is dependent on frequency. Lai and Rix (1999) proved that, under the assumption of the classical exponential form of harmonics, the Navier equation of motion for vertically heterogeneous media, in absence of body forces, is a linear differential eigenvalue problem and finally introduced an implicit form of Rayleigh wave dispersion equation

$$F_R = \left[\lambda(z), \mu(z), \rho(z), \kappa_j, \omega\right] = 0 \qquad (2.23)$$

where z is depth, ω is frequency in radians

Equation (2.23) is a complicated function of Lamé parameters, the density, the wavenumber and the frequency of excitation. These particular values of κ_j are the eigenvalues of the eigenproblem. This equation indicates that in vertically heterogeneous media the velocity of propagation of Rayleigh waves is, in general, a multivalued-

function of frequency. Any given frequency has *M* normal modes of propagation. The number *M* can be finite or infinite, depending on the z-dependence of the medium properties and on the frequency of excitation. Furthermore, the distribution of the modes, namely the mode spectrum, can be continuous or discrete, and in some cases both. In a medium composed of a finite number of homogeneous layers overlaying a homogeneous half-space, the total number of Rayleigh modes of propagation is always finite (Ewing et al., 1957).

The mode of Rayleigh waves is very important both in theory and application. Foti (2000) conducted analysis by numerical simulations for both normal and inverse media. The results are shown in Figure 2.12. In both cases, for low frequencies, only one free Rayleigh mode exists while as the frequency increases, other modes arise. Figure 2.12 (a) also gives the comparison between modal and effective phase velocity, or calculated phase velocity, in a normal medium and the comparison indicated that for normally dispersive media higher modes have no influence and hence the effective phase velocity coincides with the phase velocity of the fundamental Rayleigh mode.

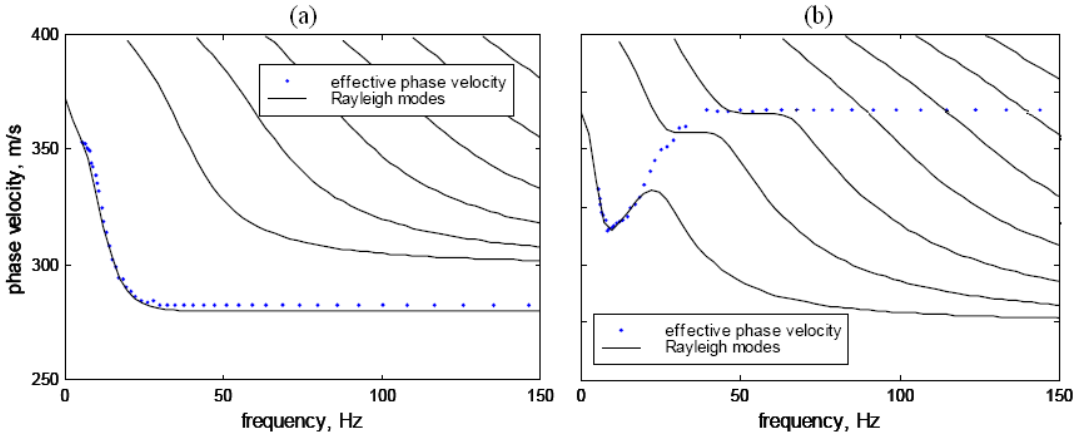

Figure 2.12 Examples of normally dispersive (a) and inversely dispersive (b) profiles (after Foti 2000)

Figure 2.12(b) shows the phase velocity is not monotonically decreasing with frequency. It is also shows that the influence of higher modes has serious consequences. Higher modes have to be taken into account for inversely dispersive media so that it is possible to identify deep layers in a characterization problem.

The shape of the dispersion curve (Rayleigh phase velocity vs. frequency or wavelength) is strongly related to the variation of stiffness with depth (Rix 1988). Usually a distinction is made between a layered system for which the stiffness is increasing with depth and another one in which there is the presence of stiffer layers over softer ones. The first case is indicated as normally dispersive profile, the latter one as inversely dispersive profile. An example is presented in Figure 2.13, where the shape of the dispersion curve is presented in the phase velocity-wavelength plane.

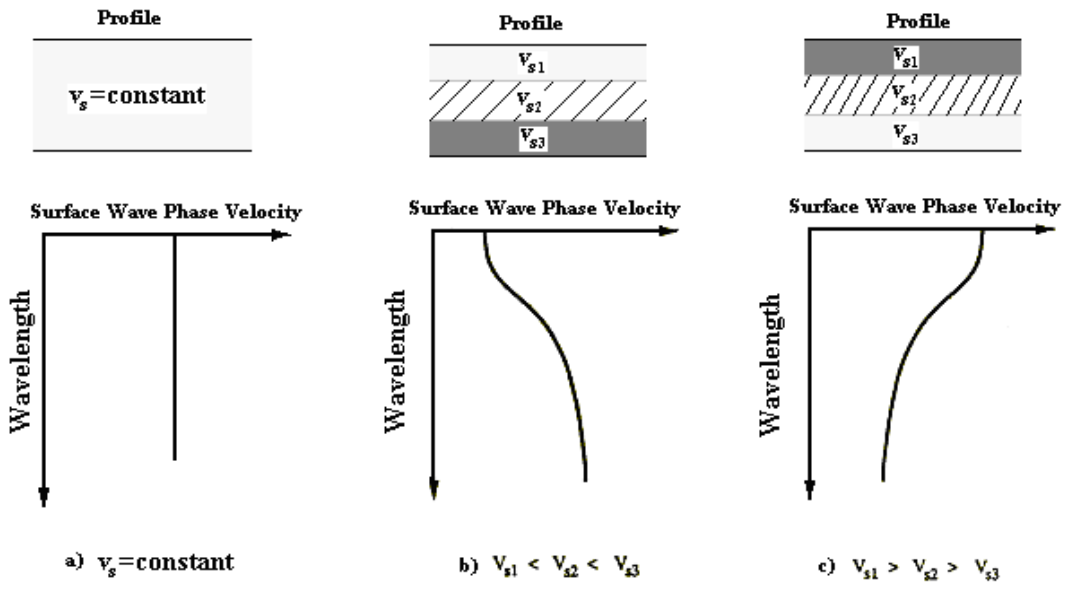

Figure 2.13 Examples of non dispersive (homogeneous halfspace), normally dispersive and inversely dispersive profiles (after Rix 1988)

This representation is often used since it gives a clear picture of the variation of stiffness with depth. In real media the alternation of stiff and soft layers can be much more complex than the above cases; still Figure 2.13 gives an idea of the relation between the stiffness profile and the dispersion curve.

Frequency-Dependant Penetration Depth

Generally surface waves of higher frequencies travel slower than those of lower frequencies because lower frequency waves penetrate deeper into the ground surface than higher frequency waves. This concept is schematically illustrated in Figure 2.14, where the vertical displacements wave field in depth at two different frequencies is presented for a layered medium.

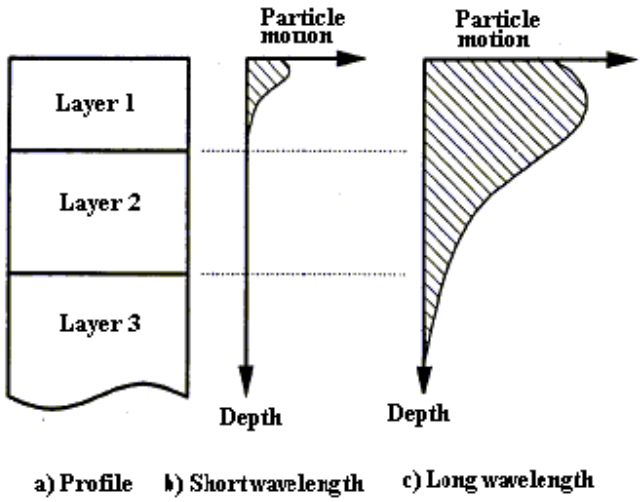

Figure 2.14 Geometrical dispersion in layered media (Rix 1988)

Hence in the case of a vertically heterogeneous medium, surface waves at different frequencies involve propagation in different layers and consequently the phase velocity is

related to a combination of the mechanical properties over a range of depth. The surface wave velocity is a function of frequency, offset (distance from a source) and properties of the medium.

Group Velocity and Phase Velocity

An important consequence of surface wave dispersive behavior in layered media is the existence of a group velocity (Telford et al 1990). So far, the wave velocity discussed is known as phase velocity, which is the velocity of a point of constant phase such as a peak or a trough. For a dispersive medium, this is not the same as the velocity of a pulse of energy, which is referred to as group velocity. A pulse can be decomposed into its component frequencies by Fourier analysis, each frequency component traveling with its own velocity. Figure 2.15 defines group velocity and gives comparison of the two concepts. The velocity of the wave train or the velocity of the envelope (a) is indicated as group velocity, in contrast with that of the carrier that is the phase velocity. Only in a non-dispersive medium, or an infinite homogeneous and isotropic medium, does group velocity coincide with phase velocity.

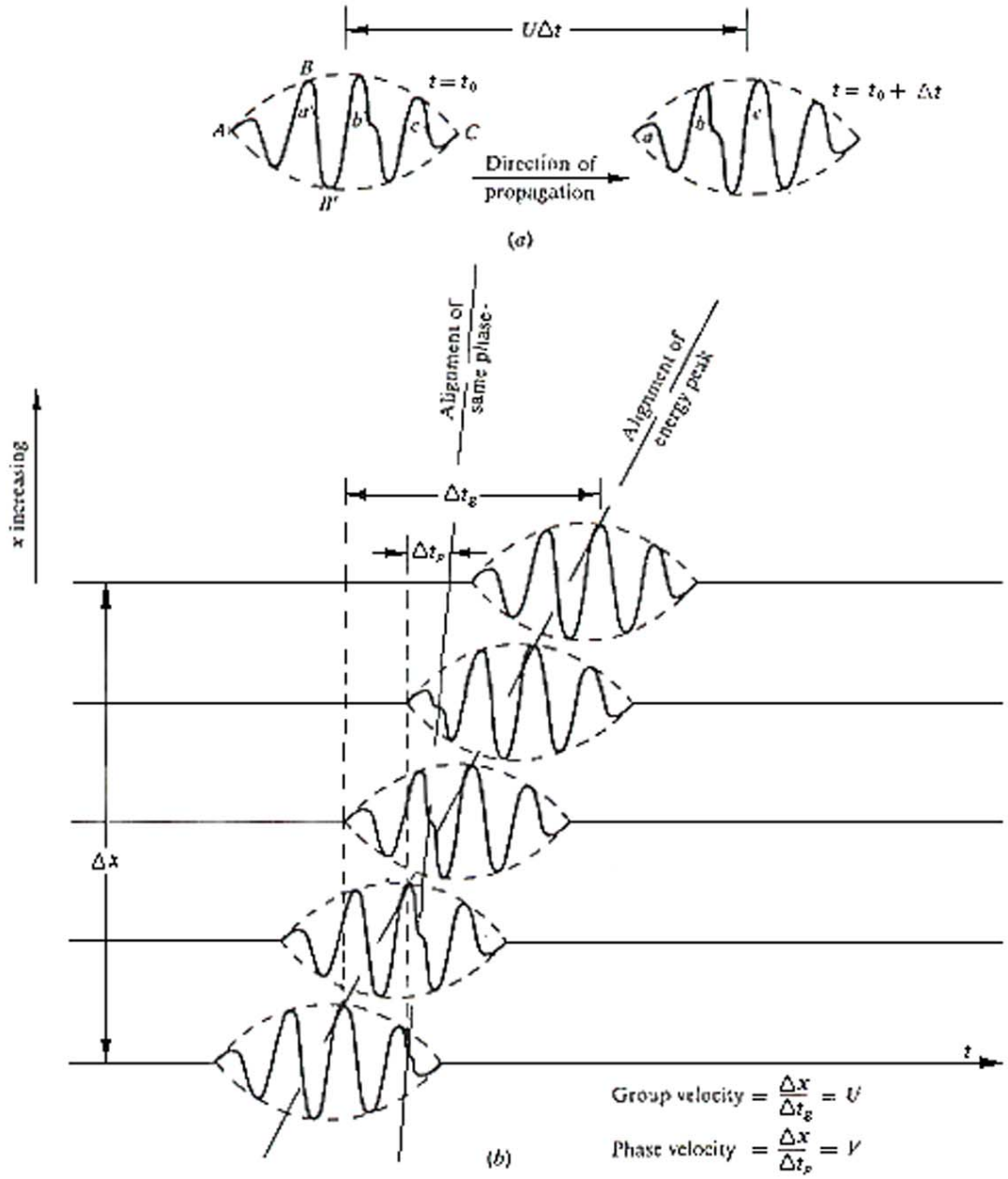

Figure 2.15 Group velocity and phase velocity: (a) definition of group velocity *U*, (b) comparison of group velocity and phase (Telford et al 1990)

Mathematically, phase velocity and group velocity can be defined as (Telford et al 1990):

$$V(\omega) = \frac{\omega}{k(\omega)} \tag{2.24}$$

$$U(\omega) = \frac{d\omega}{dk} \tag{2.25}$$

where U = group velocity, V = phase velocity, k = wavenumber.

The relation between them is

$$U = V - \lambda \frac{dV}{d\lambda} = V + \omega \frac{dV}{d\omega} \tag{2.26}$$

The values of $dV/d\lambda$ and $dV/d\omega$ are average for the range of frequencies that make up one part of the pulse.

When V decreases with frequency, V is larger than U. This is called normal dispersion. In this case, the carrier travels faster than the envelope. If a carrier appears at the beginning of the pulse, it overtakes and passes through the envelope and finally disappears in the front (as shown in Figure 2.15(b). Obviously everything reverses for the case of an inverse dispersion, which is defined as V increase with frequency.

Rayleigh Wave Properties in Laterally Varying Media

In reality, the near surface is not always made up of horizontal layers. Dipping layers are common ranging from shallow dipping to almost vertical. When Raleigh waves

propagate through those types of media, reflections occur on the interfaces. The larger the contrast of acoustic impedance (the product of density ρ and velocity V) across the interface, the more Rayleigh wave energy will be reflected back. Manning and Margrave (1999) proved that surface wave reflections and transmissions have similarities to body wave reflections and transmissions using finite difference modeling (FDM) of elastic wave fields at the surface of the earth through shallow lateral and vertical velocity changes.

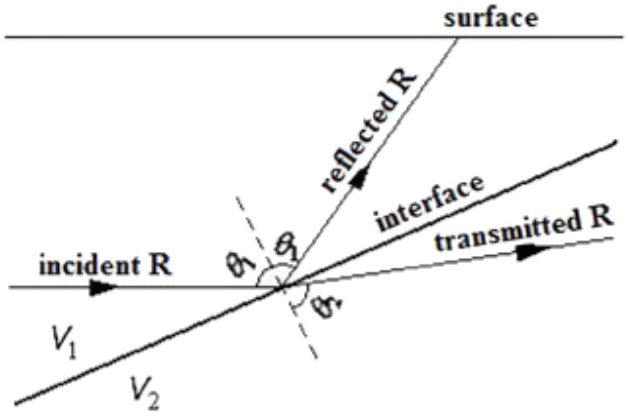

Figure 2.16 Rayleigh wave propagation at interface of acoustic impedance contrast ($V_2 > V_1$)

Figure 2.16 shows the ray paths of Rayleigh wave propagation at an interface of acoustic impedance contrast. When a Rayleigh wave is incident on the dipping interface, reflected and transmitted Rayleigh wave rays are generated. According to Snell's Law

$$\frac{\sin\theta_1}{V_1} = \frac{\sin\theta_2}{V_2} \qquad (2.27)$$

When $V_1 > V_2$, Rayleigh wave passes through the interface into the lower velocity layer, so the refracted Rayleigh wave ray is bent down; whereas when $V_1 < V_2$, Rayleigh wave

passes through the interface into the higher velocity layer, so the transmitted Rayleigh wave ray turns upward when θ_1 reaches the critical angle.

Considering the incident angle, when the interface tends to be vertical, or incident angle θ_1 approaches zero, the incident Rayleigh wave becomes normal to the interface and the reflected ray is known as back-scattered Rayleigh wave.

How much energy is reflected and transmitted is also very important in considering Rayleigh wave applications. For normal incidence can be expressed by the reflection and transmission coefficients in term of energy (Telford et al 1990):

$$R = \left[\frac{\rho_2 V_2 - \rho_1 V_1}{\rho_2 V_2 + \rho_1 V_1} \right]^2 \qquad (2.28)$$

$$T = 1 - R = \frac{4(\rho_1 V_1)(\rho_2 V_2)}{(\rho_2 V_2 + \rho_1 V_1)^2} \qquad (2.29)$$

Where R and T are the reflection and transmission coefficients in term of energy.

If $R = 0$, all the incident energy is transmitted. This is the special case when there is no contrast of acoustic impedance across the interface, even if both the density and the velocity values are different in the two layers. The other special case is $T = 0$, that is all the incident energy is reflected. This situation is at free surface of an air- or water-filled cavity.

Discontinuity and Subsurface Cavities

In the above discussion, Rayleigh wave energy propagates through a uniform medium or through a medium with an interface of acoustic impedance contrast. In both cases, the body is continuous. If there is an abrupt discontinuity, such as a well developed fault or a cavity, diffraction occurs. Diffraction refers to phenomena associated with wave propagation, such as the bending, spreading and interference of waves passing by an object or aperture that disrupts the wave. Figure 2.17 can be used to illustrate the relationship of diffraction over the wavelength and size of a discontinuity in terms of an object; there are three cases:

i) For $\lambda < d$, stronger back scattered Rayleigh wave energy and weaker transmission occurs

ii) For $\lambda \cong d$, equally strong back scatter & transmission occurs

iii) For $\lambda > d$, weaker back scattered Rayleigh wave energy and stronger transmission occurs

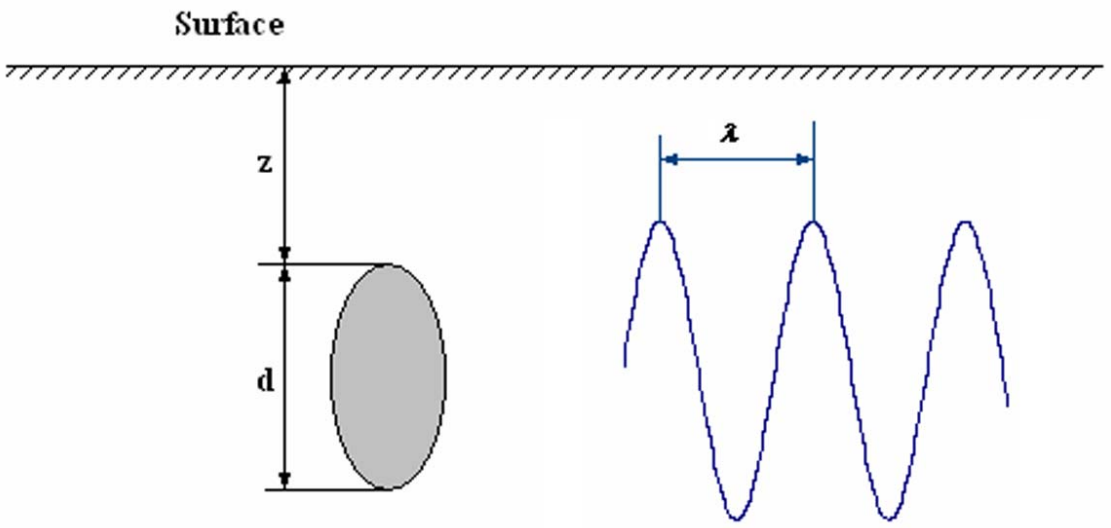

Figure 2.17 Lateral velocity variation models in two modes: λ = wavelength, z = depth of object and d = size of object

Whenever diffraction occurs, its effects are generally most noticeable for waves where the wavelength is comparable or greater than the feature size of the diffracting objects or apertures. Diffraction can be explained by Huygens' Principle. Figure 2.18 illustrates the diffraction effect of a fault. For a plane wavefront AB normally incident on the interface CD, the position of the wavefront when it reaches the surface of the wall at $t = t_0$ is COD. At $t = t_0+\Delta t$, the portion to the right of O has advanced to the position of GH, whereas the portion to the right of O has been reflected and reached the position of EF. We might have constructed the wavefronts of EF and GH by selecting a large number of centers in CO and OD and drawing arcs of length $V\Delta t$. EF and GH would then be determined by the envelopes of these arcs. However, for the portion of EF there would be no centres above O to define the envelope, whereas for the portion GH there would be no centres below O to define the envelopes. Thus O marks the point of transition point between centres that

give rise to the upward-traveling wavefront EF and centres that give rise to downward-traveling wavefront GH. The arc FPG with center O is the diffracted wavefront originating at O and connecting the two wavefronts EF and GH. The diffracted wavefront also extends into the geometrical shadow area GN and into the region FM.

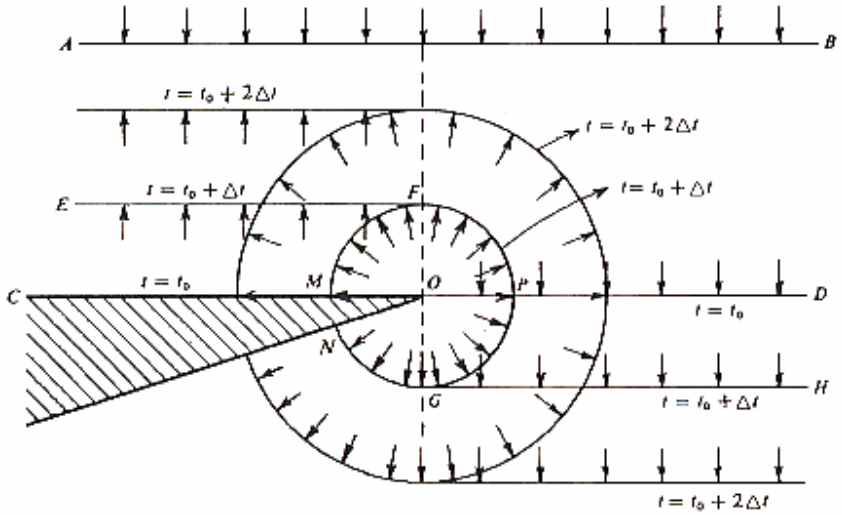

Figure 2.18 Diffracted wavefronts: diffraction allows seismic energy to reach regions forbidden by ray theory (after Telford et al 1990)

Xia et al. (2007) derived a Rayleigh-wave diffraction travel time equation for detecting near-surface feature with Rayleigh-wave diffraction. Assuming a void in a homogeneous and isotropic medium (Figure 2.19), the travel time equation for the Rayleigh-wave diffraction can be written as Equation 2.30.

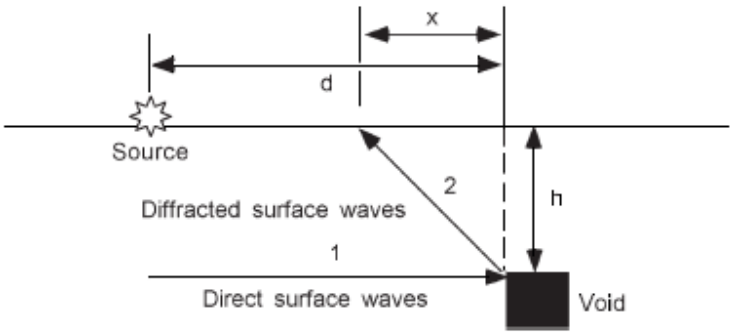

Figure 2.19 Geometry of surface wave diffraction (Xia et al, 2007)

$$t_x = \frac{1}{c}\left[d + \left(x^2 + h^2\right)^{1/2}\right] \qquad (2.30)$$

where c = Rayleigh wave velocity

x = horizontal distance from the apex of the hyperbola corresponding to the edge of the void

t_x = diffraction arriving time at x

d = horizontal distance from the source to the apex of the hyperbola

h = depth to the top of the void

when $x \gg h$, t_x becomes a linear function of x,

$$t_x = \frac{1}{c}(d + x) \qquad (2.30b)$$

when x=0, obtain the arrival time t_0 at the hyperbola:

$$t_0 = \frac{1}{c}(d + h) \tag{2.31}$$

The solutions are based on only two travel times extracted from the diffraction: one at the apex of the hyperbola and the other at any other place along the hyperbola.

Substitute Equation (2.31) into (2.30) to eliminate c and obtain a quadratic equation,

$$ah^2 + bh + m = 0,$$

$$\text{where} \quad \text{a} = \left(\frac{t_x}{t_0}\right)^2 - 1, \quad b = 2\frac{t_x}{t_0}\left(\frac{t_x}{t_0} - 1\right)d$$

$$m = \left[\left(\frac{t_x}{t_0}\right)^2 - 2\left(\frac{t_x}{t_0}\right) + 1\right]d^2 - x^2$$

The quadratic equation can then be solved

$$h = \frac{-b + \sqrt{b^2 - 4am}}{2\text{a}} \tag{2.32}$$

If the Rayleigh wave diffraction can be determined from seismic data or processed seismic data, it is straightforward to determine the location of a cavity. Unfortunately, the reality is much more complicated than a uniform background medium, and always gives rise to difficulty in isolating these waves. However, back scattered energy is often seen in some portions of a seismic section and this might be helpful to determine the existence of anomalies.

CHAPTER 3: RAYLEIGH WAVE ISOLATION

Rayleigh waves are the fundamental tool that will be used in this research. Field seismic data often consists of many different waves and seismic events. This chapter concentrates on the processing of Rayleigh wave isolation from field seismic data. Different techniques to be discussed focus on how to suppress unwanted wave types or seismic events in the form of coherent and random ambient noise. The goal is to enhance Rayleigh waves.

Field Seismic Data

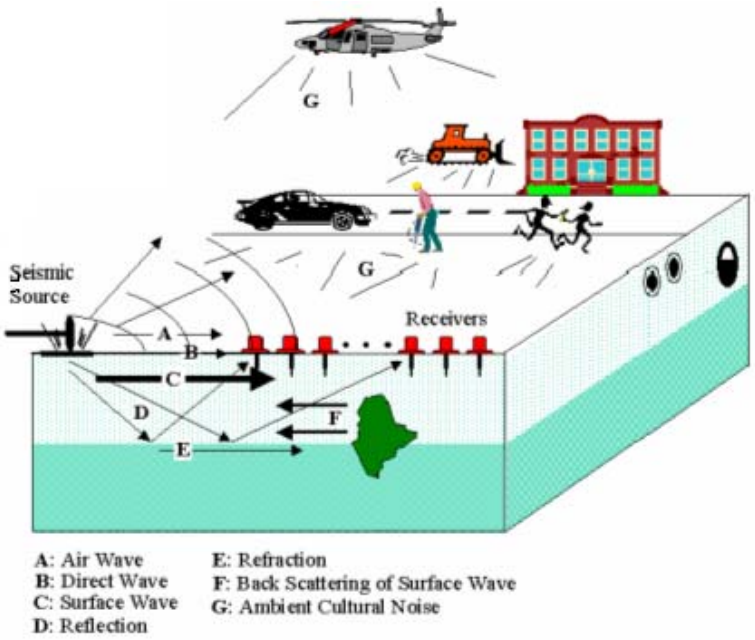

Figure 3. 1 Field conditions of data acquisition (KGS Workshop, 2005)

Figure 3.1 gives an example of a field system of data acquisition. The field is an urban area full of human activities around the field and the geological formation is mainly horizontal layers with an anomaly inside.

The field seismic data was acquired by a geophone spread of 55 stations at a spacing of 2 metres (KGS Workshop, 2005). When seismic data acquisition was conducted on the ground, all vibrations would arrive to the geophone spread and could be recorded in the seismic data. The acquired field seismic data in the form of seismogram are shown in Figure 3.2.

There are several wave types in seismic section:

i) Direct wave B always is the first arrival in the near field.

ii) Refracted waves E are persistent and make up the early arrivals and can be easily recognized.

iii) Reflection D occurs when there is acoustic impedance contrast at the interface.

iv) Rayleigh waves, C, are recognized by low frequency, strong amplitude and low group velocity. It is the dispersive vertical components of Rayleigh waves

v) Back scattered energy F due to the anomaly in the layers along the survey line.

vi) The air waves A often appear with a constant velocity of 300 m/s in near field.

vii) Ambient culture noise G.

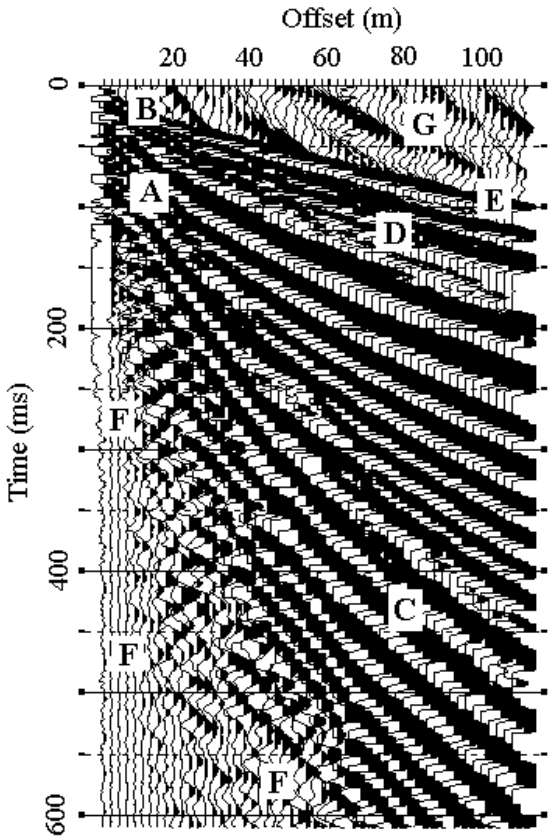

Figure 3. 2 Field seismic data corresponding to Figure 3.1. All the letters stand for the same events as Figure 3.1 (KGS Workshop, 2005)

In addition to all these that can be seen in the record, there probably is other noise as follows:

viii) Side scattered energy which occurs where there are irregularities, either natural or manmade (a conduit or drainage system). It is harmful when side scattered energy appears and interferes with other events.

ix) Power lines also cause noise in the form of monofrequency wave (Yilmaz 1988). The frequency depends on where the field survey is conducted.

x) Multiples from a strong reflector,

xi) Reverberation at low frequency caused from loose shallow near surface

The geophone spread, whose length equals to maximum offset, should be long enough to separate different events in the record. From Figure 3.2 it is apparent that many arrivals might overlap in the near field. The consequences of the key geometric parameters such as distance between source and the nearest geophone, distance between the source and the farthest geophone, and inter- geophone spacing, are discussed in the following sections.

Minimum Offset

The estimation of the near field of the pulse source is based on two considerations: one factor is that the nearest receiver has to be set far enough to be in the elastic zone and can detect only elastic waves, and the other is the consideration that the surface wave method requires the analysis of horizontally traveling plane waves of Rayleigh waves and avoids recording of any non-planar components. Surface waves become planar only after

travailing a certain distance from the source, and this distance is known to be a function of wavelength (Nazarian and Stokoe, 1994; Park et al., 1999). A longer wavelength takes a greater distance before it becomes planar. Historically it was proposed to discard all data for which the distance between the source and the first receiver was less than one third of the obtained wavelength. However, a near field extension of half a wavelength is assumed for a normally dispersive medium whereas about two wavelength is a more prudent estimate for a strongly inverse dispersive medium, i.e. where a soft layer is present below or trapped between stiffer ones (Foti 2000).

Maximum Offset.

In order to obtain long wavelength components, spatial signals are recorded as far as possible. Usually there are four factors that may limit the maximum spatial extent of the receiver spread: power of a source, number of geophones serially connected in one geophone cable, ground condition of a site to be investigated and data processing. The effect of the first three factors is straightforward. A discussion on data processing is presented here: the resolution of a dispersion curve image increases with the total length of receiver spread (Park et al., 1999). The resolution issue becomes critical, especially when the higher modes tend to take significant energy and need to be separated from the fundamental mode. A longer receiver spread is needed for the lower frequencies of surface waves whose phase velocities are greater than the higher frequencies. The overall resolution of the dispersion curve image improves rapidly as the receiver-spread length increases. Also, the low frequency components are acquired only when the spread length

is sufficient for them to become well-developed plane waves as previously explained in this section.

Spacing

There are several factors to be considered. First, because of attenuation, data from inter-receiver distance greater than about three wavelengths are usually strongly affected by noise and therefore it is preferable to discard them. The second important factor in spacing is lateral contrasts of stiffness. In a laterally varying medium, spacing should be set smaller to make sure not to miss important subsurface information. A larger spacing can produce spatial aliasing when lateral variation is present. This issue is discussed in Section 3.3. However, small spacing needs more geophones to reach a spread long enough, which makes field test more time consuming. In summary, spacing determination is a compromise among topographical and geological conditions, an acquisition system and project requirements.

Processing in *x-t* Domain

Seismic data can be expressed in a 2D matrix. If *m* geophones are used and *n* sampling points are applied within recording time, one shot gather of seismic data can be represented as $u_{ij}(x, t)$, i.e., the vertical particle movement of the set of *m* receivers is recorded as $u_{ij}(x, t)$:

$$u_{ij}(x,t) = \begin{pmatrix} u_{1,1} & u_{1,2} & \cdots & u_{1,k} & \cdots & u_{1,l} & \cdots & u_{1,m-1} & u_{1,m} \\ u_{2,1} & u_{2,2} & \cdots & u_{2,k} & \cdots & u_{2,l} & \cdots & u_{2,m-1} & u_{2,m} \\ \vdots & \vdots & \vdots & \vdots & \vdots & \vdots & \vdots & \vdots & \vdots \\ u_{i,1} & u_{i,2} & \cdots & u_{i,k} & \cdots & u_{i,l} & \cdots & u_{i,m-1} & u_{i,m} \\ \vdots & \vdots & \vdots & \vdots & \vdots & \vdots & \vdots & \vdots & \\ u_{j,1} & u_{j,2} & \cdots & u_{j,k} & \cdots & u_{j,l} & \cdots & u_{j,m-1} & u_{j,m} \\ \vdots & \vdots & \vdots & \vdots & \vdots & \vdots & \vdots & \vdots & \vdots \\ u_{n-1,1} & u_{n-1,2} & \cdots & u_{n-1,k} & \cdots & u_{n-1,l} & \cdots & u_{n-1,m-1} & u_{n-1,m} \\ u_{n,1} & u_{n,2} & \cdots & u_{n,k} & \cdots & u_{n,l} & \cdots & u_{n,m-1} & u_{n,m} \end{pmatrix} \quad (3.1)$$

where t = time elapsed in ms, x = offset in metres, $1 \le I \le n$, $1 \le j \le m$

To suppress unwanted energy in a seismograph, there are two approaches using a polygon filter as discussed below.

The first approach is to design a polygon filter so that all desired energy is enclosed inside the filter and all unwanted energy is excluded. A matrix of Equation (3.2) can be used to represent this filter. To conveniently make the filter design, a polygon is graphically picked up in a seismograph. The elements inside the polygon are assigned values of one, whereas the elements outside the polygon are zeros. The filter is defined as Equation (3.2).

$$\Gamma_{ij}(x,t) = \begin{pmatrix} 0 & 0 & \cdots & 0 & \cdots & 0 & \cdots & 0 & 0 \\ 0 & 0 & \cdots & 0 & \cdots & 0 & \cdots & 0 & 0 \\ \vdots & \vdots & \vdots & \vdots & \vdots & \vdots & \vdots & \vdots & \vdots \\ 0 & 0 & \cdots & 1 & \cdots & 1 & \cdots & 0 & 0 \\ \vdots & \vdots & \vdots & \vdots & \vdots & \vdots & \vdots & \vdots & \\ 0 & 0 & \cdots & 0 & \cdots & 1 & \cdots & 0 & 0 \\ \vdots & \vdots & \vdots & \vdots & \vdots & \vdots & \vdots & \vdots & \vdots \\ 0 & 0 & \cdots & 0 & \cdots & 0 & \cdots & 0 & 0 \\ 0 & 0 & \cdots & 0 & \cdots & 0 & \cdots & 0 & 0 \end{pmatrix} \quad (3.2)$$

The product of the original field data $u_{ij}(x,t)$ and the filter $\Gamma_{ij}(x,t)$, which is given in Equation (3.2), is the desired energy shown in Equation (3.4).

$$U_{ij}(x,t) = u_{ij}(x,t) \bullet \Gamma_{ij}(x,t) \tag{3.3}$$

$$U_{ij}(x,t) = \begin{pmatrix} 0 & 0 & \cdots & 0 & \cdots & 0 & \cdots & 0 & 0 \\ 0 & 0 & \cdots & 0 & \cdots & 0 & \cdots & 0 & 0 \\ \vdots & \vdots & \vdots & \vdots & \vdots & \vdots & \vdots & \vdots & \vdots \\ 0 & 0 & \cdots & u_{i,k} & \cdots & u_{i,l} & \cdots & 0 & 0 \\ \vdots & \vdots & \vdots & \vdots & \vdots & \vdots & \vdots & \vdots & \\ 0 & 0 & \cdots & 0 & \cdots & u_{j,l} & \cdots & 0 & 0 \\ \vdots & \vdots & \vdots & \vdots & \vdots & \vdots & \vdots & \vdots & \vdots \\ 0 & 0 & \cdots & 0 & \cdots & 0 & \cdots & 0 & 0 \\ 0 & 0 & \cdots & 0 & \cdots & 0 & \cdots & 0 & 0 \end{pmatrix} \tag{3.4}$$

As a result, the processed data preserves only the elements defined by the filter.

The second approach for polygon filtering is to design a polygon filter so that all unwanted energy is inside the polygon and all desired energy is outside. To do this in the same way as the first approach, a polygon is picked in a seismograph. The elements inside the polygon are given zeros, whereas the elements outside the polygon are assigned ones. The filter is represented as Equation (3.5).

$$\overline{\Gamma_{ij}}(x,t) = I - \Gamma_{ij}(x,t) = \begin{pmatrix} 1 & 1 & \cdots & 1 & \cdots & 1 & \cdots & 1 & 1 \\ 1 & 1 & \cdots & 1 & \cdots & 1 & \cdots & 1 & 1 \\ \vdots & \vdots & \vdots & \vdots & \vdots & \vdots & \vdots & \vdots & \vdots \\ 1 & 1 & \cdots & 0 & \cdots & 0 & \cdots & 1 & 1 \\ \vdots & \vdots & \vdots & \vdots & \vdots & \vdots & \vdots & \vdots & \vdots \\ 1 & 1 & \cdots & 1 & \cdots & 0 & \cdots & 1 & 1 \\ \vdots & \vdots & \vdots & \vdots & \vdots & \vdots & \vdots & \vdots & \vdots \\ 1 & 1 & \cdots & 1 & \cdots & 1 & \cdots & 1 & 1 \\ 1 & 1 & \cdots & 1 & \cdots & 1 & \cdots & 1 & 1 \end{pmatrix} \tag{3.5}$$

where I is a unit matrix of $m \times n$.

The product of the original field data $u_{ij}(x,t)$ and the filter $\overline{\Gamma_{ij}}(x,t)$, which is given in Equation (3.5), is:

$$\overline{U_{ij}}(t,x) = u_{ij}(t,x) \bullet \overline{\Gamma_{ij}}(t,x) \tag{3.6}$$

As a result, the processed data defined by the filter only preserve the elements in Equation (3.7).

$$\overline{U_{ij}}(x,t)=\begin{pmatrix} u_{1,1} & u_{1,2} & \cdots & u_{1,k} & \cdots & u_{1,l} & \cdots & u_{1,m-1} & u_{1,m} \\ u_{2,1} & u_{2,2} & \cdots & u_{2,k} & \cdots & u_{2,l} & \cdots & u_{2,m-1} & u_{2,m} \\ \vdots & \vdots & \vdots & \vdots & \vdots & \vdots & \vdots & \vdots & \vdots \\ u_{i,1} & u_{i,2} & \cdots & 0 & \cdots & 0 & \cdots & u_{i,m-1} & u_{i,m} \\ \vdots & \vdots & \vdots & \vdots & \vdots & \vdots & \vdots & \vdots & \\ u_{j,1} & u_{j,2} & \cdots & u_{j,k} & \cdots & 0 & \cdots & u_{j,m-1} & u_{j,m} \\ \vdots & \vdots & \vdots & \vdots & \vdots & \vdots & \vdots & \vdots & \vdots \\ u_{n-1,1} & u_{n-1,2} & \cdots & u_{n-1,k} & \cdots & u_{n-1,l} & \cdots & u_{n-1,m-1} & u_{n-1,m} \\ u_{n,1} & u_{n,2} & \cdots & u_{n,k} & \cdots & u_{n,l} & \cdots & u_{n,m-1} & u_{n,m} \end{pmatrix} \tag{3.7}$$

Figure 3.3 shows the effect of a polygon *x*-*t* filter [$\Gamma_{ij}(x,t)$], on a field seismic data. The original field data is displayed in (a) with a filter applied to them, and the right figure (b) is the resultant from the filter. It is clear to see that all the features inside the polygon are well preserved while all the elements outside the polygon are eliminated.

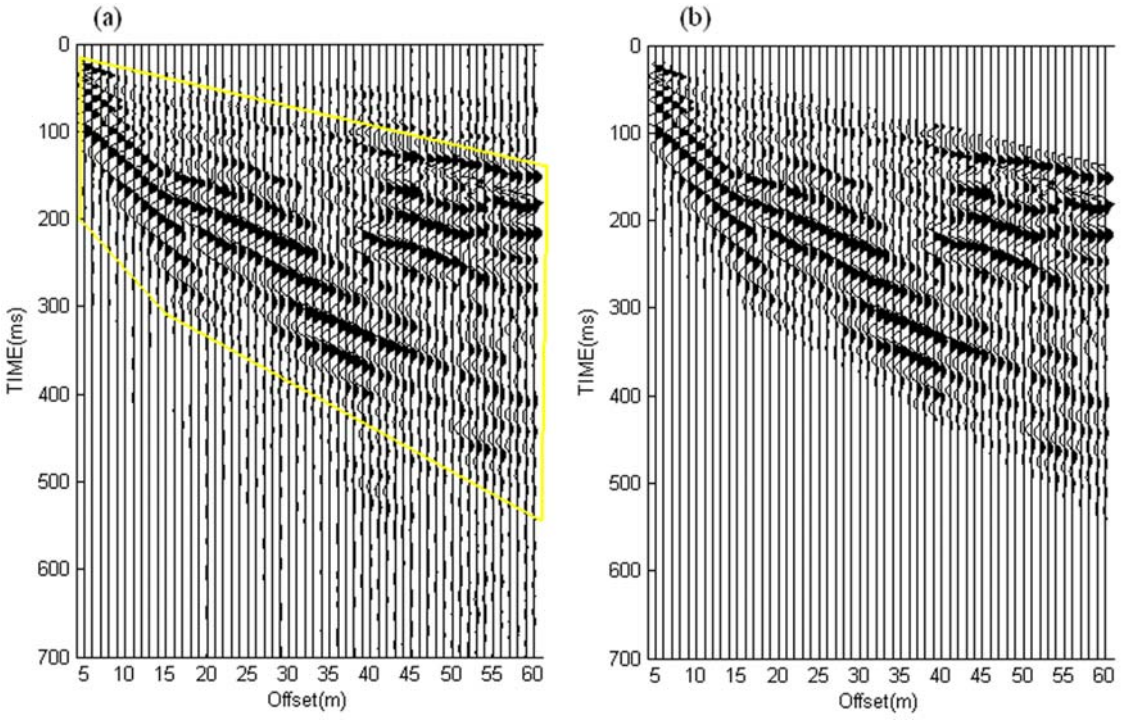

Figure 3.3 (a) A field seismic data with an *x*-*t* filter marked in yellow and (b) the resultant data through a polygon *x*-*t* filter

This *x-t* filter is brutal and can give rise to the additions of high frequency to the seismic data. These high frequency additions can be removed by a bandpass frequency filter, which will be discussed next.

Frequency Filter

Although Rayleigh waves are low frequency seismic energy, a relatively high sampling frequency (or short time interval between consecutive samples) has to be set for field data acquisition, so that Rayleigh wave components can be enhanced by a bandpass filter.

Why a high sampling frequency: Nyquist sampling criterion

Figure 3.4 shows a sinusoidal wave and the digital signals that are obtained when the sine wave is sampled at different time intervals. Figure 3.4(a) shows the sine wave sampled eight times per period. If there is the assumption that the signal is linear between sampled points, a reasonable facsimile of the original waveform is obtained. Figure 3.4(b) shows the sine wave sampled twice per period. The digital output yields an accurate representation of the frequency, but misrepresents the amplitude. Figure 3.4(c) shows the sine wave sampled less than twice per period. The frequency of the digital signal is lower than that of the original analogue signal. This phenomenon is called aliasing. In order to obtain correct information about the frequency of a wave, sampling at a rate at least twice the highest frequency has to be applied. This minimum sampling frequency f_s is given by the Nyquist Sampling criterion:

$$f_S = 2f_{\max} \text{ or } \Delta t_S = \frac{1}{2f_{\max}} \tag{3.8}$$

where f_{max} = highest frequency in the analogue signal

Δt_s = minimum sampling interval.

When sampling at the minimum Nyquist sampling rate of $2f_{max}$, the frequency content or spectral content of the original wave is retained.

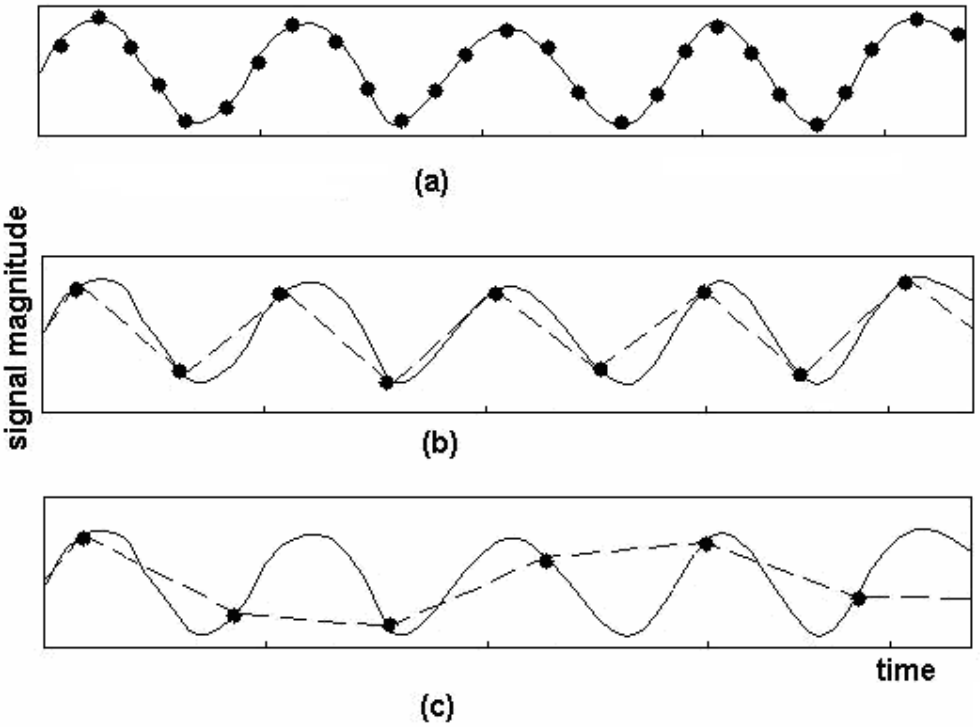

Figure 3.4 Digitizing a sinusoidal wave signal at different sampling rates: (a) 8 times/period, (b) 2 times/period, (c) <2 times/period

Frequency Filter

A bandpass filter is a digital operation that passes frequencies within a certain range and rejects (attenuates) frequencies outside that range. An ideal filter would have a

completely flat pass band with no gain/attenuation throughout and would completely attenuate all frequencies outside the pass band. In practice, no bandpass filter is ideal. The filter does not attenuate all frequencies outside the desired frequency range completely; in particular, there is a region just outside the intended pass band where frequencies are attenuated, but not rejected. This is known as the filter roll-off, and it is usually expressed in dB of attenuation per octave or decade of frequency. Generally, the design of a filter seeks to make the roll-off as narrow as possible, thus allowing the filter to perform as close as possible to its intended design. However, as the roll-off is made narrower, the pass band is no longer flat and begins to "ripple." This effect is particularly pronounced at the edge of the pass band in an effect known as the Gibbs phenomenon.

Figure 3.5 shows a bandpass filter applied to a signal consisting of two events A and B in frequency domain, where event A is the desired signal and event B is the unwanted event to be removed. There is a frequency f_c at which the gain of the filter is at its maximum, and the frequency f_c is called the resonant frequency,. A frequency band is simply the difference between the lower cutoff frequency f_1 and the upper cutoff frequency f_2.

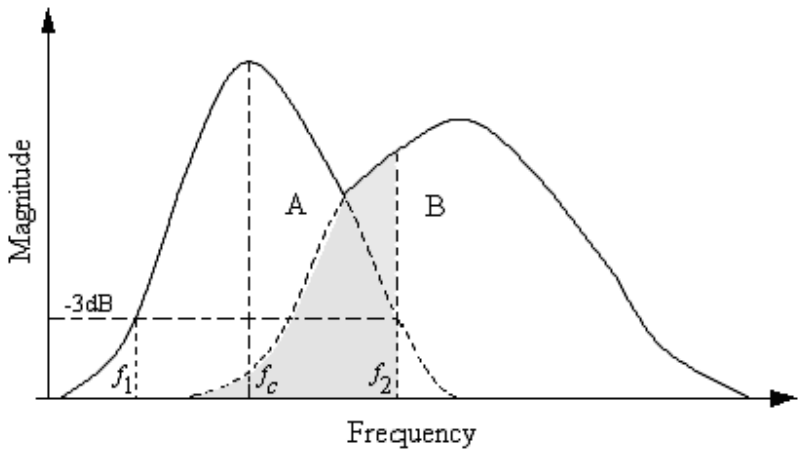

Figure 3.5 A bandpass filter

The bandwidth consists of those frequencies for which the power is a significant fraction of the maximum. In practice, the amplitude at f_2 and f_1 is defined to be greater than or equal to m times the maximum. The constant m is called the significance factor and is usually chosen to be $1/\sqrt{2}$ of amplitude as this implies 1/2 of the power at the maximum. The resulting bandwidth is called the half power bandwidth or -3dB bandwidth. The term -3dB is used as 10log (1/2) = -3.0103.

It is impossible to suppress the interference (shadow area in Figure 3.5) of the two events just by a bandpass filter.

Frequency filtering can be in the form of bandpass, bandreject, highpass (low-cut) or lowpass (high-cut) filters. In Figure 3.5, when $f_1 = 0$, the filter becomes a lowpass filter when $f_2 \to \infty$, the filter is a highpass filter.

Figure 3.6 shows the resultant of Figure 3.3(b) from a lowpass filter of cutoff frequency of 70Hz. The filter application removed the high frequencies caused by brutal *x*-*t* filtering and made smooth the edges of the signal.

Mathematically, frequency filtering involves multiplying the amplitude spectrum of an input seismic trace by that of a filter operator. This operation is based on an important concept in time series analysis: convolution in the time domain is equivalent to multiplication in the frequency domain. Similarly, convolution in the frequency domain is equivalent to multiplication in the time domain (Yilmaz, 1988).

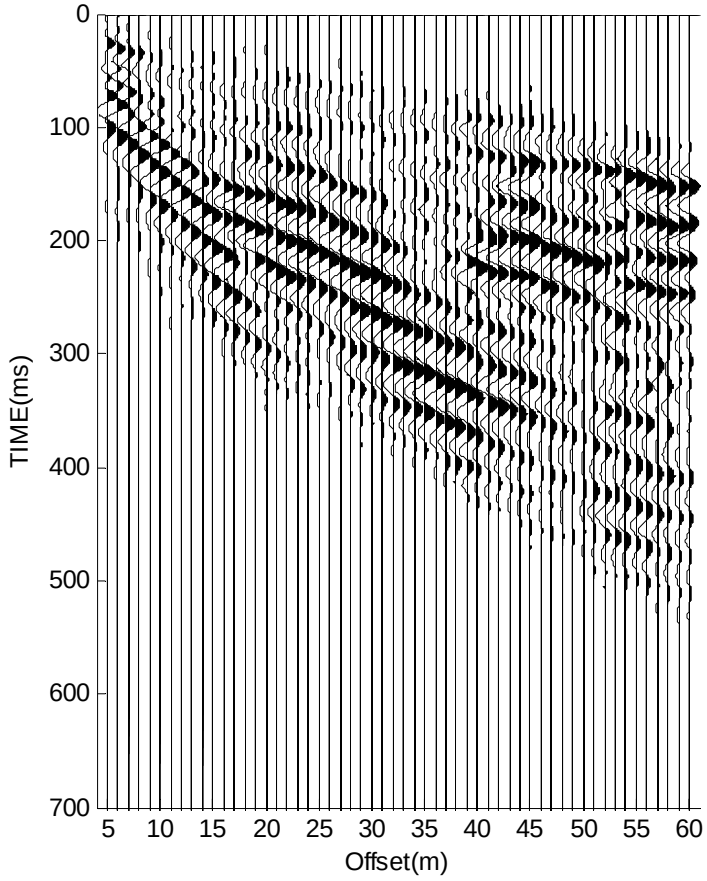

Figure 3.6 Resultant of Figure 3.3b from a lowpass Butterworth filter of a cutoff frequency of 70Hz.

The filtering process is described in Figure 3.7. The filtering process described here is zero phase frequency filters because it only band-limits the amplitude spectrum of the input while it does not modify its phase spectrum.

Filter order of the lowpass analogue prototype filter forms the basis for the bandpass filter design. The passband with two frequencies is specified. The first frequency determines the lower edge of the passband, and the second frequency determines the upper edge of the passband. Similarly, the stopband with two frequencies is specified. The first

frequency determines the upper edge of the first stopband, and the second frequency determines the lower edge of the second stopband.

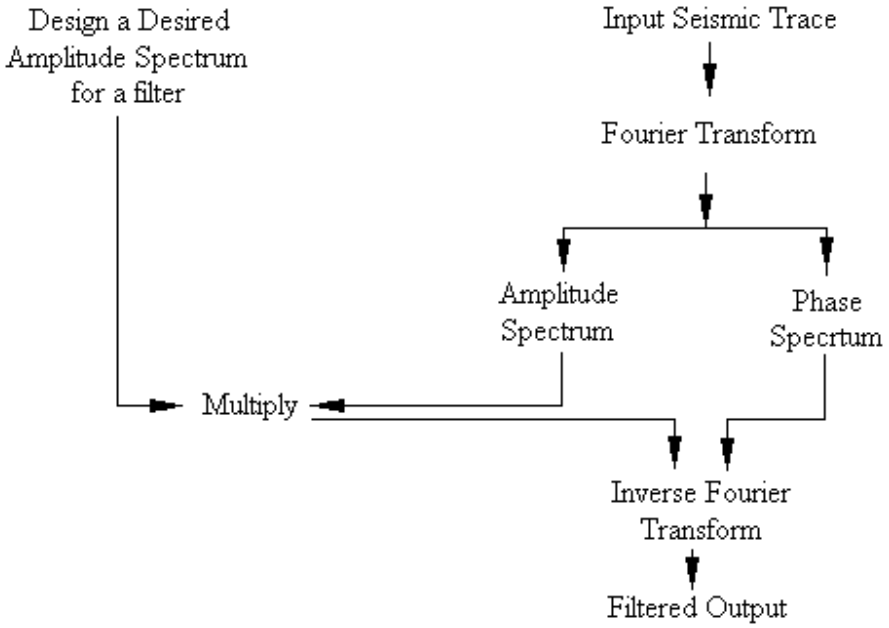

Figure 3.7 Design and application of a zero-phase filter in frequency domain (Yilmaz 1988)

There is a large range of prototype filter forms in literature. Table 3.1 gives some examples of bandpass filters. More details on filters are available in literature (e.g., Oppenheim and Schafer, 1989; Rabiner and Gold, 1975).

Table 3. 1 Filter design methods and parameters (Rabiner and Gold 1975,Oppenheim and Schafer 1989)

Design Method	Description	Filter Design Parameters
Butterworth	The magnitude response of a Butterworth filter is maximally flat in the passband and monotonic overall.	Order, lower passband edge frequency, upper passband edge frequency
Chebyshev I	The magnitude response of a Chebyshev I filter is equiripple in the passband and monotonic in the stopband.	Order, lower passband edge frequency, upper passband edge frequency, passband ripple
Chebyshev II	The magnitude response of a Chebyshev II filter is monotonic in the passband and equiripple in the stopband.	Order, lower stopband edge frequency, upper stopband edge frequency, stopband attenuation
Elliptic	The magnitude response of an elliptic filter is equiripple in both the passband and the stopband.	Order, lower passband edge frequency, upper passband edge frequency, passband ripple, stopband attenuation
Bessel	The delay of a Bessel filter is maximally flat in the passband.	Order, lower passband edge frequency, upper passband edge frequency

f - k Filter and Spatial Aliasing

Seismic events interfering with one another in the *x-t* domain may possibly be separated in the *f-k* domain. Amplitude spectra in *f-k* domain may separate different events since it is not likely that different events have both the same frequency and wavenumber. The numerical computation of the 2-D Fourier Transform as shown in Figure 3.8 maps input data in the *x-t* domain to output data in the *f-k* domain. The mathematical formations of 1-D Fourier transform and 2-D Fourier transform are presented in Appendix A.

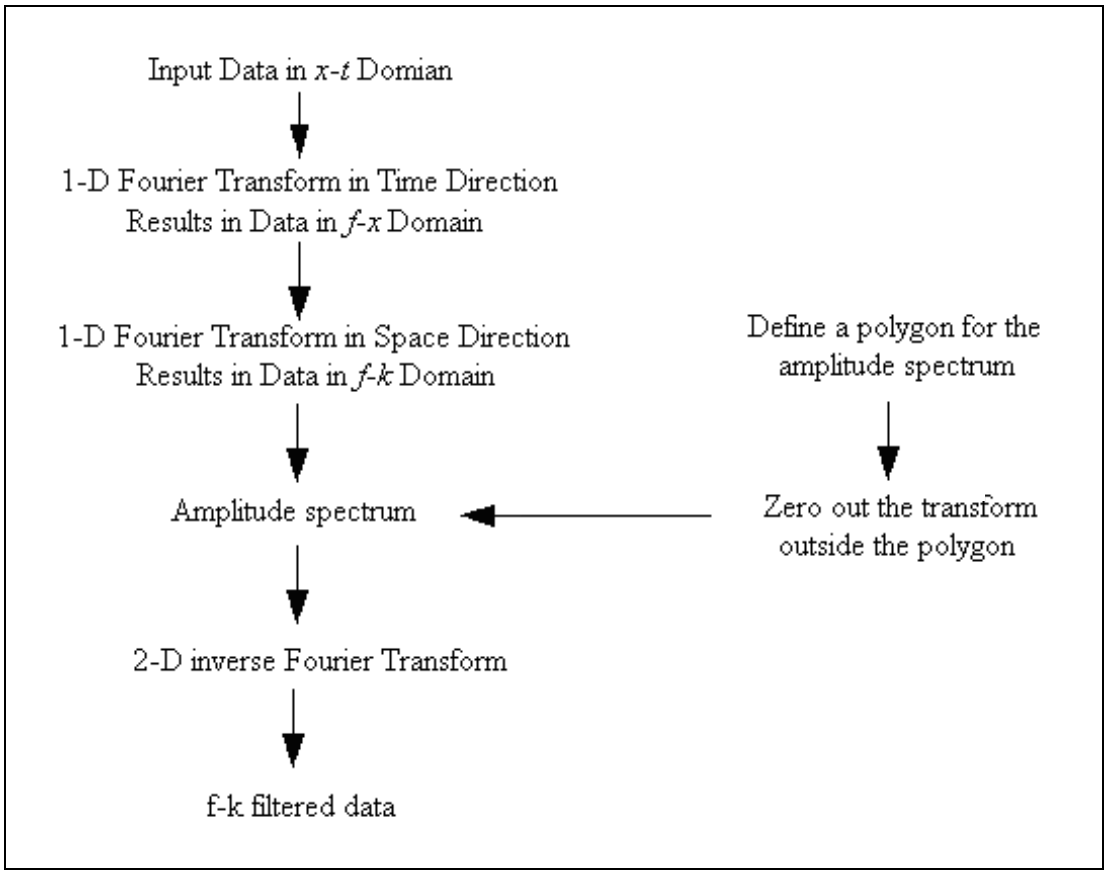

Figure 3.8 Computation of 2-D Fourier Transform and *f-k* filtering

Figure 3.9 shows the *f-k* filtering application on a set of field seismic data. These data were acquired in West Waverley Gold District near Dartmouth, Nova Scotia in summer 2006. The field trial targeted imaging old workings of a gold mine. Details will be reported in later chapters.

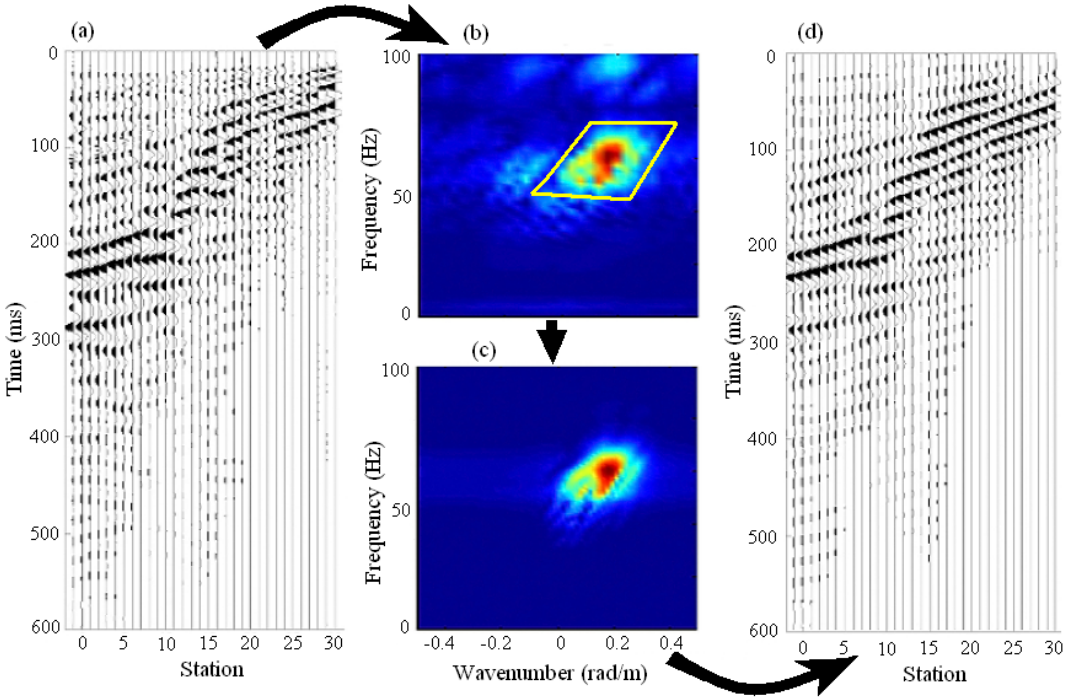

Figure 3.9 Process of *f-k* filter: (a) field data, (b) *f-k* spectrum of (a) with *f-k* filter in a quadrilateral window, (c) *f-k* spectrum after *f-k* filtering, (d) *f-k* filtered data of (a)

In Figure 3.9, the left seismic section (a) is the field data, the middle top (b) is the *f-k* spectrum of (a) with an *f-k* filter in a quadrilateral window, the middle bottom (c) is *f-k* spectrum after *f-k* filtering, and the right section (d) is *f-k* filtered data of (a). The arrows indicate the implementation of *f-k* filtering. In the original seismic section (a), there are many different seismic events such as direct p-waves in the early window, back scattered energy between 100 and 250 ms at stations 7 to 11 and stations 15 to 17 , which interfere with direct Rayleigh waves. In addition, high frequency noise from traffic and operation is also buried in this section. The *f-k* filter yielded a much better seismic record (d) in which direct Rayleigh waves stand out more clearly.

A significant issue for *f-k* filtering is spatial aliasing and resolution which can be the base of sampling criterion in spatial domain. Similar to frequency aliasing, spatial aliasing results in wrongly converted wavenumbers during Fourier transform in the space direction. Yilmaz (1988) discussed spatial aliasing problems and showed how dipping events and high frequency cause spatial aliasing. Figure 3.10 shows how the *f-k* spectra changed with different dips at different frequencies.

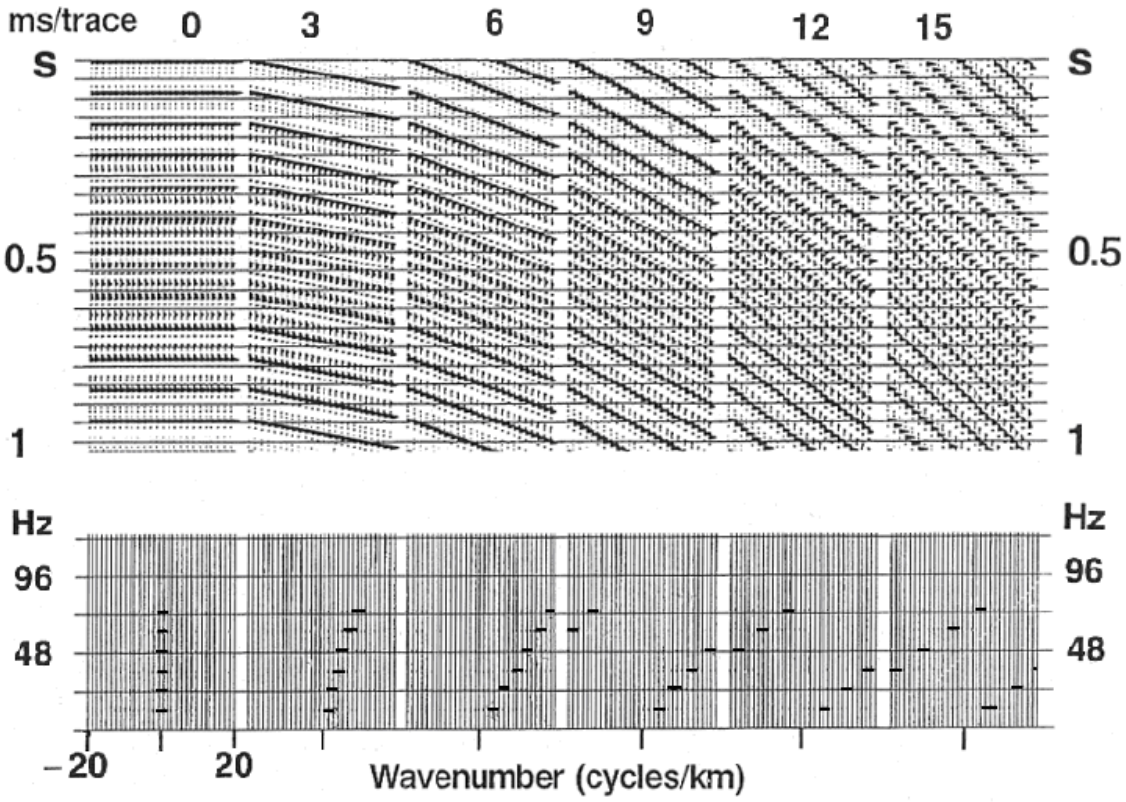

Figure 3.10 Spatial aliasing due to dipping and high frequency: top row is six gathers dipping ranges from 0 to 15 ms/trace, bottom row is the corresponding spectra of a monofrequency range from 12 to 72 Hz with 12 Hz increment (Yilmaz 1988)

In Figure 3.10, the top row gives six gathers with dipping range from 0 to 15 ms/trace, and the bottom row is the corresponding *f-k* spectra at monofrequencies ranging from 12

to 72 Hz with an increment of 12 Hz. From these results, it is expected that, for the same dipping formations, spatial aliasing might occur with frequency increase. On the other hand, for the same frequency, spatial aliasing also tends to occur with increasing dip.

Another cause of spatial aliasing is inline geophone spacing. Figure 3.11 shows *f-k* spectra of field data from Beijing Research Institute of Hydropower and Geophysical Surveying (Liu 2001).

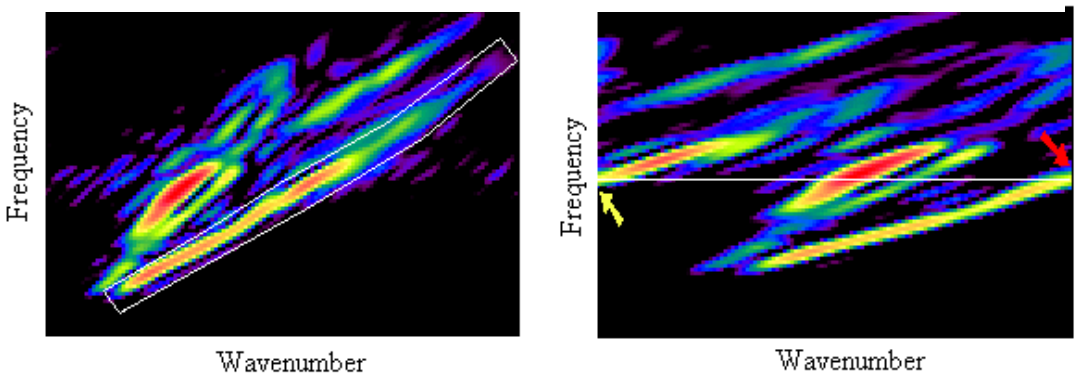

(a) (b)

Figure 3.11 Comparison of a normal *f-k* spectrum (a) and an aliased *f-k* spectrum (b) (Liu 2001)

The two *f-k* spectra are from the same survey line of 48 metre length, but with two different spacings. The left spectrum was from 24 channels with a spacing of 2 metres. This field configuration gave a wavelength range between 1 to 96 metres (λ_{min}= 2/3=0.67 m, λ_{max}= 48×2=96 m), and the corresponding wavenumber range was between 0.065 and 9.42 in radians ($\kappa = 2\pi/\lambda$, λ_{max}= 48×2=96 m). This spectrum was regular and apparent. Similarly, the right spectrum was from 12 channels with a spacing of 4 metres, which gave a wavelength range between 1.33 to 96 metres and a corresponding wavenumber

range between 0.065 and 7.71 in radians. The effect of the larger spacing is to wrongly map the energy from the red arrow to the yellow arrow because the geophone spacing could not sample the shortest wavelength (or maximum wavenumber) and wrapped the higher wavenumber into lower wavenumber.

Spatial aliasing can be demonstrated using simulated field data acquisition. Figure 3.12 shows how spatial aliasing occurs with increasing geophone spacing.

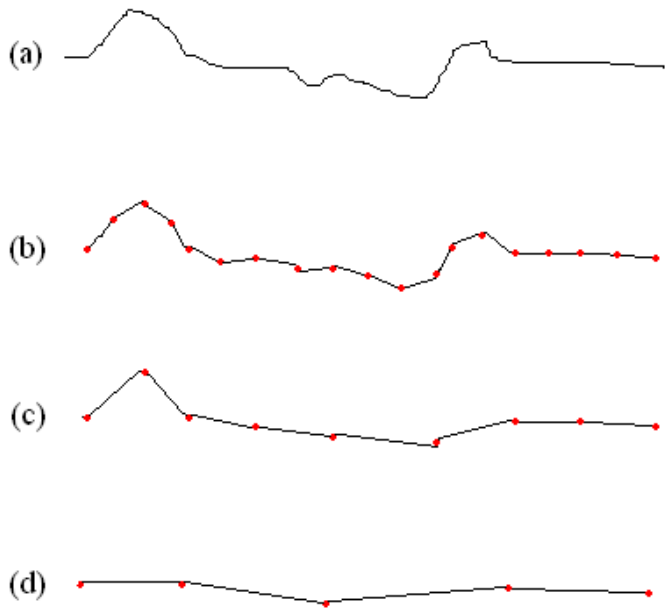

Figure 3.12 Relationship between spatial aliasing and geophone spacing: red dots are geophone locations and (a) original target, (b) signal from small spacing configuration, (c) signal from twice spacing configuration of (b), (d) signal from twice spacing configuration of (c)

In Figure 3.12, The original target (a) is assumed a one dimension datum of undulation with prominent peak and valley. When a small spacing configuration is used for data acquisition, it yields a profile (b) that represents the target well because the main characteristics are presented. With doubling the spacing, the acquisition yields profile (c)

that only retains a small part of the characteristics of this target. Further, when the spacing doubles again, the collected signal (d) losses most of the characteristics of this target. Essentially, this spatial aliasing occurs because the minimum wavelength resulting from these geophone spacing configurations (c and d) is greater then the spatial variation of this target. As a result, similar to frequency aliasing, the high wavenumber is folded into low wavenumber in digital data acquisition.

Another consideration is the length of geophone spread related to spatial resolution. Figure 3.13 is based on the same data as used for Figure 3.11.

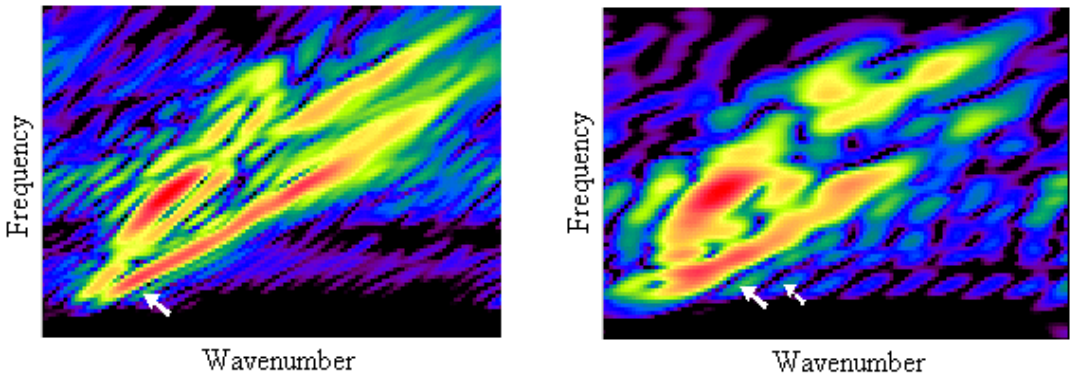

(a) (b)

Figure 3.13 Comparison of resolution in *f-k* domain of (a) a long geophone spread and (b) a short geophone spread (Liu 2001)

The left spectrum (a) is the original data of 24 channels with a 2 m geophone spacing while the right one (b) is only from the first 6 channels, or a geophone spread of 12 m. The right spectrum is much more blurred than the left spectrum. therefore it is necessary to use a long enough geophone spread for field configuration in order to improve confidence in seismic data processing.

Unlike frequency aliasing, for spatial aliasing problems neither a hardware filter nor a software filter can be implemented (Foti, 2000). So it is very important to choose small enough geophone spacing in field configurations to avoid spatial aliasing, and *f-k* filtering has to be applied to remove the energy of spatial aliasing if spatial aliasing appears in *f-k* spectrum. This fix, however, may cause energy leakage and important information loss. Another important question is if *f-k* filtering above is enough to enhance Rayleigh waves? My study gave the answer "NO". Chapter 4 discusses on this in more details.

Figure 3.14 shows the effects of different types of filtering. The left column is *f-k* spectra of field data (a) and respectively resulting from *x-t* filtering (b), *f-k* filtering (c) and a sequential combination of filtering of *x-t, f-k*, and bandpass filter (d). The corresponding seismic sections through (a') to (d') are displayed in the right column. Figure 3.14 (c) and (c') shows that *f-k* filtering might yield noise standing out in far field because attenuation made the genuine signal weaker and weaker while the noise presents random in the seismic section. If the noise happens to have the same *f-k* components as the genuine signal, the noise will suppress the signal in far field. This phenomenon cannot be easily differentiated in *f-k* spectrum (c) but projects itself out in *x-t* domain (c').

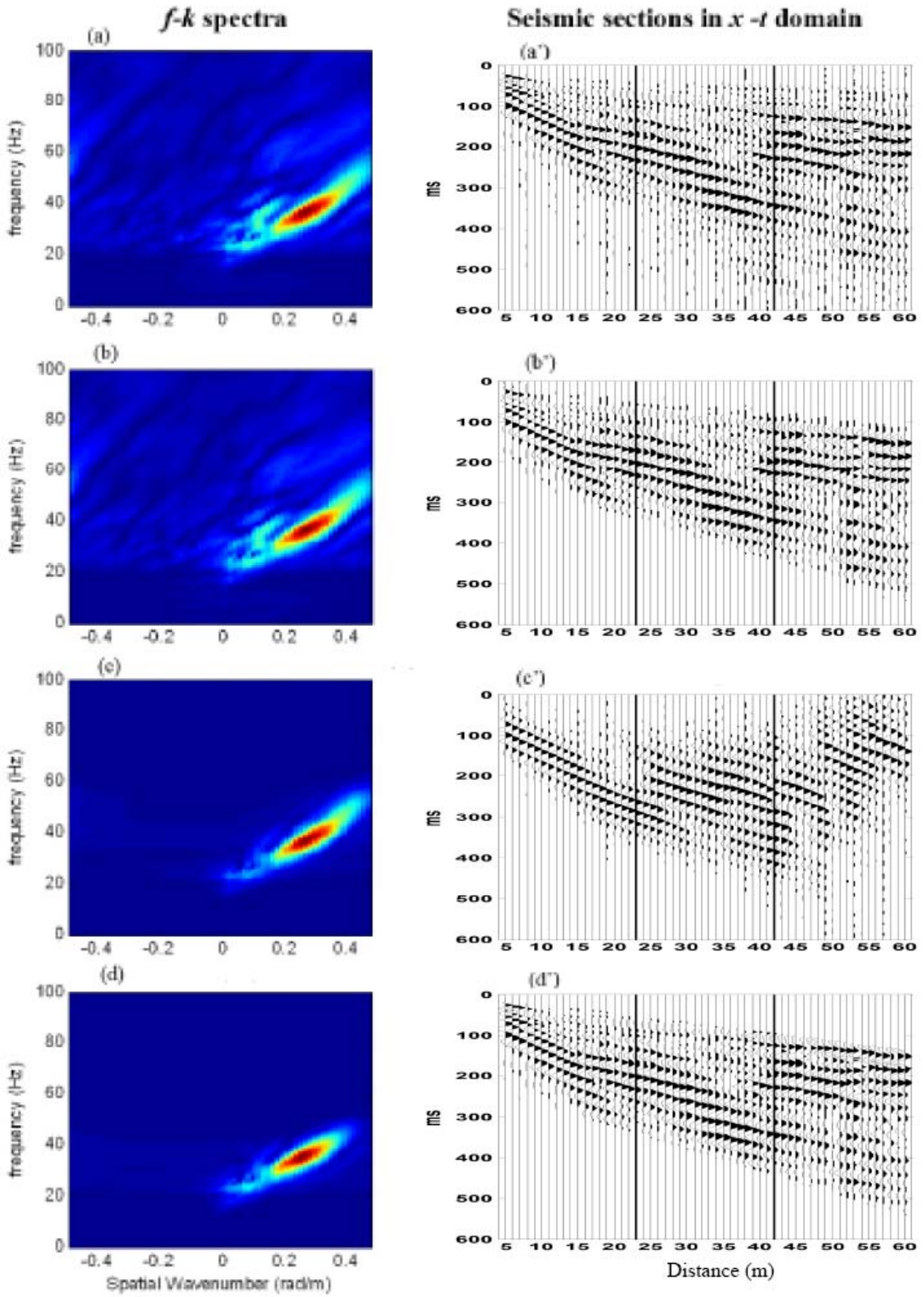

Figure 3.14 Comparison of different types of filtering. Left column for *f-k* spectra: (a) field data, (b) *x-t* filtered data, (c) *f-k* filtered data, (d) data from combination of filtering of *x-t, f-k*, and bandpass filter. The middle and right column are seismic sections corresponding to (a), (b), (c) and (d).

CHAPTER 4: DATA ANALYSIS OF SEISMIC RAYLEIGH WAVES

Seismic waves are usually measured by a multichannel geophone-spread on land or hydrophones for marine surveys, and recorded by a seismograph. The results are displayed in 2D images with offset from the point of excitation, or source, as horizontal axis and time as vertical axis. Seismic data analysis is the first step to evaluate the data quality and identify seismic events. This section will focus on Rayleigh wave behaviour in the time-space domain and in the frequency – wavenumber domain, dispersion characteristics for different subsurface structures and the effects of subsurface cavities through literature review and experimental work.

Time Space Domain Analysis

A pulse source generates transient waves and the waves spread away from the source. This process is known as wave propagation. During wave propagation, the waves slowly change as well as maintain similar characteristics. One wave type (such as a P-wave or a Rayleigh wave) in neighbouring traces has a similar shape which is referred to as a wavelet. The same wavelet in all traces can often be linearly connected to form a phase axis. Generally, the phase axis represents the velocity of wave propagation by reciprocal of the phase axis slope. So the steeper the slope is, the lower the velocity is, and vice versa. The peak of the cycle of a wavelet can be used to estimate wave frequencies

Figure 4.1 is a seismic record from sedimentary strata (Liu 2001) which shows three wave types of different apparent velocity and different frequency. The first group is marked as A with the greatest velocity due to the flattest phase axis and with the highest frequencies because of the shortest cycles. This group is direct waves and/or refracted body waves and reflected waves from the shallow interface. Refracted waves usually are characterized as the first linear arrivals whereas reflected waves are in the curve of hyperbola.

Groups B and C are two different modes of Rayleigh waves. B is the higher mode with higher velocity and higher frequency and C is the fundamental mode with the lowest frequency and lowest apparent velocity (refer to Chapter 2 for mode issue).

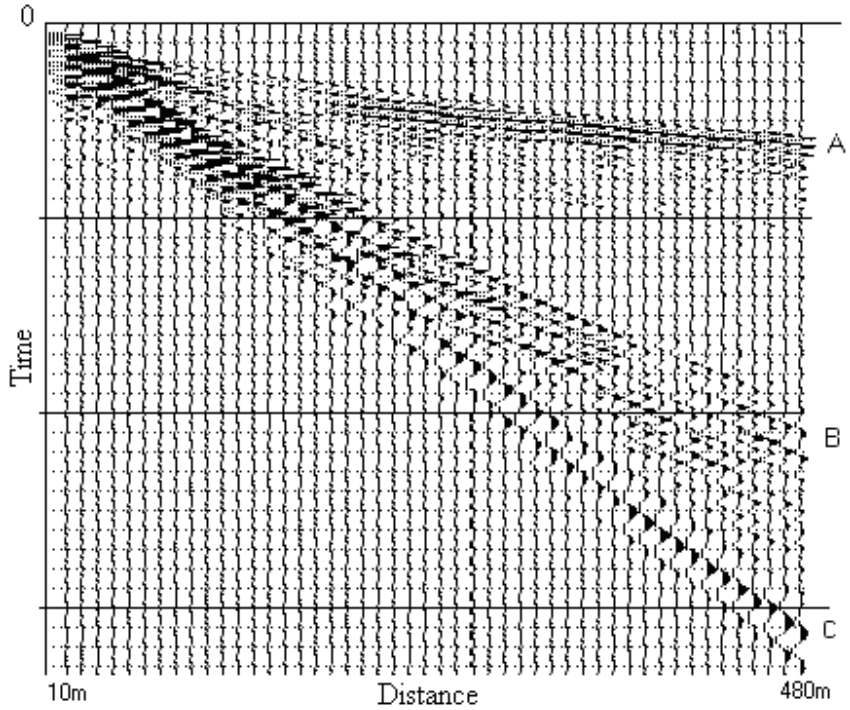

Figure 4.1 A seismic section and its initial evaluation (Liu 2001)

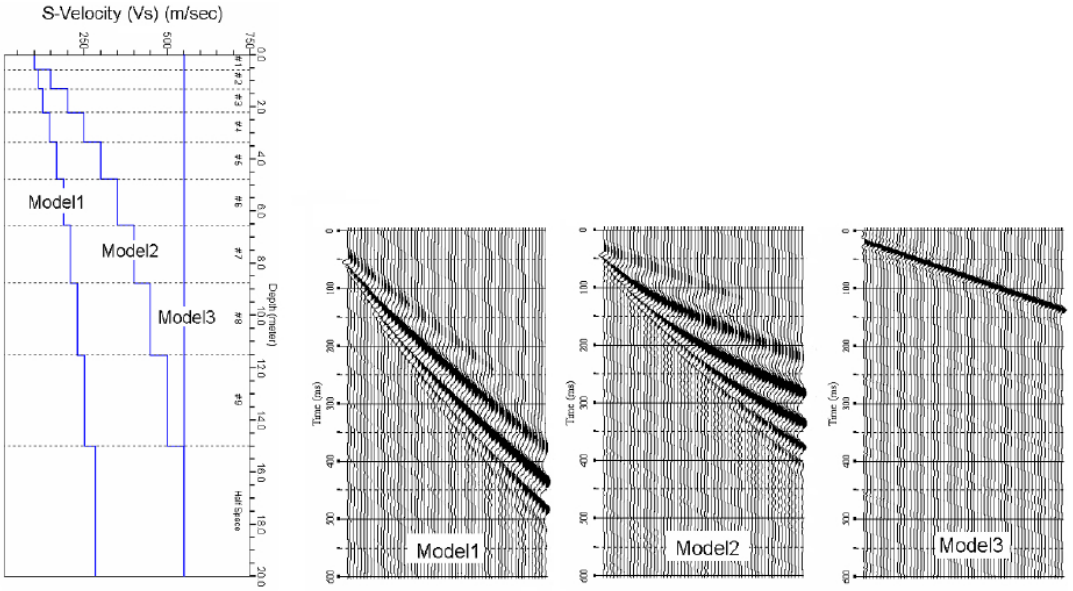

(a) Models (b) Seismic sections for models in (a)

Figure 4.2 Velocity layers influence on dispersion and modes of Rayleigh waves (KGS Workshop, 2005)

Figure 4.2 is a numerical simulation from the Kansas Geological Survey (KGS Workshop, 2005). It illustrates occurrence of dispersion and higher modes of Rayleigh waves due to layered media. Figure 4.2 (a) shows the three different models of media. Model 1 is a medium with slow increase of shear velocity from 100 to 250 m/s with depth from 0 to 20 metre; Model 2 is a medium with faster increase of shear velocity from 100 to 550 m/s with depth from 0 to 20 metre; Model 3 is a medium with constant shear velocity (550m/s). Figure 4.2 (b) shows the corresponding seismic records of (a). Model 3 produces a perfectly linear phase axis, which indicates that there is no dispersion or higher mode because the medium in Model 3 is homogeneous and isotropic, whereas Model 1 and Model 2 produce fan-out wavefields because dispersion occurs in the layered models. Furthermore, Model 2 brings about flatter and wider fan-out waveforms

than Model 1 does since velocity in Model 2 changes faster the Model 1. So the faster the velocity changes in a medium, the wider the wavefield will fan out.

Figure 4.3 shows seismic Rayleigh wave data for different frequencies in a normally horizontally layered medium. The trace spacing is 2 metres. The pulse sources always generate wavefields with a broad range of frequencies. Components of specific frequency ranges can be obtained through bandpass filters of different cutoff frequencies and are used to investigate the performance of Rayleigh waves of different modes with amplitude change. By doing this, it is possible to pick up components of a specific range of frequencies for dispersion estimation in $x - t$ domain while discarding all other components as noise.

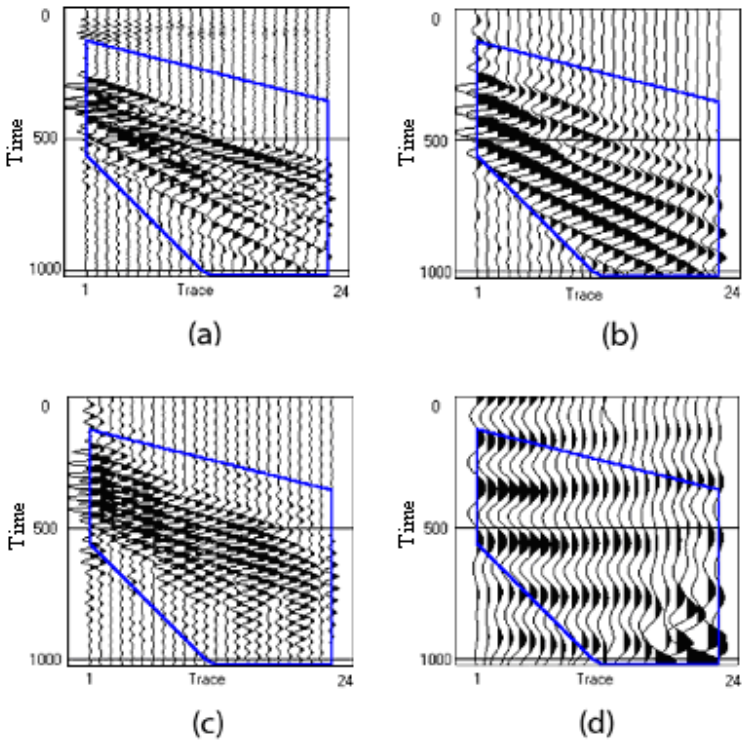

Figure 4.3 Performance of different frequency components in a normally horizontally layered medium: (a) field data, (b) 0-11 Hz lowpass, (c) 11-22 Hz bandpass, (d) 0-3Hz narrow bandpass (Liu 2001).

Figure 4.3 (a) is the original field seismic data including Rayleigh waves and interference between different Rayleigh wave modes and noise. The wavefield inside the blue pentagon mainly consists of Rayleigh waves. The fundamental mode and higher modes of Rayleigh waves are respectively distributed in the lower portion and upper portion of the pentagon. This distribution is caused by the layered strata. The maximum apparent velocity defined by the top line of the pentagon is about 200 m/s and the minimum apparent velocity defined by the left-bottom line in the pentagon is about 50 m/s. Near the top of the pentagon may be direct waves, refraction or reflection from the shallow interface. They travel much faster than Rayleigh waves and can be very weak in seismic surface wave acquisition.

Figure 4.3 (b) shows Rayleigh waves isolated by a narrow lowpass of 0-11 Hz. These frequency components are clearly close to the fundamental Rayleigh wave mode because the wavefield maintains the main structure of the wavefield of lower frequency in (a) but enhances the energy of these components. However, there still exists narrowly fan-shaped distribution, that is, higher modes exist in this frequency range. Figure 4.3 (c) shows Rayleigh waves isolated by a narrow bandpass of 11-22 Hz. These frequency components are mainly energy of higher Rayleigh wave modes. Compared with (a), there also exists the fundamental Rayleigh wave mode of lower frequency and lower velocity even if it is much weaker in energy. After applying 3Hz narrow bandpass filter and a suitable amplitude gain, Figure 4.3 (d) was obtained. Generally all the wavelets with very flat phases have much greater velocities than Rayleigh waves and are distributed throughout the window. These phenomena might be common in urban areas or fields of busy traffic. The phases of low-frequency and great velocity indicate components of long

wavelengths. They could be low-frequency ringing due to shallow portion of the near surface, or side scattered energy from heavy machinery or traffic during seismic data acquisition.

Figure 4.4 shows seismic data from an inversely horizontally layered medium (i.e. the deeper layer has a lower velocity than the overlying layer). There are clearly two phases of different apparent velocities (indicated by two arrows in the figure). The upper phase axis depicts the higher mode Rayleigh waves and the lower phase axis represents the fundamental mode Rayleigh waves. However, the waveform of the higher mode, instead of the fundamental mode, has stronger energy. The interference between the different modes of Rayleigh waves might be noticeable.

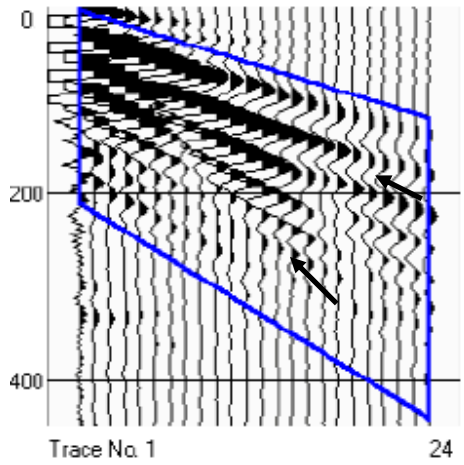

Figure 4.4 Behavior of different frequency components in an inversely layered medium. The two arrows indicate two phases (Liu 2001).

Figure 4.5 is a numerical simulation conducted by Xia et al. (1999). The model is Rayleigh waves propagate from a higher shear velocity into a lower shear velocity of infinite thickness. A yellow vertical line marks the boundary of the two different velocity half spaces. A small reflected surface wave propagates to the left and the transmitted

surface wave propagates more slowly to the right undispersed. This agrees with Chapter 2 about Rayleigh wave propagation with lateral variation.

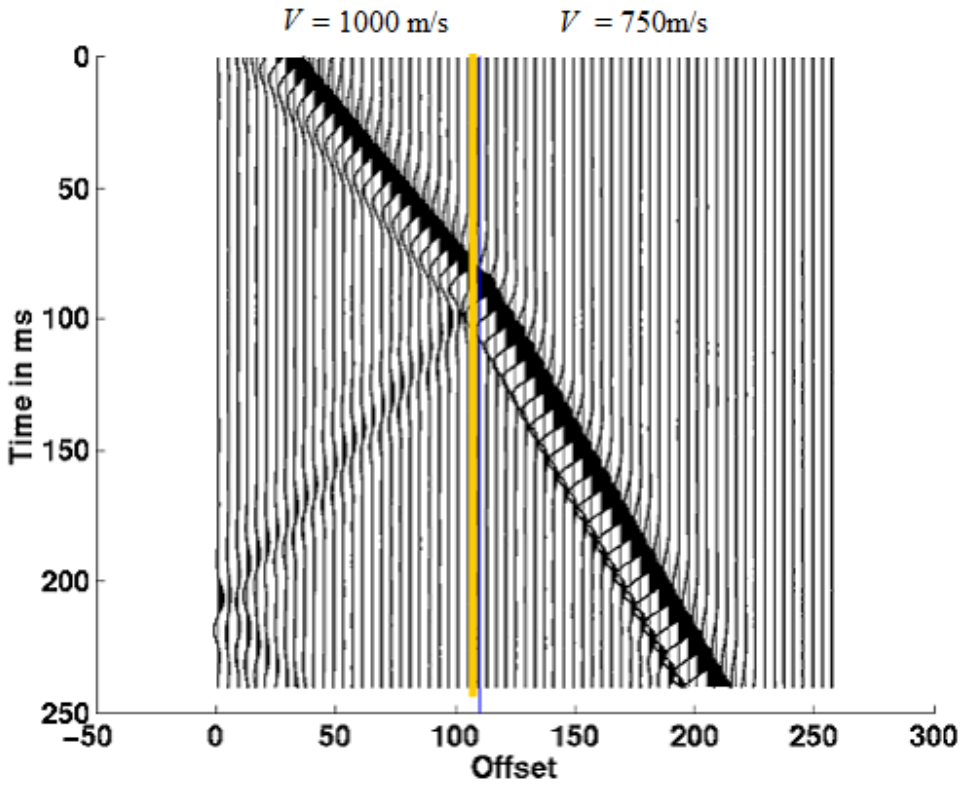

Figure 4.5 Wavefield of performance of different frequency components (Xia et al. 1999)

Analysis of Rayleigh wave behaviours in the x - t domain is very important and helpful to understand the macrostructure of Rayleigh waves and interference phenomena. Result from numerical analysis is also introduced to further understand Rayleigh waves.

Frequency Wavenumber Domain Analysis

Through Fourier analysis, the trace of a seismic signal recorded in time can be regarded as the summation of sine or cosine components of a range of frequencies and can be transformed into spectra in the frequency domain. Correspondingly, waveforms recorded in time space domain by a multichannel-geophone spread can be transformed into a two-dimensional spectrum in frequency wavenumber domain, or *f-k* domain. In *x-t* domain, while one can identify the big picture of the investigated medium as previously discussed, in real cases it is difficult, or even impossible, to completely differentiate the Rayleigh waves of different modes or the interference between them. However, wavefields in the *x-t* domain can be mapped into spectra in the *f-k* domain using a 2D Fourier Transforms. Theoretically, *f-k* mapping separates not only different wave types but also Rayleigh waves of different modes because each wave type has its own frequency band and velocity and each Rayleigh wave mode has a velocity for this frequency.

In the *f-k* domain, usually the horizontal axis is defined as wavenumber and the vertical axis is defined as frequency. Values distributed in the plane defined by the *f* and *k* axes are spectra calculated from 2D Fourier Transform. The resulting plot shows the energy distribution for each frequency along the wavenumber axis. For each frequency, there will be such a wavenumber that the corresponding energy is the maximum value. Hence in *f-k* domain, there exist (*f, k*) pairs that give energy maxima. The energy maxima define the phase velocity. This can be easily deduced as follows:

$$V = \lambda f = \frac{1}{\kappa/2\pi} f = \frac{2\pi f}{\kappa}$$

So the tangents (slops) of the maxima in *f-k* domain times 2π are the phase velocities.

In an infinite homogeneous medium, no dispersion occurs, that is, Rayleigh waves of all frequencies travel at the same velocity, so the maxima of spectra in *f-k* domain tend to be linear. Figure 4.6 shows the experimental result from an infinite halfspace and shows that the fundamental Rayleigh wave mode predominates in the *f-k* domain (Liu 2001). Besides the maxima, there are some other weak energy zones with their secondary maxima also marked as white cross lines, which might be direct P – waves, reflection and noise. Wave types are well separated in *f-k* domain.

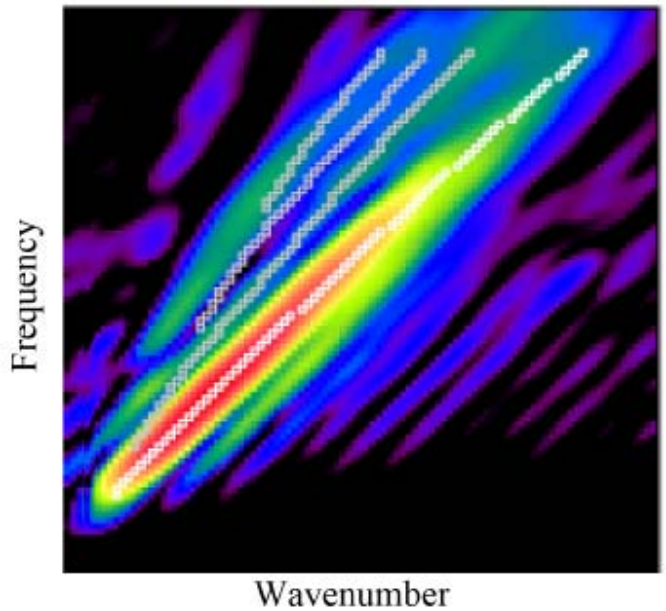

Figure 4.6 Only fundamental mode exists in a homogeneous medium (Liu 2001)

Figure 4.7 represents seismic spectra in the *f-k* domain for a normally layered medium. It clearly shows two predominant energy zones. The lower portion represent Rayleigh waves of fundamental mode and the higher mode is the upper portion. The fundamental

mode has energy maxima of good continuity running through a wide range of frequency and wavelength. For a given frequency in this range, there are two wavenumbers (or two different wavelengths) corresponding to the spectra maxima as shown respectively as the red and the white points. The slope of the line to the red point gives the fundamental mode Rayleigh wave velocity V_f whereas the slope of the line to the white point gives the higher mode Rayleigh wave velocity V_h. In other words, this frequency of Rayleigh wave has two wavelengths and this wave travels at two different velocities, thus Figure 4.7 is also a good representation of the concept of Rayleigh wave modes. Most importantly, the two Rayleigh wave modes are successfully split. After removal of the higher mode Rayleigh waves, the fundamental mode can be used for dispersion curve estimation for this normally layered medium (Liu 2001).

For inversely layered media, the spectra of Rayleigh waves in *f-k* domain are very different from the previous situations. Figure 4.8 shows the spectra in *f-k* domain for an inversely layered medium. Although it clearly shows two predominant energy zones, with the fundamental mode shown in the lower portion and higher mode shown in the upper portion, the higher mode Rayleigh waves have much stronger energy than the fundamental mode Rayleigh waves (Liu 2001).

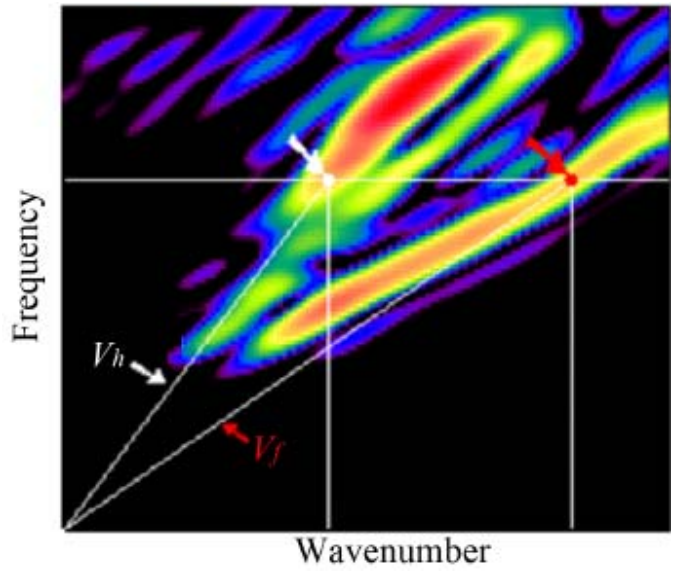

Figure 4.7 More energy continuously distributed as fundamental mode shows a normally layered medium (Liu 2001)

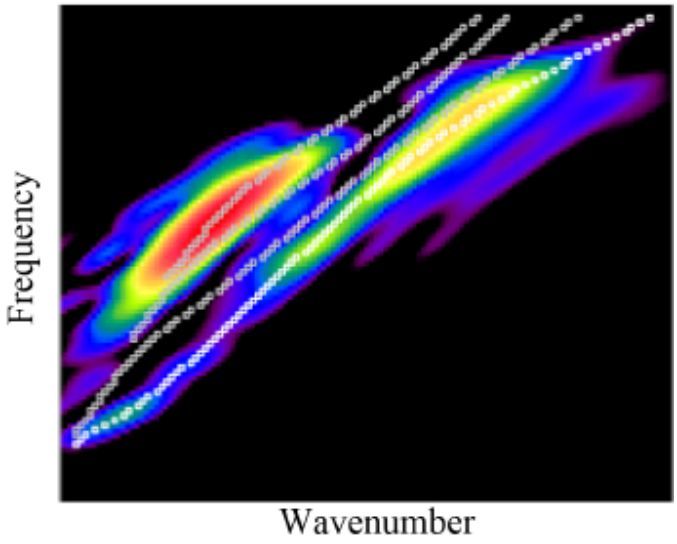

Figure 4.8 Predominant energy in higher mode shows an inversely vertical medium (Liu 2001)

Figure 4.9 schematically shows Rayleigh wave spectra distribution in the *f-k* domain for a medium with a vertical interface with acoustic impedance contrast, where the wave propagates from a higher velocity half space into a lower velocity half-space. There are

three energy maxima lines in the plane respectively marked as I, II and III: Line I is the energy spectrum in the higher velocity space of direct Rayleigh waves, Line II is the energy spectrum in the higher velocity space of back scattered Rayleigh waves and Line III is the energy spectrum in the lower velocity space of transmitted Rayleigh waves. Lines I and II have the same slope value with opposite signs because the direct Rayleigh waves and the back scattering travel in opposite directions.

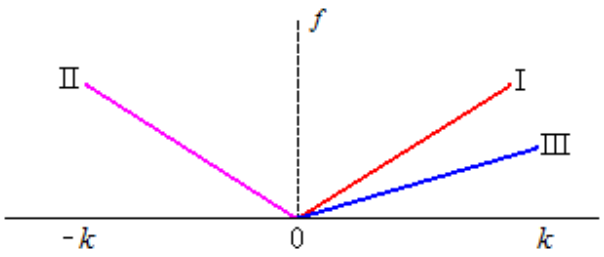

Figure 4. 9 Typical spectra in a medium with a vertical interface

From the above discussion, it is clear that although all surface wave modes in *x-t* domain often interfere with one another, these modes can be separated in *f-k* domain. Analysis in *f-k* domain makes it possible to extract a single-modal dispersion curve of interest.

Dispersion and Near Surface Structure

For near-surface imaging, velocity dispersion is the most important characteristic of Rayleigh waves. It reflects the relationship between Rayleigh wave velocity and frequency or wavelength. Only correct dispersion estimation can yield a correct interpretation for the subsurface structure.

There are two main categories of techniques for determining dispersion. The first technique is called Spectral Analysis of Surface Wave method (SASW) through which

the dispersion curve is obtained using signals from the traces from two geophones at adjacent locations to derive the frequency dependent time delay from the two signals. The dispersion curve in term of phase velocity against wavelength approximately represents how the velocity changes with depth in the section geometrically covered by the two traces. The SASW method requires the medium segment between the two traces to be horizontally homogeneous. In practice, for a uniform field, the spacing between the two traces can be selected longer, whereas for a field with lateral variation, the spacing will have to be selected sufficiently short that the section between the two traces can be treated as uniform.

The second technique is the Multichannel Analysis of Surface Wave method, or modal analysis of surface wave, or MASW method. This method employs a suitable 2-D transform algorithm to map the seismic data from x - t domain into energy spectra in another 2-D plane such as f - k domain, τ - p domain (slant-slowness domain) or f – c domain (phase – shift domain), and then identify the dispersion curve of the most suitable Rayleigh wave modes from the spectral maxima. This dispersion curve represents the whole section covered by the geophone spread in a multichannel survey. However, if a field has lateral variation, the dispersion curve gives rise to uncertainty and error.

Generally, a field to be investigated can be divided into many segments, each of which can be considered to be uniform, then dispersion curves can be calculated for each segment. Finally all these dispersion curves are geometrically arranged to form a dispersion section that can be used to invert and map the investigated field as a shear velocity field (SVF). The following sections give more details about this processing.

Based on the above discussion, dispersion curve estimation can be simplified into two types of media: horizontal layers with velocity increasing with depth or horizontal layers with velocity decreasing with depth. Figures 4.10 and 4.11 are results from numerical simulation of these two types. The software was coded in Matlab (Rix, 1999).

Thickness (m)	5	10	∞
V_S (m/s)	350	400	450
V_P (m/s)	600	700	800
Density (Mg/m^3)	1.8	1.8	1.8

(a)

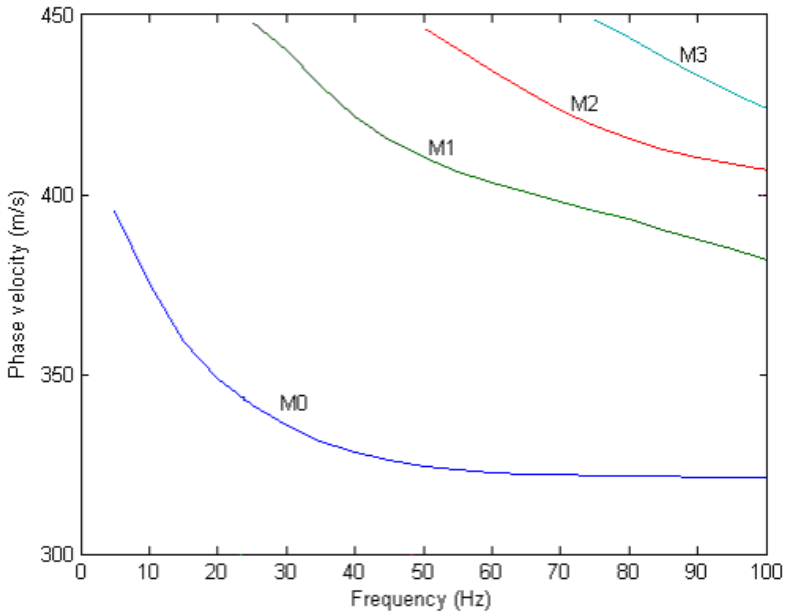

(b)

Figure 4.10 Typical spectra in a medium with two horizontal interfaces (M0 = the fundamental mode, M1, M2, M3 = higher modes)

The numerical simulation results allow evaluation of the following three aspects:

i) How the modal Rayleigh wave velocities change with frequency.

ii) How Rayleigh wave modes are affected by vertical elastic variations.

iii) How many modes and which modes are predominant.

The surface wave dispersion curves are often expressed as a function of velocity (V_R) with frequency (f) and mapped in f-V_R plane. Figure 4.10 shows the numerical modelling result of normally layered vertical strata and indicates there are many modes from fundamental mode M0 to higher modes M1, M2, M3, etc. As expected, Figure 4.10 shows that, for the free Rayleigh modes in this normally dispersive case, there are higher modes with frequency increase whereas the fundamental Rayleigh mode is dominant over the whole frequency range and the phase velocity of the fundamental Rayleigh mode coincides with model (a): the phase velocities at 10 Hz and 50 Hz are 370 m/s and 325 m/s, corresponding to the two layers.

Apply Equations 2.20 to estimate Rayleigh wave velocities for the two layers from the fundamental Rayleigh mode dispersion curve M0 in Figure 4.10,

$$\frac{V_S}{V_P} = \sqrt{\frac{\mu}{\lambda + 2\mu}} = \sqrt{\frac{1-2\upsilon}{2(1-\upsilon)}} \qquad (2.20)$$

$$\Downarrow$$

$$\frac{350}{600} = \sqrt{\frac{1-2\upsilon_1}{2(1-\upsilon_1)}} \text{ and } \frac{400}{700} = \sqrt{\frac{1-2\upsilon_2}{2(1-\upsilon_2)}}$$

$$\Downarrow$$

$$\upsilon_1 = 0.24 \text{ and } \upsilon_2 = 0.26$$

This numerical simulation for normally layered strata shows what the dispersion curves look like and proves that the fundamental Rayleigh mode is predominant and so can be used to characterize this type of media in practice.

$$V_R = \frac{0.862 + 1.14\upsilon}{1+\upsilon} V_S \qquad (2.21)$$

$$\Downarrow$$

$$V_{R1} = 321\,\text{m/s} \text{ and } V_{R2} = 368\,\text{m/s}$$

To represent the case of a soft layer trapped between two stiffer ones, two layers over a halfspace have been considered in Figure 4.11(a).

First use equations (2.20) and (2.21) to estimate Rayleigh wave velocities for the different layers,

$$\frac{V_S}{V_P} = \sqrt{\frac{\mu}{\lambda + 2\mu}} = \sqrt{\frac{1-2\upsilon}{2(1-\upsilon)}} \qquad (2.20)$$

$$\Downarrow$$

$$\frac{400}{700} = \sqrt{\frac{1-2\upsilon_1}{2(1-\upsilon_1)}}, \frac{300}{500} = \sqrt{\frac{1-2\upsilon_2}{2(1-\upsilon_2)}} \text{ and } \frac{400(450?)}{800} = \sqrt{\frac{1-2\upsilon_3}{2(1-\upsilon_3)}}$$

$$\Downarrow$$

$$\upsilon_1 = 0.26, \upsilon_2 = 0.22 \text{ and } \upsilon_3 = 0.27$$

and

$$V_R = \frac{0.862 + 1.14\upsilon}{1+\upsilon} V_S \qquad (2.21)$$

$$\Downarrow$$

$$V_{R1} = 367 \text{ m/s}, V_{R2} = 274 \text{ m/s} \text{ and } V_{R3} = 414 \text{ m/s}$$

Thickness (m)	5	10	∞
V_S (m/s)	400	300	450
V_P (m/s)	700	500	800
Density (kg/m³)	1.8	1.8	1.8

(a)

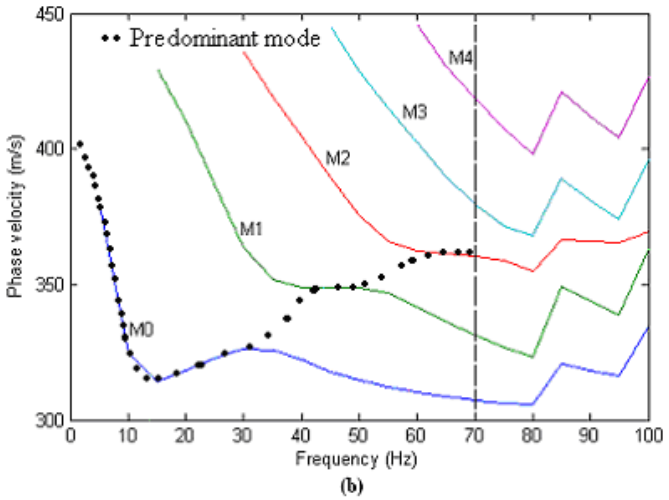

(b)

Figure 4.11 Typical spectra in a medium with a horizontal intermediate layer

Figure 4.11(b) is the numerical modeling result of the free Rayleigh wave modes in this inversely dispersive case, there are higher modes with frequency increase whereas neither the fundamental Rayleigh mode nor any higher Rayleigh mode is dominant over the whole frequency range and gives phase velocities that coincide with the analysis. However, if higher modes are considered together with the fundamental Rayleigh mode for different frequencies, it is possible to approximately pick up the correct Rayleigh wave velocities for the different layers. Now exam the dispersion curves in Figure 4.11b.

The zig-zig shape at high frequency is due to layer variation and apparent fluctuation at frequencies greater than 70 Hz. This fluctuation phenomenon is because the numerical modeling program ignored Rayleigh mode leak in inversely layered vertical media. Theoretically, the leaky surface wave arises from the complex conjugate roots of the Rayleigh equation. The complex conjugate roots give rise to a wave that propagates along the surface and is coupled to a plane shear wave in the medium. Due to the coupling, the surface wave leaks energy into the medium and is highly inhomogeneous (Schröder and Scott, 2001). This omission caused uncertainty and error in the dispersion curve analysis of this numerical simulation.

The main difference compared to the case of the normal dispersion profile is that there is not a single dominant mode. For this situation, it is possible to obtain the dispersion curves relative to different modes shown in black dots in Figure 4.11b from f –k spectra, which are represented in the spectrum by local maxima as discussed in Section 3.2. Although in this case the fundamental mode is not predominant over the entire range of

frequency, for higher frequencies there is a transition towards higher modes. In the frequency range of interest, the behaviour is dominated by the fundamental and the first and second higher modes and the transition between the fundamental, the first order and the second order higher modes is concentrated in the frequency range between 40 and 70 Hz. Clearly, for a given frequency, the local maximum corresponding to the fundamental mode is the one that is associated with the highest wavenumber, because the fundamental mode has the lowest phase velocity, whereas the local maximum corresponding to the successive higher modes is associated with the higher wavenumber. The possibility of evaluating the phase velocity associated with different modes would be very interesting in the view of the inversion process, indeed more information than the single effective phase velocity would result in a better posed mathematical problem to be solved (Foti 2000).

The numerical simulation showed the dispersion profiles are strongly affected by the elastic properties of a medium. The dispersion tendency of Rayleigh wave modes was also evaluated and the dispersion features reflect the elastic properties of this medium. This is the basic principle of inversion algorithms, by which a physical model can be constructed for interpretation purposes.

Rayleigh Wave Performance on Geological Fractures and Anomalies

Cavity Effect on Seismic Section

Figure 4.12 is a synthetic shot gather from Xia et al 2007. A square cavity of 6 m × 6 m with a depth to the top of the cavity of 12 m in a homogeneous half space was modeled at a trace spacing of 2.5 metres. P- and S-wave velocities of the homogenous halfspace were assumed to be 1000 m/s and 200 m/s, respectively. These values defined a Rayleigh-wave velocity of 190 m/s based on Equation (2.20).

To avoid numerical difficulties, P- and S-wave velocities of the cavity were assumed at 340 m/s and 17 m/s (actually S-velocity is 0), respectively. Densities of the half space and the cavity were respectively 2000 kg/m^3 and 10 kg/m^3. Synthetic seismographs simulated the following field layout. Sixty vertical component geophones were located in the middle of the subspace from 21 m to 80 m with an interval of 1m. The cavity was at the centre of the geophone spread with different depths. A source was described by the first-order derivative of the Gaussian function $t \cdot \exp(-\alpha t^2)$ with a central frequency of 25 Hz and was set at 20 m from the first geophone. The synthetic medium conditions and data acquisition configurations produced a seismic section. As expected, a hyperbola representing diffraction travel time curve can be traced in this section. Three patterns of Rayleigh waves can be seen: in Figure 4.12, direct Rayleigh waves DR, back scattered Rayleigh waves BR and transmitted Rayleigh waves TR.

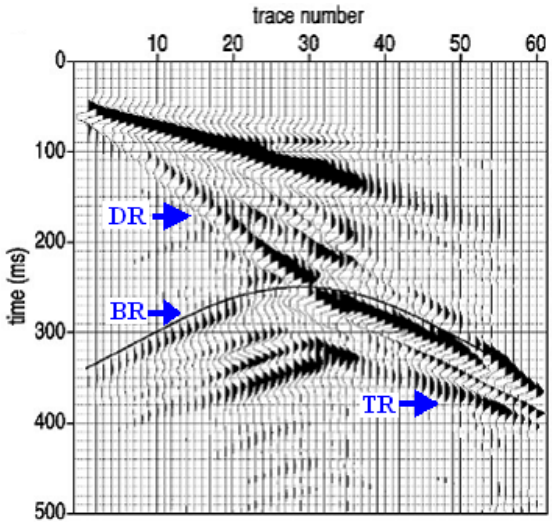

Figure 4.12 A synthetic shot gather of a 6m x 6m cavity at the depth of 12m in a homogeneous half space with a hyperbolic diffraction travel time curve. DR, BR and TR are respectively direct Rayleigh waves, back scattered Rayleigh waves and transmitted Rayleigh waves (after Xia et al 2007).

Fault Effect on Seismic Section

Figure 4.13 shows another numerical modeling study, with a fault as an anomaly (Xu et al 2005). The earth surface intersection point of the fault is at the centre point of the 60-station-receiver spread. The sources are marked as O_1 as the "left" source and O_2 for the "right", respectively. The modeling parameters are the same as the homogenous half-space, as shown in the figure.

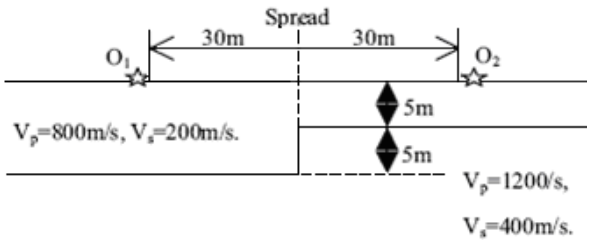

Figure 4.13 Fault model and layout of sources and receivers (Xu and Miller, 2005)

Scattering events that spread from the middle to the left quadrant can be seen in the seismic section excited by the left source (Figure 4.14a), but it is difficult to identify scattering events for the right source (Figure 4.14b).

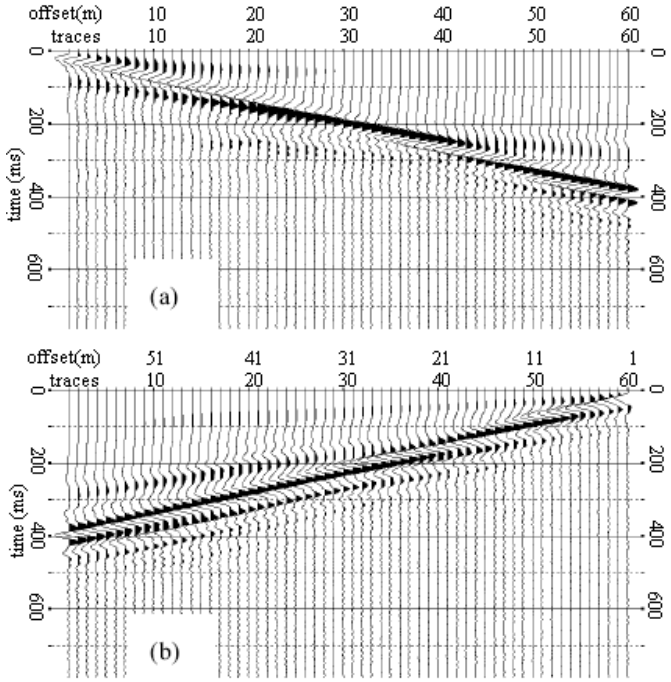

Figure 4.14 Seismic sections of the corner-edge model in Figure 4.13 for different source layouts with (a) the left source and (b) the right source (Xu and Miller, 2005)

The estimated fault effect dispersion curves were shown in Figure 4.15. When the frequencies are outside of the frequency range from 9 to 18 Hz, the dispersion curves, from sources on the left and right sides, approach the same Rayleigh wave phase velocities for the top layer and the bottom half-space. However these two dispersion curves have different phase velocities within the middle frequency band (9 to 18 Hz). It has been suggested that the dispersive characterizations of Rayleigh waves excited by the left source would be determined mainly by the left portion of subsurface structures; whereas the dispersive characterizations of Rayleigh waves excited by the right source are determined mainly by the right portion of subsurface structures.

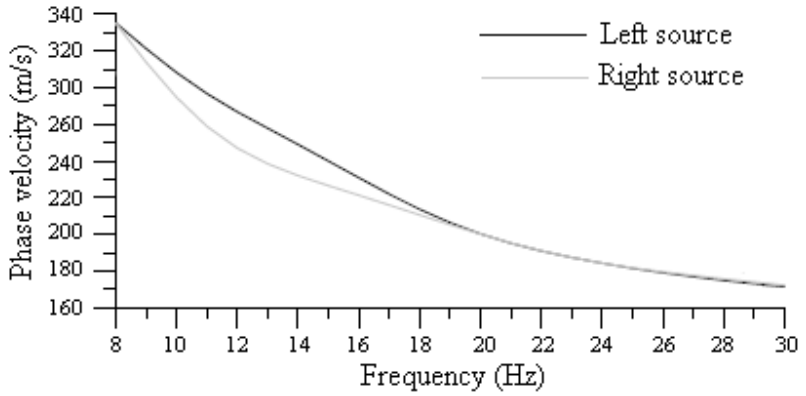

Figure 4.15 Effect dispersion curves for different source layouts with (a) the left source and (b) the right source (Xu and Miller, 2005)

In summary, the phase velocity of Rayleigh waves can be measured at about 321 m/s at 9 Hz from the record excited by the left source which gives a penetration depth to the top of the lower half-space at about 17.8 m. However, the phase velocity of Rayleigh waves

can be measured about 210 m/s at 18 Hz from the record excited by the right source which gives a penetration depth to the top of the lower half-space at about 6.4 m.

The Cavity Effect on Dispersion Curves for Different Vertically Layered Media

Three models show the effect of cavities when Rayleigh waves propagate in different media in Figure 4.16 (Xu et al 2008). These models illustrate how a cavity affects Rayleigh waves in term of SVF to be expected for propagation from left to right. The profile (a) is a cavity inside a homogeneous medium. To the left side of the cavity (Zone I), Rayleigh wave velocity is constant. When Rayleigh waves approach the cavity, the velocity decreases with depth, and at some point decreases to zero (Zone II) for lack of shear strength in the cavity filled with air or water. After passing through the cavity to the right side of the cavity (Zone III), Rayleigh waves spread out due to diffraction and transmission, and the propagation gradually returns to the right at the same constant velocity as that in zone I. The middle profile (b) is a cavity inside a normal medium whose velocity in the layers increases with depth. In the left side of the cavity (Zone I), Rayleigh wave velocity increases with depth. When Rayleigh waves approach the cavity, the velocity decreases with depth, and at some point, decreases to zero (Zone II). After passing through the cavity to the right side of the cavity (Zone III), Rayleigh waves spread out and return to the same way as in Zone I. The rightmost profile (c) is a cavity inside a medium whose velocity in the layers decreases with depth. In the left side of the cavity (zone I), Rayleigh wave velocity decreases with depth. When Rayleigh waves approach the cavity, the velocity decreases faster with depth, and at some point, decreases to zero (Zone II). After passing through the cavity to the right side of the cavity (Zone

III), again, Rayleigh waves spread out and return to the same way as in zone I. The last profile is a difficult situation in that Rayleigh wave velocity variations have the same trend along the whole profile. If the cavity is small and has a minor effect on the wave propagation, possibly, this can be quantified from numerical or experimental studies, but the exact nature or the presence of the cavity may not be observed.

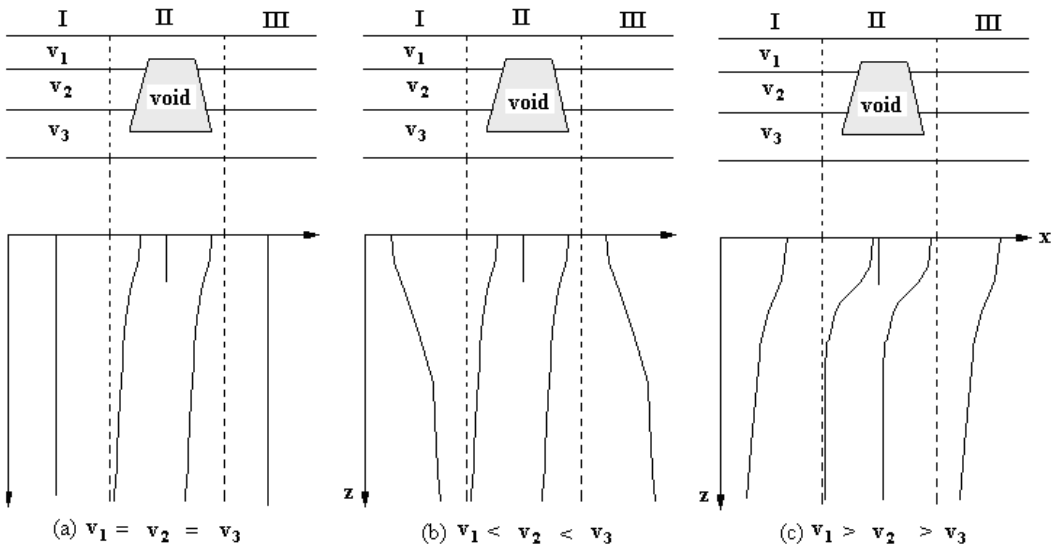

Figure 4.16 Theoretical cavity effects on Rayleigh wave propagation in three different medium profiles (Xu et al. 2008)

There is a sharply dissipative characteristic due to scattering between interface and absorption through the medium. There could be some danger that the Rayleigh waves may become so attenuated after a small cavity or small fractured zone that Rayleigh waves could not be detected.

To sum up, subsurface cavities present sharp change in porosity or density from their surroundings and can cause energy scattering and energy absorption in the proximity of the cavities. As a result, the noticeable contrast in shear wave velocity can be observed in

a vertical section of one cavity. This dispersion anomaly can be used for a quantitative interpretation of the lateral variation of a medium, a cavity or some other subsurface features.

Cavities impose significant and complicated impacts on wave propagation through the medium. A main difficulty in detection of subsurface cavities is heterogeneity and anisotropy. In this situation, Rayleigh waves become so complicated that it is difficult and even impossible to build a mathematical formulation (Foti 2000). So far, most studies have investigated how Rayleigh waves behave in transversely isotropic and vertically heterogeneous media (Lai, 1998), and a dispersion equation also has been constructed. These achievements lay a foundation, both in theory and in practice, for my investigation. It is possible to understand how subsurface cavities affect Rayleigh wave propagation through numerical simulation, then take measurements of Rayleigh wave dispersion curves and finally give a reasonable interpretation for geomechanical properties of a medium as well as localize subsurface cavities in the medium by Rayleigh wave methods. This thesis does not intend to cover the theory of numerical simulation of Rayleigh wave propagation.

CHAPTER 5: DISPERSION ESTIMATION AND SHEAR VELOCITY FIELD MAPPING

For anomaly localization, the processing strategy involves detection of frequency variation locally in time. Classical Fourier analysis uses the basic functions $\sin(\omega t)$, $\cos(\omega t)$, or $\exp(i\omega t)$. In the frequency domain, these functions work well. The functions are suitable for the analysis and synthesis of signals with a simple spectrum. However, these functions are not localized in the time domain, that is, it is difficult to use them in analysis or synthesis of complex signals which have fast local variations such as transients or abrupt changes. To overcome this difficulty, it is possible to "window" the signal using a regular smooth function, which is zero or nearly zero outside a time segment of interest. The windowed Fourier Transform permits the description of a non-stationary signal in both time and frequency domains. However, the uncertainty principle prevents obtaining a complete description of the signal in the associated dual domain. It is inherently difficult to determine the entire frequency information of the signal over a short duration, or locally in time using this method. The wavelet transform, however, is able to represent signals localized in both time and frequency domains. Applications of the wavelet theory and related concepts are numerous, including image processing, signal processing, data compression, and enhancing the accuracy and speed of numerical solution of engineering problems. This chapter briefly introduces Short Time Fourier Transform (STFT) and its shortcoming, and then discusses Continuous Wavelet Transform (CWT), based on which a dispersion calculation method is introduced. Finally, shear velocity mapping is presented.

Continuous Wavelet Transforms

The STFT has long been regarded as a powerful spectral analysis tool. It is necessary to give a brief introduction to this transform and then go to the wavelet transforms in comparison.

Short Time Fourier Transform

Fourier Transform can only produce the entire spectrum of a signal with difficulty in obtaining the frequency content locally in time, or local signal characteristics, especially for chop signals and non-stationary signals. Hence, for stationary signals, Fourier transform is satisfactory for it reflects the overall signal characteristics of the entire time whereas, for non-stationary signals, Fourier transform becomes inadequate. In order to overcome this weakness of the conventional Fourier transform, time-frequency transform came into practice, among which windowed Fourier Transform, or Short Time Fourier Transform (STFT), is the most used in non-stationary signals. This STFT technique was used in the author's M.A.Sc research (Xu 2004). In order to compare with the Wavelet Transforms, the STFT is briefly discussed here.

The STFT of a signal $x(t)$ using a window function $g(t)$ with length s is defined as follows:

$$STFT(f,s) = \int_{-\infty}^{\infty} x(t)g(t - s)e^{-i2\pi ft}\,dt \qquad (5.1)$$

During the window $g(t)$ sliding along the signal $x(t)$, and for each shift $g(t\text{-}s)$, the product function $x(t)\ g(t\text{-}s)$ is computed using the Fourier Transform. After simple manipulation, Equation (5.1) can be rewritten as

$$\begin{aligned} STFT(f,s) &= \int_{-\infty}^{\infty} x(t)g(t-s)e^{-i2\pi ft}dt \\ &= e^{-i2\pi fs}\int_{-\infty}^{\infty} x(t)g(t-s)e^{-i2\pi f(t-s)}dt \end{aligned} \tag{5.2}$$

Equation (5.2) is actually, aside from the initial phase factor $e^{-i2\pi fs}$, the convolution of the signal with the frequency shifted and time reversed window function. It can be graphically shown in Figure 5.1. The magnitude of this distribution is called the spectrogram.

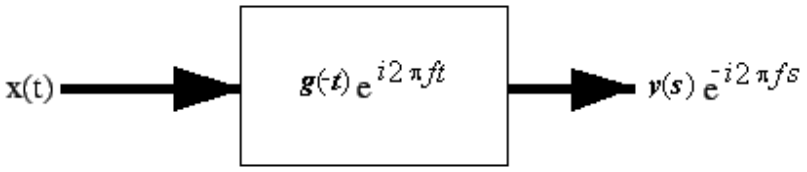

Figure 5.1 Filter interpretations of STFT (Phillips 2005)

Window length s defines resolution in the spectrogram. In the case where the signal consists of two frequencies f_1 and f_2, the windowed transform is the superposition of two shifted signals. The individual frequencies cannot be resolved unless $|f_1 - f_2| > 1/s$. In fact, for adequate separation it has to be set $|f_1 - f_2| > 2/s$. There is always a trade-off

between time resolution and frequency resolution: if a window of length s is used, then a time-resolution of s is obtained with a frequency resolution of $1/s$ (Phillips, 2005).

Figure 5.2 is an example demonstrating the shortcoming in resolution of STFT. A signal is supposed to be the sum of two sinusoids of frequencies f_1 = 500Hz and f_2 = 1000Hz and two impulses at times t_1 = 125 ms and t_2 = 130 ms. A box type window, separately with two window lengths of s_1 = 2.5 ms and s_2 = 8 ms, is used to determine the corresponding spectra in Figure 5.2. The left spectrogram (a) gave good time resolution but poor frequency resolution and the right spectrogram (b) was the opposite. Figure 5.3 shows the 3-D spectrogram from the window size for s_1 = 2.5 ms, which more straightforwardly indicates the uncertainty principle: it is impossible to obtain satisfactory images both in frequency and time.

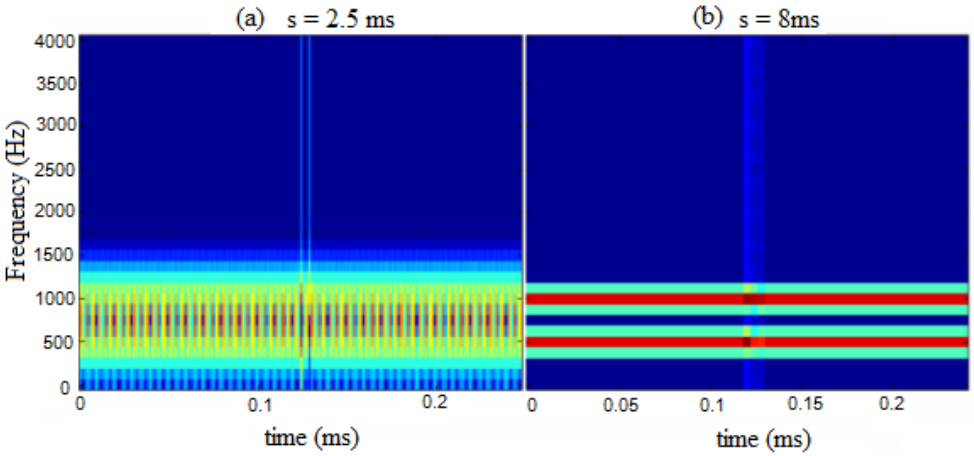

Figure 5.2 Spectrogram resulting from two different window sizes: (a) s = 2.5 ms, (b) s = 8 ms

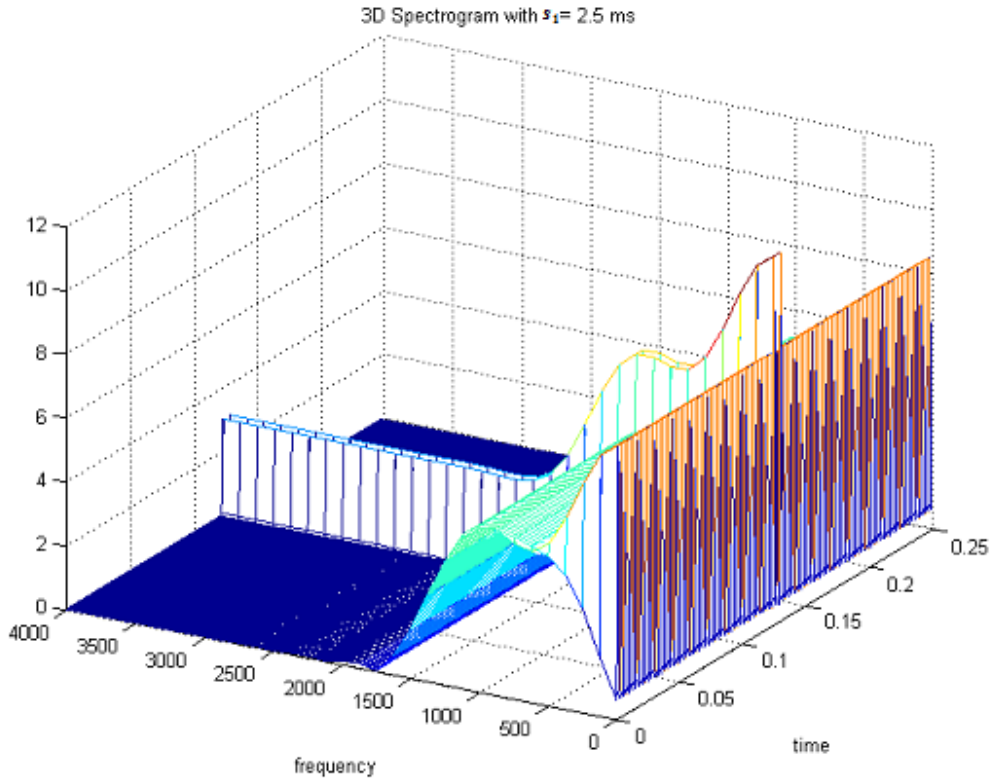

Figure 5.3 3-D spectrogram resulting from window size of s_1 = 2.5 ms

Therefore, the STFT analysis does not fundamentally solve the inherent problems with non-stationary waveforms. The wavelet transforms is necessary to overcome the shortcomings of conventional Fourier analysis.

Continuous Wavelet Transform

A wavelet is defined as a waveform of effectively limited duration that has an average value of zero. Compared with sine waves, the basis of Fourier analysis, which do not have limited duration, wavelets can be irregular and asymmetric. While Fourier analysis

breaks up a signal into sine waves of various frequencies, wavelet analysis breaks up a signal into shifted and scaled versions of the original (or mother) wavelet.

Similar to Fourier transform, the Continuous Wavelet Transform (CWT) is defined as the sum over all time of the signal multiplied by scaled, shifted versions of the wavelet function,

$$C(a,b) = \frac{1}{\sqrt{a}} \int_{-\infty}^{\infty} x(t) w\left(\frac{t-b}{a}\right) dt \qquad (5.3)$$

where the function $w(t)$ is the mother wavelet and is taken to be a "small wave", a is the scale vector and b is the shift vector.

Similar to STFT, CWT can be also regarded as a filter divided by a scale factor. This concept is shown in Figure 5.5.

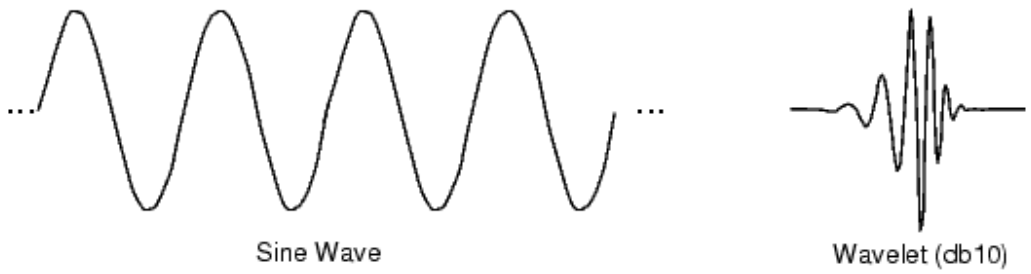

Figure 5.4 Sine base for Fourier analysis compared with db10 wavelet

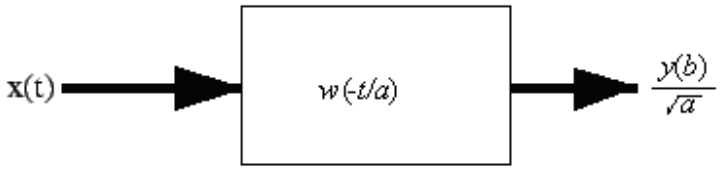

Figure 5.5 Filter interpretations of CWT (Phillips 2005)

The results of the CWT gives many wavelet coefficients *C*, which are a function of scale *a* and position *b*. CWT provides a time-scale description with several important properties (Phillips 2005):

i) Frequency is related to scale which may have a better relationship to the problem at hand compared to STFT. The higher scales correspond to the most stretched wavelets. The more stretched the wavelet, the longer the portion of the signal with which it is being compared, and thus the coarser the signal features being measured by the wavelet coefficients. Thus, there is a relationship between wavelet scales and frequency in the following way:

   Large scale *a* in Equation (5.3) defines a compressed wavelet and results in rapidly changing details of high frequency; small scale *a* in Equation (5.3) defines a stretched wavelet and results in slowly changing and coarse features of low frequency. Mathematically, the relationship between scale *a* and corresponding frequency f_a can be calculated by the center frequency f_c of a wavelet and the sampling frequency f_s

$$f_a = \frac{f_c}{a} f_s \quad \text{or} \quad a = \frac{f_c}{f_a} f_s \tag{5.4}$$

ii) The CWT is able to resolve both time and scale (or frequency) events better than the STFT. In the STFT, the frequency band has a fixed width, but in the CWT, the frequency bands grow and shrink with the scale being used. This allows good frequency resolution at low frequency and good time resolution at high frequency. Consequently the wavelets are able to determine if an anomalous event exists in a signal, and if so, can localize it. So wavelet analysis is more suitable than Fourier Transform for seismic Rayleigh wave processing for anomaly detection and imaging, in particular for those signals that have a sharp transition and a low frequency components.

To demonstrate this point, Figure 5.6 is an example of Morlet waveform compared to STFT. The Morlet wavelet has formula: $w(t) = -e^{-t^2/2}$. It is also a small wave since the Gaussian exponential, $e^{-t^2/2}$ is effectively zero outside the interval $-3 < t < 3$. The signal (a) consisted of two frequencies with a frequency transition at $t = 500$. Conventional Fourier transform gave the spectrum (b) of the signal and indicated the two frequencies, but there is no time information in the spectrum. STFT produced the spectrogram (c) with clear frequency transition; however there was no frequency differentiation.

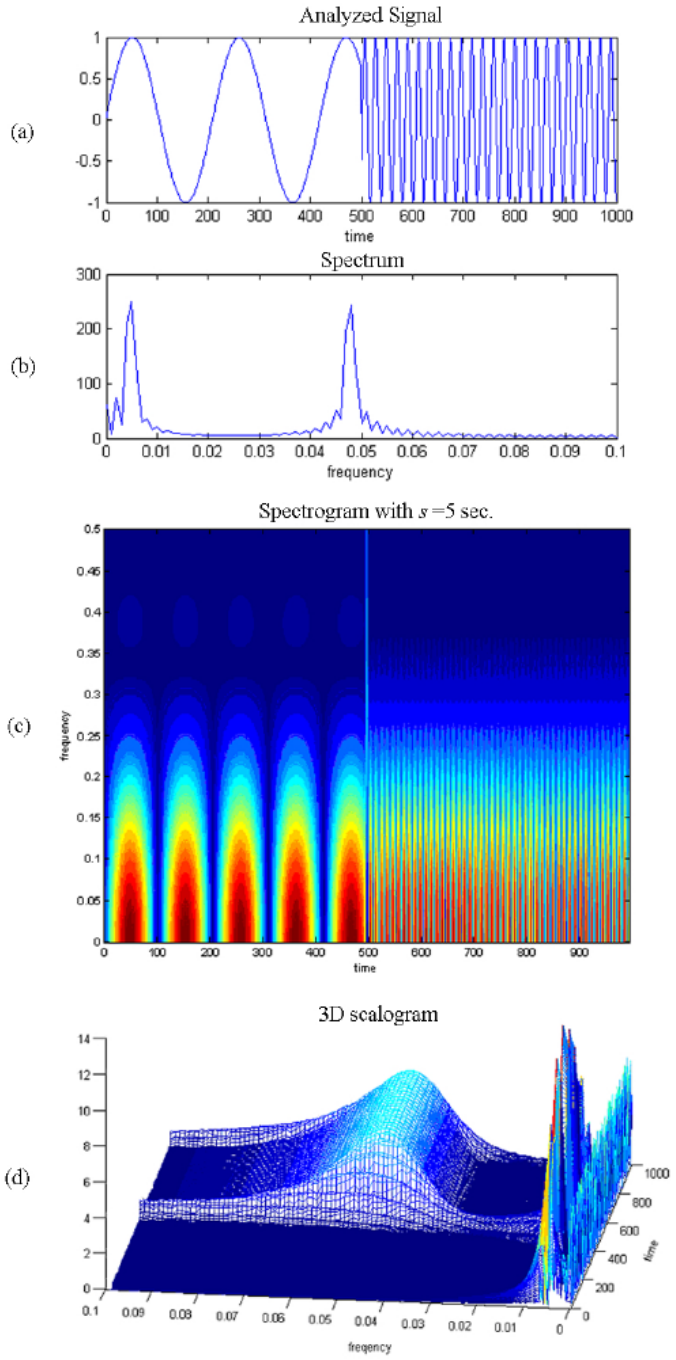

Figure 5.6 Comparison of Morlet wavelet and the STFT for detecting frequency transition: (a) signal, (b) frequency spectrum, (c) STFT spectrogram and (d) CWT scalogram from Morlet wavelet

Morlet wavelet transform generated the scalogram (d) with the evident transition in both time and frequency domain. The scalogram has the same defination as spectrogram. The difference of the scalogram is the magnitude distribution over scale instead of frequency.

iii) Multiresolution is one of the most important properties of wavelets. Typically a set of baby wavelets is defined by choosing the scales to be powers of 2 and the times to be integer multiples of the scales. Signals are sampled in discrete dataset, so the discrete wavelet transform (DWT) is applied for signal processing. A discrete signal is given:

$$f(t)=\sum_{j,k} c_k^j w_{j,k}(t);\ w_{j,k}(t)=2^{j/2} w\left(2^j t-k\right) \tag{5.5}$$

where c_k^j = coefficients, $w(t)$ = *mother wavelet,* j = scale, and k = shift

The function $w(t)$ in Equation (5.5) defines a large class of wavelet functions for which the set of baby wavelets is an orthogonal basis. With these wavelets, usual analysis-synthesis can be conducted for all signals:

Analysis:

$$c_k^j=2^{-\frac{1}{2}}\sum_n c_n^{j+1} h_{n-2k};\ d_k^j=2^{-\frac{1}{2}}\sum_n c_n^{j+1} g_{n-2k}\quad (k=0,1,\cdots,N-1) \tag{5.6}$$

where $\{h_n\}$ and $\{g_n\}$ are conjugate complex of responses of lowpass filter and highpass filter. Assume $\left\{c_k^{j+1}\right\}, \{h_n\}$ and $\{g_n\}$ are known.

Synthesis:

$$
\begin{aligned}
x(t) &= \sum_{i=-\infty}^{j}\sum_{k} c_{i,k} w_{i,k}(t) \\
&= \sum_{i=-\infty}^{j-1}\sum_{k} c_{i,k} w_{i,k}(t) + \sum_{k} c_{j,k} w_{j,k}(t) \\
&= \sum_{i=-\infty}^{j-2}\sum_{k} c_{i,k} w_{i,k}(t) + \sum_{k} c_{j\text{-}1,k} w_{j\text{-}1,k}(t) + \sum_{k} c_{j,k} w_{j,k}(t) \qquad (5.7) \\
&\quad \vdots \\
&\quad \vdots
\end{aligned}
$$

As defined in Equation 5.8, A_j is the set of all signals, $x(t)$, which can be synthesized from the baby wavelets $w_{i,k}(t)$ where $i < j$ and $-\infty < k < \infty$. Then the spaces A_j are nested inside each other. As j goes to negative infinity A_j expends to become all space L^2 while j goes to infinity A_j shrinks down to only the zero signal (Figure 5.7).

$$\{0\} \cdots \subset A_2 \subset A_1 \subset A_0 \subset A\text{-}_1 \subset A\text{-}_2 \subset \cdots \subset L^2 \qquad (5.8)$$

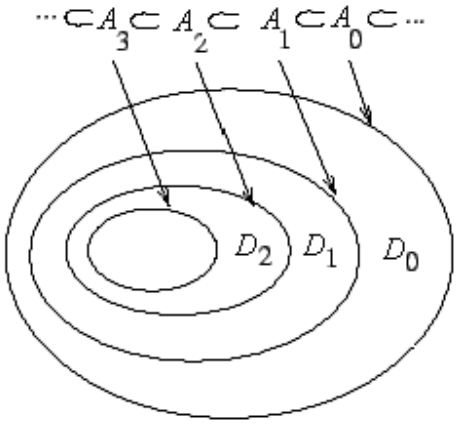

Figure 5.7 Nested subspace (after Phillips 2005)

Figure 5.7 schematically describes this space concept. D_j is the difference between adjacent spaces A_{j+1} and A_j. This nested sequence of subspaces makes sense to understand multiresolution for analyzing signals.

When function $D_i(t)$ is related to the detail at level i and $A_i(t)$ is related to the approximation at level i, L^2 is the signal itself in terms of infinite energy. This leads to various decompositions of this signal:

$$\begin{aligned} x(t) &= A_1(t) + D_1(t) \\ &= A_2(t) + D_2(t) + D_1(t) \\ &= A_3(t) + D_3(t) + D_2(t) + D_1(t) \\ &\quad \cdots \cdots \cdots \cdots \cdots \cdots \end{aligned} \tag{5.9}$$

This decomposition process is shown in Figure 5.8, which illustrates a three-level decomposition of signal x. The signal x can be obtained from superposition of successive high and low pass components as described below.

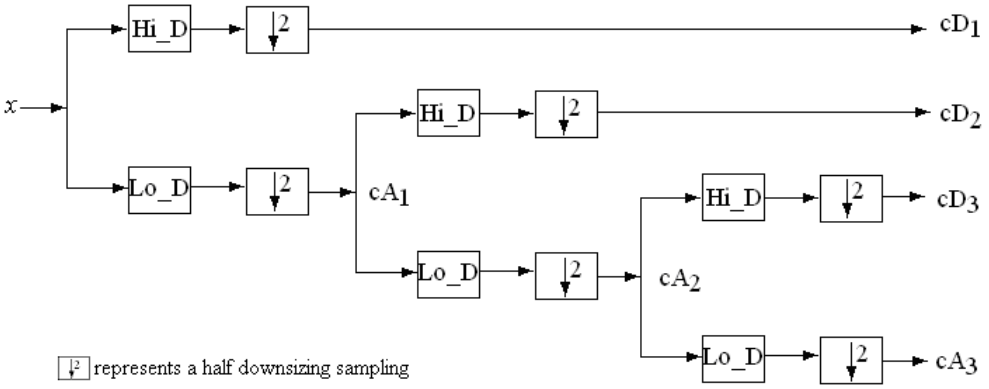

Figure 5.8 Decompositions of a signal using CWT in term of highpass and lowpass filters (Phillips 2005).

The original signal x coefficients pass a highpass filter $h_1(n)$ and then they multiply a wavelet $w(t)$ at (j-1) scale, then we get D_1. Meanwhile, the signal coefficients pass a lowpass filter $h_0(n)$ to the $(j\text{-}1)^{th}$ to produce A_1. In the next level, A_1 passes another highpass filter and lowpass filter to the (j-2) scale wavelets to respectively give D_2 and A_2. Finally, A_2 passes another highpass filter and lowpass filter to the (j-3) scale wavelets to respectively give D_3 and A_3. Thus, D_1 has the highest frequency components because it is the component of the original signal x which has come through a highpass filter. D_2 is the second highest frequency components because A_1, the lower frequency components from x through a lowpass filter, passes a highpass filter. Similarly D_3 is the next highest frequencies. A_3 of the most interest, is the result from three levels of lowpass filters consequently applied to the signal x, so it is the lowest frequencies.

The decompositions go down rapidly based on power of 2 associated with j and k for a signal. This is why wavelet expansions are more effective in signal processing.

iv) There is a connection and equivalence to filter bank theory from digital signal processing (DSP) which leads to a computationally efficient algorithm. For a signal of length of n, the computational complexity of the FFT is $n\log_2(n)$ while that of DWT is n.

Dispersion Calculation

Traditional Spectral Analysis of Surface Waves (*SASW*)

The SASW method calculates dispersion between a pair of channels. It is a pair-channel based method. This method involves evaluation of the Rayleigh wave phase velocity as a function of frequency and the computation of the phase delay associated with the signal travel time at a pair of geophone stations. One pair of signals is assumed to be x_1 and x_2, and then the SASW method for dispersion estimation is shown in Figure 5.9.

This technique is straightforward. However, the success of SASW method depends on the condition that Rayleigh waves predominate in the generated wavefield. The SASW method has a strict requirement for a high signal-to-noise ratio (SNR), which is difficult to meet in urban areas or fields near busy traffic. The other shortcoming is related to phase calculation. The phase delay from cross power spectrum is not genuine phase delay, but wrapped phase. So the phase has to be unwrapped. This unwrapping process might wrongly convert all higher mode phase into one phase curve and result error in time delay calculation. In addition, the geophone spacing has to be long enough to separate the phases of any two neighbouring geophones for unwrapping. This long spacing might cause spatial aliasing to the signal, which results in wrong interpretation of the targets.

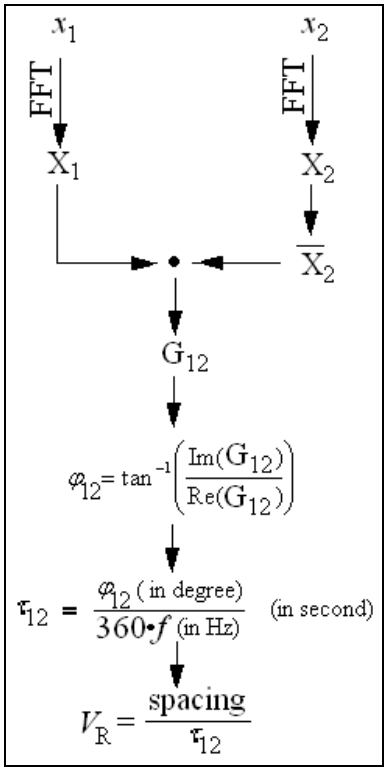

Figure 5.9 SASW method for dispersion estimation: x_1 and x_2 are a pair of signals, X_1 and X_2 are their Fourier coefficients, $\overline{X_2}$ is conjugate of X_2, G_{12} is the cross power spectrum, φ_{12} is phase delay between the two signals, τ_{12} is the time delay between the two signals and V_R is Rayleigh phase velocity between the two stations of these signals.

Multichannel Analysis of Surface Waves (MASW)

MASW method is based on the concept of stacking a set of multichannel seismic data. The fundamental assumption for MASW is that there is no lateral variation and that each layer is homogeneous. Usually a transform technique can be used to map the seismic date into one 2-D field, which is called spectrum and presents energy distributions of different frequency components whose maxima represent predominant energy status of every frequency component. Redundancy from the multichannel data acquisition makes the maxima stand out in the spectrum so the SNR can be significantly improved. As a result,

one 2-D spectrum from transform application to seismic data makes it easy and convenient to pick up dispersion curves. The maximum energy for each frequency is traced to yield the relationship of velocity as function of frequency. This dispersion curve represents the whole seismic section. Besides *f-k* transform previously discussed, frequency-slowness transform (*f-p* transform) and wavefield transform are also commonly applied. These techniques are discussed in detail in Appendix B.

Figure 5.10 (a) gives the flowchart of dispersion calculation of conventional MASW methods, based on which Foti (2000) gave an experimental measurement as an example (b), which reports the composite dispersion curve obtained by the *f-k* analysis of the one shot gather.

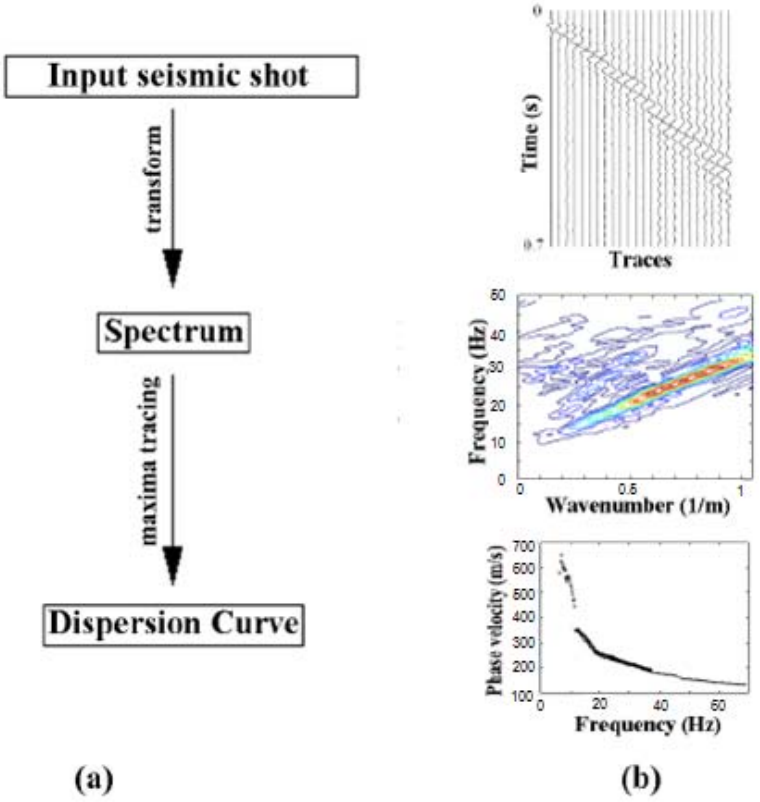

Figure 5.10 MASW method for dispersion estimation using *f-k* transform (Foti 2000)

The Foti (2000) testing site was located close to the Dora Baltea River in Saluggia (VC) in Northern Italy and it is part of a large flat area. Several borehole logs were available, together with results from Standard Penetration Tests and a Cross-Hole Test. The site is composed essentially of fluvial sediments with the soil composed of gravels and gravelly sands, with the presence of fine sand and clayey silt in the form of lenses. Both longitudinal wave velocity and shear wave velocity increase with depth. The data acquisition used a 60 kg weight-drop from 2 m high, at a spacing of 3 m and recorded on 24 channels. The upper panel of Figure 5.10(b) shows a regular dispersion seismic Rayleigh section and the middle panel of (b) shows that globally the frequency range between 8 and 68 Hz. The resulting dispersion curve (the bottom of Figure 5.10b) can be regarded as the effective mean value corresponding to the whole space covered by the array of geophones.

Figure 5.11 shows an attempt to detect a collapse feature and a drainage tunnel conducted by Xia et al (2004) using wavefield transform (Appendix B). The drainage tunnel is at a depth of 13.5 m. For data acquisition, a 24-channel system was used with 4,5 Hz vertical component geophones at 1.2 m spacing and 7.2 m for the nearest field to obtain maximum wavelength of 30 m as well as good spatial resolution. A hammer of 5.5 kg and an aluminum plate of 0.3m×0.3m were used as the seismic source. The seismic section shows many different wave types and seismic events. The spectrum is blurred and the difficulty in separating seismic events results in little confidence for the dispersion curve shown as the white dashed line. The most serious problem is that this dispersion

curve does not represent all this complicated geometrical section covered by the geophone spread.

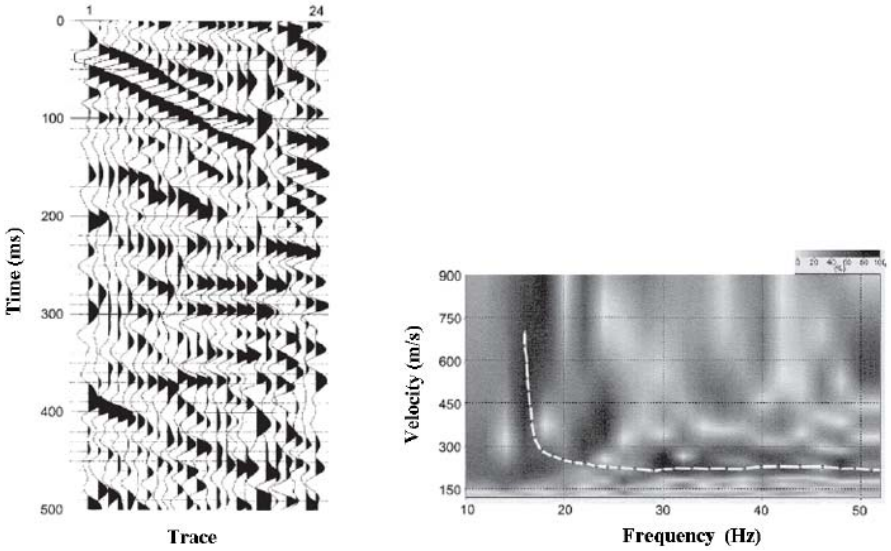

Figure 5.11 MASW methods for dispersion estimation using wavefield transform (KGS Workshop, 2005)

Application of MASW methods using transforms as shown in Figure 5.11 violated the assumption that there were no lateral variations; therefore the dispersion curve cannot be used to well represent a whole section.

Pair-channel Analysis of Continuous Wavelet Transform

Park and Kim (2001) used harmonic wavelets to derive an approach for phase velocity calculation from group velocity. Similarly, it applies to other different wavelets.

The complex Morlet wavelet is given (Schmitz-Hübsch and Schuh 1999):

$$w_{(a,b)}(t) = \frac{e^{-i\omega_0 t}}{\sqrt{2\pi}}\left[e^{-t^2/2a^2} - \sqrt{2}e^{-t^2/2a^2}e^{-a^2{\omega_0}^2/4}\right] \tag{5.10}$$

where ω_0 is the frequency parameter and usually assumed greater than 5 to satisfy the admissibility condition. The corresponding Fourier transform is given:

$$W_{(a,b)}(\omega) = a\left[e^{-(\omega-\omega_0)^2 a^2/2} - e^{-(\omega-\omega_0)^2 a^2/4}\cdot e^{-{\omega_0}^2 a^2/4}\right] \tag{5.11}$$

Given a signal $x(t)$, it has Fourier transform:

$$X(\omega) = \int_{-\infty}^{\infty} x(t)e^{-i\omega t}dt \tag{5.12}$$

From Equation (5.3), the wavelet transform of signal $x(t)$ with the complex Morlet wavelet is computed:

$$\begin{aligned} C_{(a,b)} &= \int_{-\infty}^{\infty} x(t)w_{(a,b)}(t)dt \\ &= \frac{1}{2\pi}\int_{-\infty}^{\infty} X(\omega)W_{(a,b)}(\omega)d\omega \\ &= \frac{1}{2\pi}\int_{-\infty}^{\infty} X(\omega)W(a\omega)e^{i\omega b}d\omega \\ &= \mathrm{FT}^{-1}\{X(\omega)W(a\omega)\} \end{aligned} \tag{5.13}$$

Then the coefficients $C_{(a,\,b)}$ are finally computed efficiently using Fast Fourier Transform (FFT) by first computing $X(\omega)$ and $W(a\omega)$, and then computing inverse Fourier Transform of the product of $X(\omega)W(a\omega)$.

After decomposition of the seismic signal basis on the complex Morlet wavelet, the wavelet coefficients can be represented as the decomposed signal by Equation (5.14) (Chik et al. 2009):

$$C(a,b) = y(t)e^{i\theta(t)} \tag{5.14}$$

where $y(t)$ represents the envelope of $C_{(a,b)}$and θ is the phase of $C_{(a,b)}$.

$$\begin{aligned} &y(t)\cos\theta(t) + jy(t)\sin\theta(t) = y(t)\cos\theta(t) \\ &p(t) + jH(y(t)\cos\theta(t)) = p(t) + jH(p(t)) \end{aligned} \tag{5.15}$$

where

$$p(t) = y(t)\cos(\theta(t)) \tag{5.16}$$

And H is called the Hilbert transform; the magnitude $m(a,b)$ and $C(a,b)$the phase $\theta(a,b)$ of $C_{(a,b)}$ are given:

$$\begin{cases} m(a,b) = \sqrt{[p(t)]^2 + \{H[p(t)]\}^2} \\ \theta(a,b) = \tan^{-1}\left(\dfrac{H[p(t)]}{p(t)}\right) \end{cases} \tag{5.17}$$

In Matlab Wavelet Toolbox, the function “COEFS = cwt(S,SCALES,'cmor')” computes the continuous wavelet coefficients. The magnitude and phase can be computed using Equation (5.17).

Then, how are the magnitude and phase used to derive the corresponding information of the signals recorded in seismic data? Continuous wavelet transform is fundamentally a correlation method. The wavelet coefficients $C_{(a,b)}$ provide information about the

structure of the input signal, $x(t)$ and its relationship to the wavelets $w(t)$. If the wavelets are selected suitably, then $x_f(t)$ include most information of interest of original $x(t)$. That is, $C_{(a,b)}$ sufficiently and correctly provide information about the structure of the input signal $x(t)$.

If the signal recorded at a geophone is denoted $x(t) = y(t_g)\cos(\theta(t_p))$ based on Equation (5.15), where t_g is the group delay and t_p is the phase delay. The group delay can be measured through magnitude of $C_{(a,b)}$ and then the phase θ corresponding to t_g can be traced through the phase of $C_{(a,b)}$. Then, the phase delay t_p can be traced using θ through the phase of $C_{(a,b)}$. The difference in phase time delay between signals from a pair of channels is finally used for phase velocity calculation. Figure 5.12 gives the process of dispersion curve calculation.

To explain this flowchart in Figure (5.12), one example in Figure 5.13 is presented to illustrate how the processing works. This is done using the programs coded in Matlab by the author.

i) A pair of signals was read from seismic data (a1 and a2). The two signals are channels 5 and 6 from shot line 1 in forward direction from the Stellarton Coalfield site.

ii) The magnitudes of their wavelet coefficients resulting from continuous wavelet transform were mapped (b1 and b2).

iii) Then tracing maximum for every frequency component in b1 and b2 produced the group time delays, respectively denoted as t_{g1} and t_{g2}, based on which

phase θ would be read off in the phase delay curves also resulting from CWT (c1 and c2).

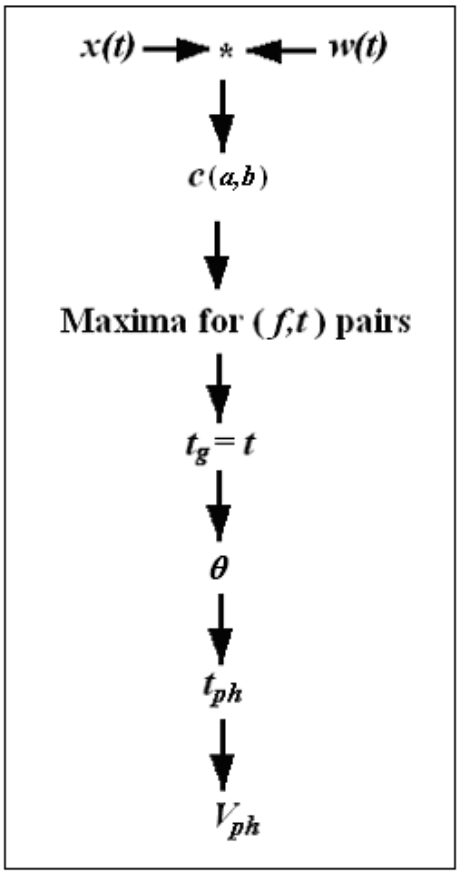

Figure 5.12 Pair-channel dispersion curve estimation using CWT methods

It is apparent θ would right couple t_{g1} in c1, which is the corresponding phase time delay t_{p1}, whereas the phase θ would not right couple t_{g2} in c2, but correspond to time values, t_L before t_{g2} and t_R after t_{g2}, which is closer to t_{g2} is the phase time delay t_{p2} in c2.

If phase time t_L closer to group time t_{g2}, or the carrier travels faster than the envelope, the small scale section between the two geophones is normally vertically layered medium. If phase time t_L equals group time t_{g2}, or the carrier travels at the same velocity as the envelope, the small scale section is homogenous and isotropic. If phase time t_R closer to group time t_{g2}, or the carrier travels slower than the envelope, the small scale section between the two geophones is inversely vertically layered medium (Section 2.5).

It is noted that, corresponding to the all the frequencies, t_{p1} and t_{p2} are two vectors of the same size as the frequency range.

iv) Finally, phase velocity could be calculated by dividing distance between two geophones by the difference of phase time delays t_{p2} and t_{p1}. The plot of the phase velocity vector over frequency vector is the dispersion curve (d).

There are a number of different types of wavelets. Trial and error concludes that the Complex Morlet Wavelet is most suitable for variation localization. The comprehensive comparison made is shown in Appendix C.

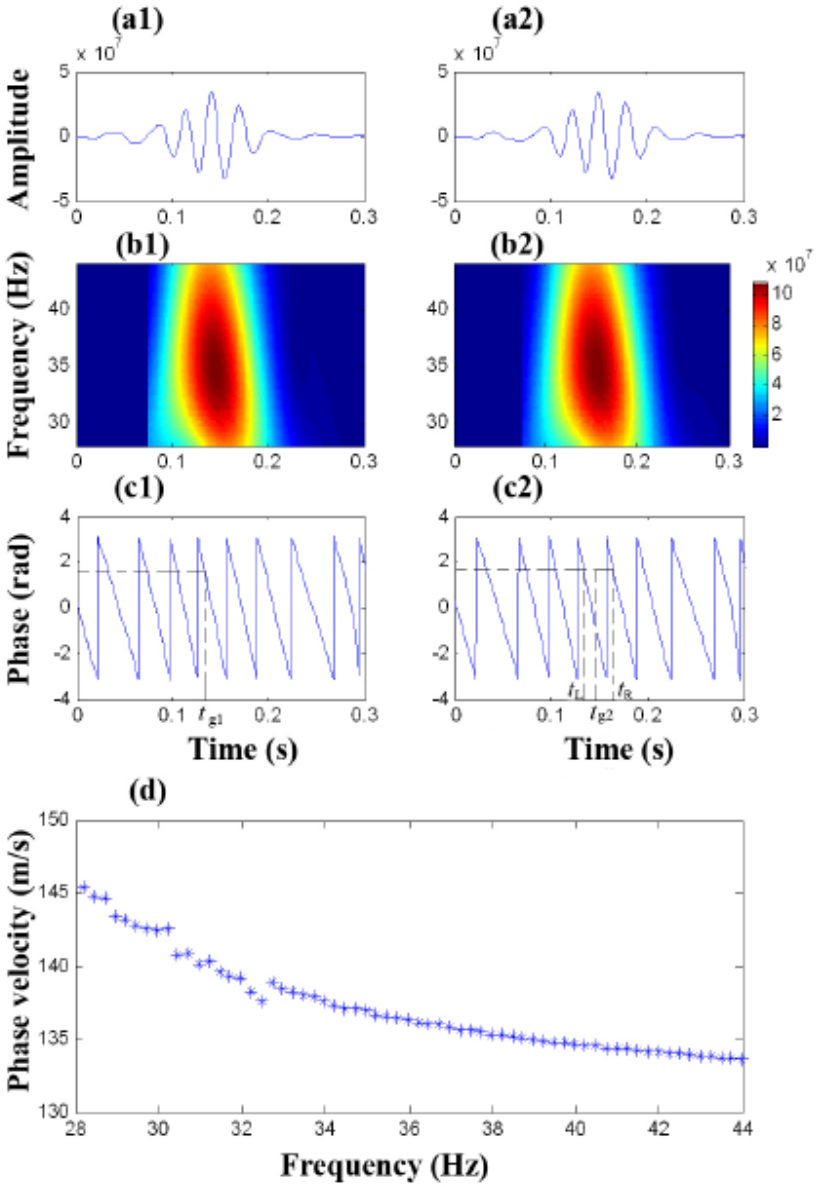

Figure 5.13 Pair-channel dispersion curve estimation using CWT methods: (a1) and (a2), a pair of traces; (b1) and (b2), CWT mappings; (c1) and (c2), wrapped phases; (d), dispersion curve. (Xu et al 2008)

Shear Velocity Field Mapping

Shear velocity field (SVF) mapping is essentially shear velocity contouring. Along the geophone spread, shear velocity is plotted as a function of depth to give a 2-D shear velocity section, which can be used to differentiate variations and anomalies.

Surface wave propagation depends on frequency (depth of penetration), phase velocities (compression and shear), and the subsurface density. Each of these properties will affect the surface wave dispersion curve. However, a dispersion curve can be inverted to obtain a shear wave velocity profile as a function of depth since shear velocity has the greatest impact on the properties of a surface wave as discussed previously.

The determination of shear velocity as a function of depth from experimental Rayleigh wave dispersion is usually referred to as inversion. There are two categories of inversion techniques which were grouped into optimization methods and numerical modeling methods. In the optimization inversion process, it is assumed that know the depth of each individual layer of the target is known, while in numerical modeling inversion process, besides the depth for each layer, it is necessary to have prior knowledge of the P-wave velocity, Poisson's ratio and density of each individual layer. However, for purpose of detection and localization of anomalies, there may not be a suitable layered model which can be used for reference; in addition, Rayleigh wave propagation becomes so complex that there is not any mathematical formulation at all. For the complicated fields encountered in this research, it would be difficult to build up accurate mathematical models and define suitable boundary conditions for forward simulations or inversion

problems. At best, it is a long way to go and a lot of work to do. This topic is beyond this research but is under study in related research investigation.

To simplify the inversion procedure, the Steady State Rayleigh Method was used. It is the first method developed for soil characterization at a small scale proposed by Jones (1958, 1962) and then adopted at the Waterways Experimental Station, USA (Ballard 1964). Butt et al (2005) also applied this strategy in cavity detection at Montague Gold District, NS, Canada. Starting with the obtained dispersion curves for Rayleigh waves, approximate procedures based on the results of theoretical analysis of wave propagation were used to infer shear velocity of the subsurface system. Rayleigh wave wavelength λ_R can be easily calculated for all frequencies f by:

$$\lambda_R = \frac{V_R}{f} \tag{5.17}$$

where V_R = Rayleigh phase velocity

The motion induced by surface waves is confined in the upper part of the media. Thus it can be assumed that the energy that is associated to the perturbation travels in shallow zone. The depth penetration z is associated with wavelength (Section 2.4) approximated by

$$z \approx \frac{1}{3}\lambda_R \tag{5.18}$$

The shear wave velocity V_S is closely related to V_R (Section 2.4) and can be estimated as:

$$V_S = 1.1 V_R \tag{5.19}$$

This process can be considered to be direct mapping from the (V_R, λ_R) space to the (V_S, z) space and yield a stiffness profile (Figure 5.14). This simple inversion procedure is based on the limited availability of more precise inversion methodologies for imaging complicated targets. Although this result might not present the exact depth of individual layers and anomalies, it definitely gives a good approximation and can be referred to as a guide for further subsurface investigation.

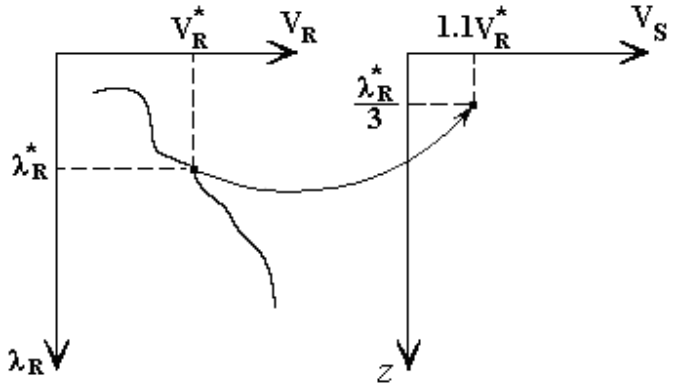

Figure 5.14 Simplified inversion process: mapping (V_R, λ_R) space to the (V_S, z) space will yield one stiffness profile

Demonstration of SVF Mapping

Dispersion calculation is the key part of the whole research. Dispersion calculation and SVF mapping involve a large amount of data and complicated calculations which have to be done by fast computers.

Figure 5.15 used the same field data as Figure 5.13 to show the process of the dispersion and SVF mapping. When the input data was chosen, the *f-k* spectrum was generated and

the predominant frequency range was selected by mouse clicks at two reasonable cross cursor locations (a). The frequency range allowed a suitable scale vector for wavelet transform. Next, a seismic record appeared with upper velocity limit on it (b). This limit would suppress effects of other potential events which could not be completely removed by the filtering process. However, an opportunity was given to override the velocity for imaging purpose when an input dialogue box popped up (c), where a number close to the upper velocity could be specified. The default value would be the reading in (b), that is, if nothing was input, the original reading (b) would be accepted. Following that, all wavelet transform and pair-channel analysis would be done. All dispersions curves would be saved in a matrix combined with frequency vector and geophone station vector. Because there are so many dispersion curves that it is not of straightforward meaning to display all them, only a final SVF image would be presented (d).

If topography information is considered in the processing, the SVF image would have a surface following the elevations. But for all testing fields in this research, the surface does not change very much and the surface variation was negligible, so topography information was not taken into account. However, there is an option for topography consideration in this program, which can be applied to future research.

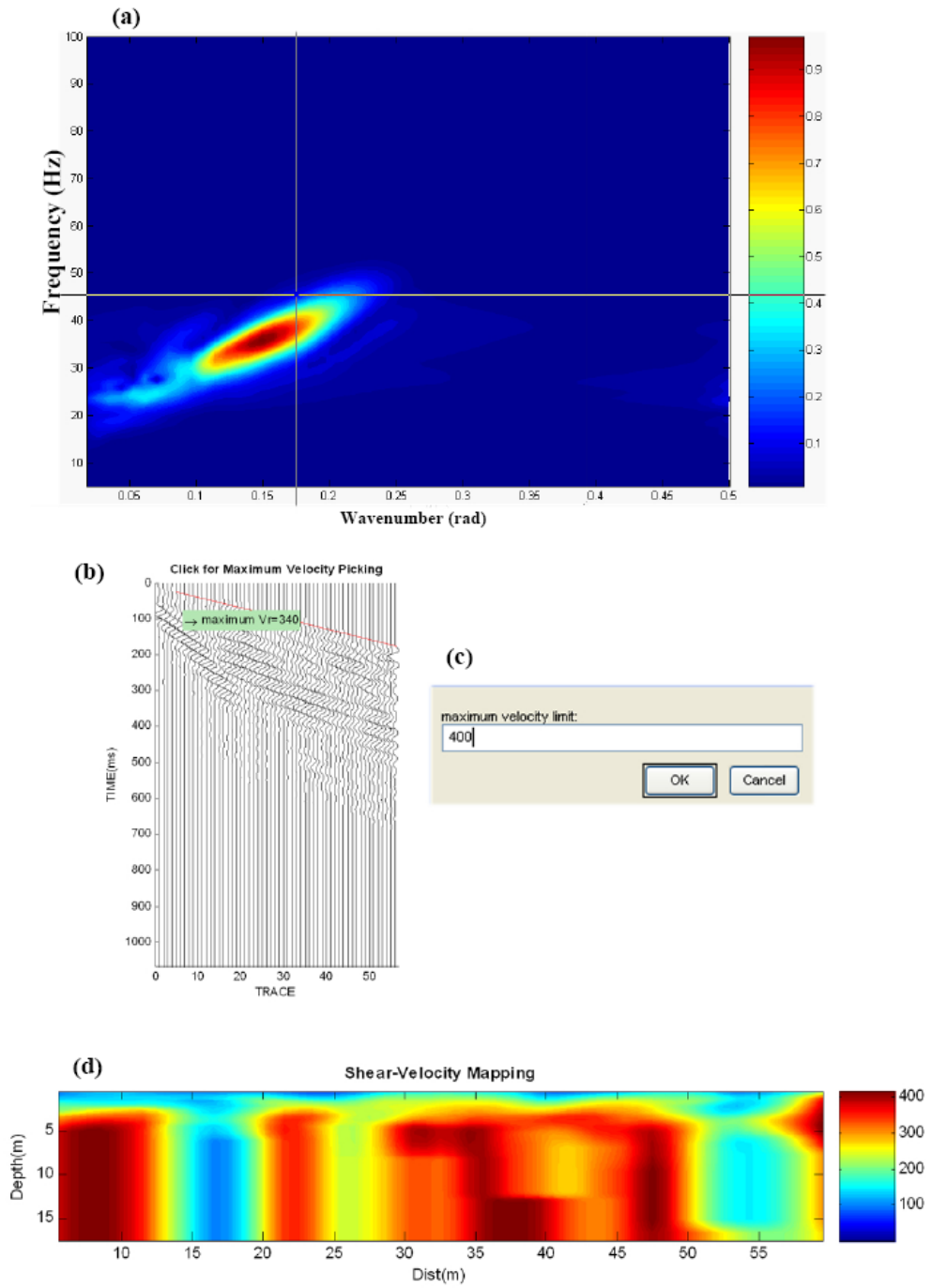

Figure 5.15 Demonstration of dispersion and SVF mapping (Stellarton Coalfield site, summer 2006). (a) *f-k* domain for determination of frequency range, (b) x-t domain for determination of maximum Rayleigh wave velocity, (c) input box of maximum velocity, (d) SVF image

CHAPTER 6: FIELD TESTS

This chapter covers three field tests in different subsurface scenarios: (i) medium dipping coal seams in Stellarton coalfield, (ii) steeply dipping gold-bearing quartz veins in West Waverley Gold District, and (iii) nearly horizontal strata in Liverpool. All these sites are in the province of Nova Scotia, Canada. As shown in Figure 6.1.

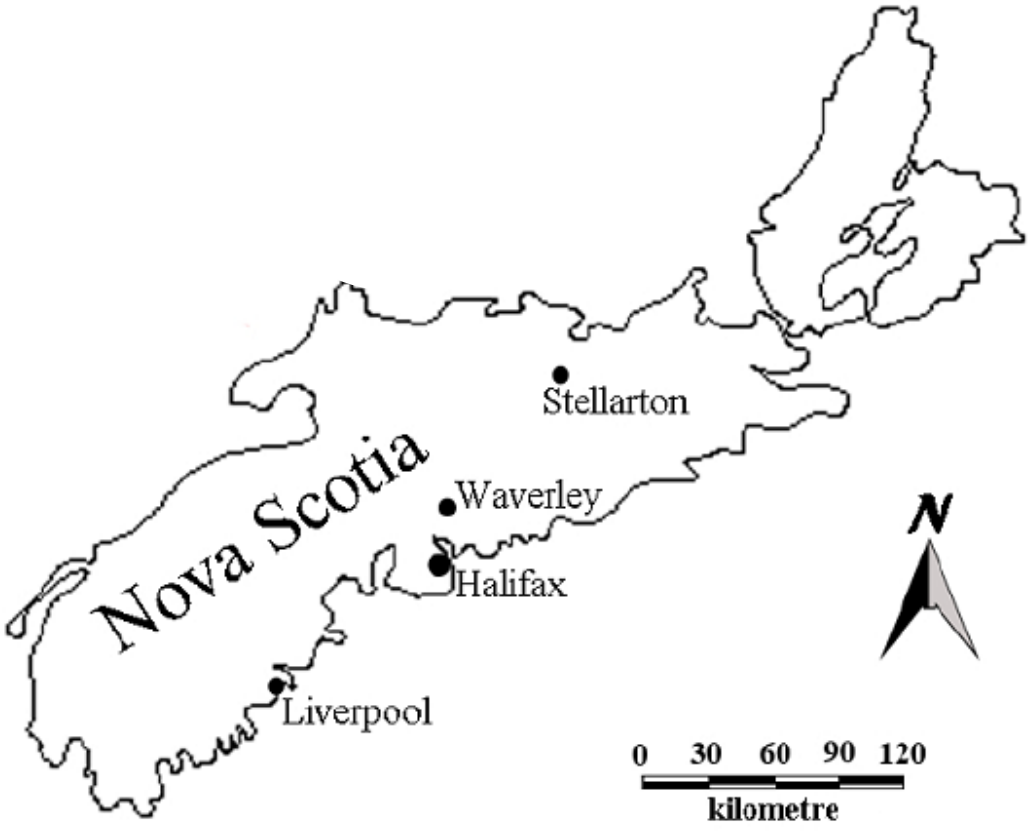

Figure 6.1 Locations of testing fields

The Stellarton site is now an open pit for coal mining. The shallow coal seams were historically mined using a room and pillar geometry with approximately 50% extraction ratio. Seismic investigation can be easily checked by field observations. The Waverley site is a crown-shaped area characterized by two boundary faults, a centrally twisted anticline and steeply dipping geological formations with several gold bearing quartz veins. This district was extensively mined during "Gold Rush" times from 1860s to 1930s. The purpose of the field test in Waverley was to evaluate the accuracy and confidence of the seismic surface method introduced in this research when it was applied very complicated geological and disturbed conditions. The third site, in Liverpool was a geotechnical site where foundations of condominiums are going to be constructed. Investigation of this site would be compared with borehole logs. Furthermore, the success of this investigation would prove potential applications to geotechnical site investigations.

Experimental Setup and Experimental Methodology

The seismic system consisted of Seistronix RAS-24 seismograph, a laptop computer, a 60-metre-long geophone string with 12 GS-11D geophones, and a 12lb sledge hammer source with a 60-metre-long source cable.

The RAS-24 is a commercial seismograph designed for shallow refraction and reflection surveys, and general geophysical exploration. The RAS-24 seismograph utilizes 24-bit analog to digital conversion, automated signal enhancement, and records seismic data files in SEG-2 format.

The GS-11D geophone is made in the Geospace Technologies. This geophone has a natural undamped frequency of 4.5 Hz and, a DC resistance of 380 Ohms and an intrinsic sensitivity of 0.810 V/IN/SEC. Figure 6.2 gives the response curve for the GS-11D.

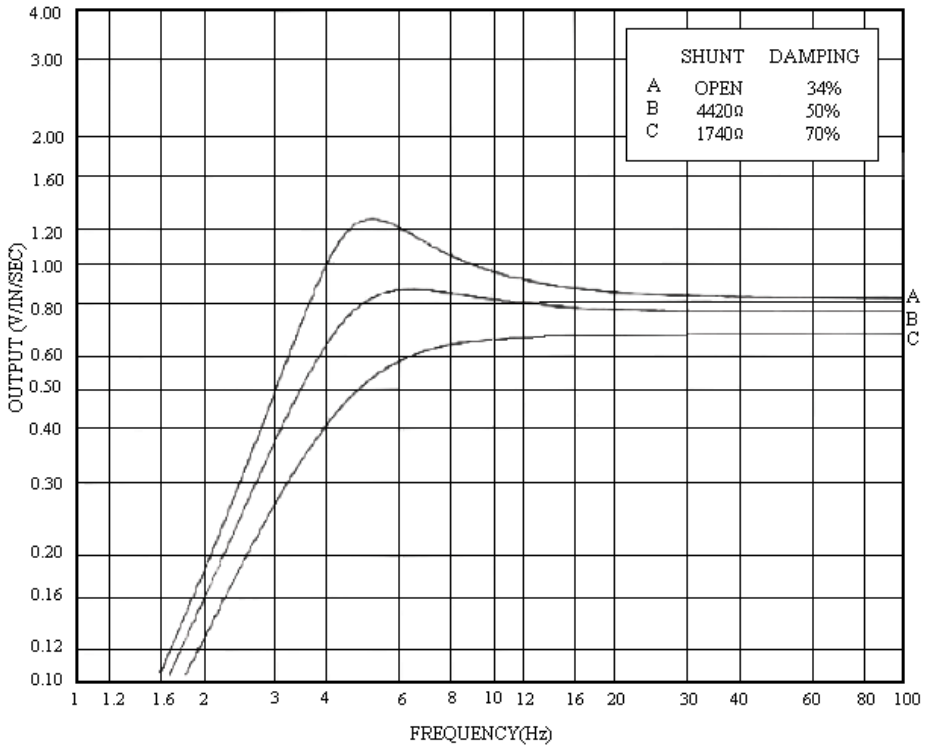

Figure 6.2 Response curve for GS-11D geophone

At the outset of this investigation, several types of portable sources were fabricated and evaluated, including a modified 22-caliber-gun, a 12 lb sledgehammer, and a custom-built 12 kg weight drop impacting on a metal plate (Butt et al. 2005). The hammer blows were proven to be highly repeatable (Figure 6.3) and allowed the source to be moved easily, by the use of the source cable, to either end of a survey line with a geophone

spread setup, which are referred to as forward shot and reverse shot (Xu 2004, Butt et al., 2005).For these reasons, most seismic data presented in this chapter are recorded using the sledgehammer source.

Figure 6.3 is an example of the routine procedure for source evaluation. The sledgehammer source is evaluated by seismic sections from different shots and the same individual traces from different shots, spectra sections from different shots and the individual spectrum of the same traces from different shots, and the frequency-wavenumber images from different shots for comparison with one another.

Another approach for source evaluation is computing coherence function between two shots (Xu 2004). This approach is applied the same way as used in SASW method (Foti 2000), but the coherence function is computed between the same traces of two shots, rather than two traces of one shot.

In order to use the 12 geophones and 60-metre-long geophone cable to acquire seismic data from a long survey line with short trace spacing, a method of shifting geophone spread is developed (Xu et al. 2008). This method has the following properties:

i) The shift numbers depends on the survey length. 3 to 5 shifts are used to complete data acquisition for a survey line which has a length ranging from 30 to 56 metres.

ii) Geophone spacing depends on the survey line. In the field, 3 to 5 metres is used for a line ranging from 30 to 60 metres long.

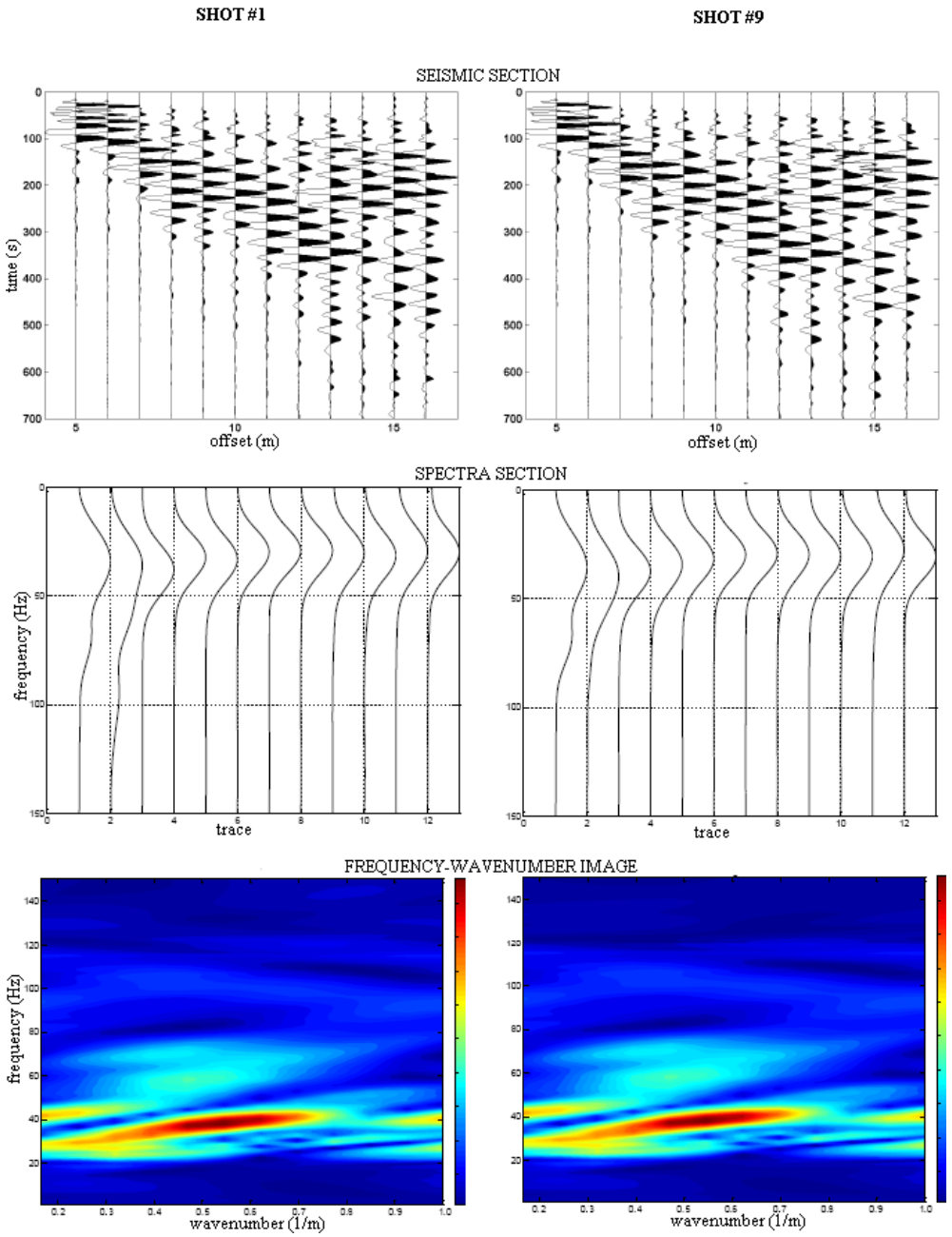

Figure 6.3 Comparison of two shots by sledgehammer: left column is for shot #1 and right is for shot #10; upper panel is seismic sections, middle panel spectra, and bottom *f-k* display (Stellarton data, line #1 position 1 forward shot)

iii) Typically stations are surveyed at 1 metre spacing and the first station is referred to as Station 0, which is used for the source location for the forward shot direction.

iv) The source is kept at the same location, usually at the 0^{th} station.

v) The first geophone is kept at the same location, usually at the 5^{th} station.

vi) The second geophone starts at the 6^{th} station, which 1 m from the first geophone. This geophone is moved 1 meter further for each shift.

vii) After data acquisition from the first set of shift, the other 11 geophones are moved 1 meter away from source, and so on. The shifting geophone spreads are referred to as positions.

viii) The data acquired from all the positions are combined to yield a survey line data of 1 metre spacing.

The same shifting is used for reverse shots. The next sections provide more details of how to apply this method.

Stellarton Coalfield

Field Introduction

The Stellarton Basin or Pictou Coalfield, with a size of only 18 km east-west and 6 km north-south, is situated in the north-central part of Nova Scotia. There are fifteen major

coal seams in the basin ranging from 1 to 14 m in thickness; twelve have been mined in the past. One of these, the Foord seam, at 13.4 m, is the thickest coal seam of Carboniferous age in North America. Mining has taken place in this field over the past 170 years, and relative to its small size, it has been one of the most extensively exploited and the most productive coalfields in Canada. The earliest workings in the Pictou coalfield were accessed by a series of shafts on the Foord Seam and coal was hoisted by horse gins. Many old shafts are open, and deep, and these shafts and tunnels are in varying stages of instability. Also old mining pits, trenches and quarries are considered dangerous because of loose rocks, and water seepage which indicates uncertain depths (Calder et al, 1993).

Currently, large-scale surface mines operate in the Stellarton Basin for the near surface coal resources, the great thickness and number of coal seams. The coal seams have a strike almost East West, dipping at 26° toward the North. Pioneer Coal Ltd. began mining coal in Stellarton from the Foord seam in 1996 and from the Cage Seam in 2001 for 2.6 million tonnes of coal. The mineable Foord Seam is approximately 12 metres thick and the Cage Seam approximately 5 metres thick. The company expanded eastward in winter 2004 for another 1.1 million tonnes from four seams: Cage, Third, McGregor and New seam. The company has approval to surface mine 3.7 million tonnes from five coal seams at Stellarton site. Heavy mechanical equipment is used to break the coal and overlying rock and the material is excavated using hydraulic excavators, conveyors and off-road haul trucks.

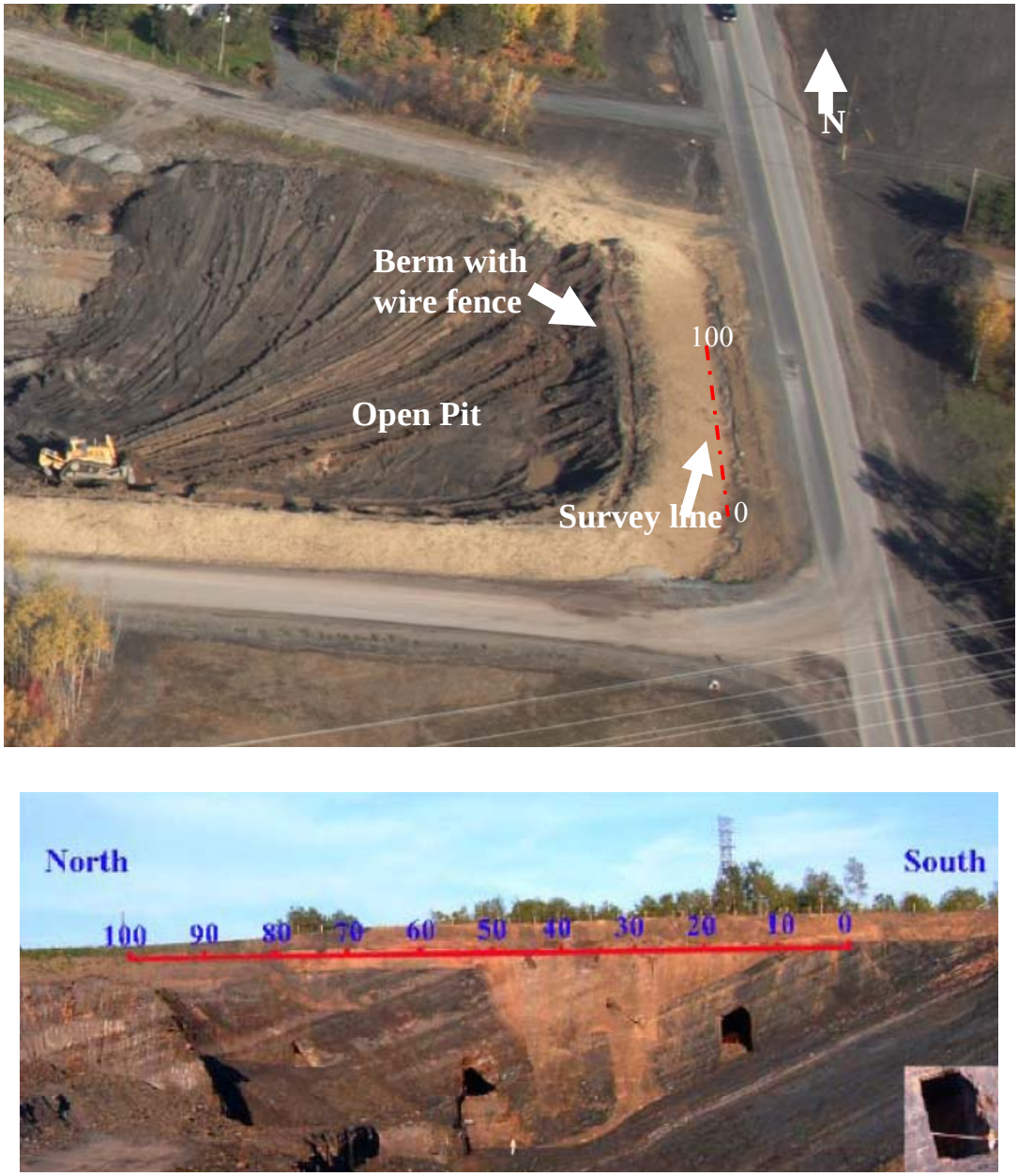

Figure 6.4 Surveying site: the upper shows the survey line parallel with the pit wall and McGregor Road (The North South highway); the bottom is a pit wall photo showing 4 tunnels discovered in mining progress.

Development and mining in Stellarton uncovered many inclined shafts and tunnels. The east boundary wall of the pit (Figure 6.4) from Stellarton pit shows a typical old mine distribution. Generally, the old tunnels are approximately separated by 5 to 10 metres and

went approximately along the coal seam strike direction (Arden Thompson, former Geologist in Pioneer Coal Ltd, personal comments.).

A survey line at the toe, outside the berm (the east boundary), was selected for seismic data acquisition (Figure 6.4). This line is in a ditch, whose surface is loose and wet, located about 20 m east of the edge of the open pit on the outside of the berm. The loose surface was removed at the planned stations using a spade to ensure good ground coupling. The line was designed 100 m long to fully cover the four discovered tunnels.

Data Acquisition

The survey was carried out on a sunny weekend to avoid noise from mining operation and busy traffic of McGregor Road.

To cover the planned 100-metre-long line, stations were set at each metre from 0 to 100 metre (stations), and the 100-metre-long line was broken into two segments: the first segment from 0 to 60th station where source was set at station 0, and the second segment from 40th station to 100th station where source was set at station 40.

For each segment, 5 geophone layouts were used to form a 56-channel record. The first geophone was kept at same position. In layout #1, the second geophone was 1 m from the first geophone and all the other geophones were placed 5 m apart (Figure 5.5a)) For each subsequent layout, all geophones were moved by 1 m. The superposition of the 5 layouts would form a 56-channel array for seismic data record with 1 metre spacing from 5th station to 60th station (Figure 6.5b).

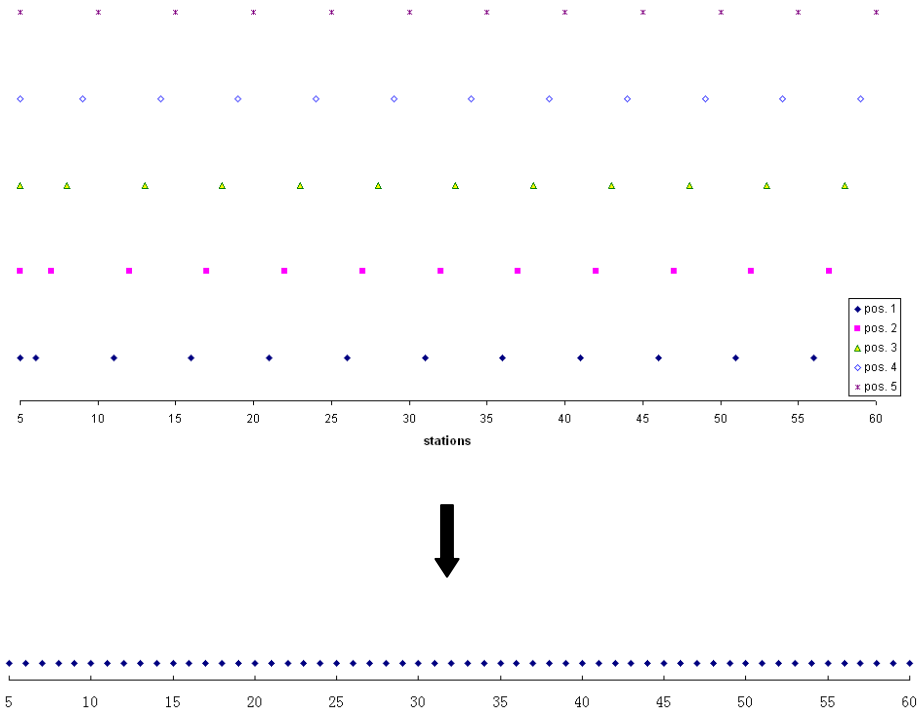

Figure 6.5 A 56-channel array resulting from superposition of 5 geophone positions: top figure is the five layouts and the bottom one the superposition.

The same arrangement for the second segment was used to form another 56 channel array from 45th station to 100th station. Two shot directions, forward and reverse, were applied for averaging to minimize uncertainty and investigate updip and downdip shot directions. For reverse shots, the two reverse segments were respectively from 100th to 45th station and 60th to 5th station. Different geophone positions and corresponding superposition were also used as forward shots.

Sampling frequency was set at 500 Hz, and recording length was 1.6 second. For each position, 10 shots were applied for stacking. The first channel was used for making a visual judgment for stacking or discarding a shot.

Data Processing

Prior to processing, it was considered that for Stellarton seismic data, the tunnels and the dipping layers should cause dramatic changes in the Rayleigh wave propagation and conversion of wave types. The open pit boundary should produce side scattering energy. The raw field records of Stellarton are shown in Figure 6.6. All these four figures are 56-channel traces from the superposition of 5 stacked shot gathers of geophone positions of two different segments in two directions. Taking segment 1 (a) for example, red 'A' is direct P-waves (in red line), and 'B' is backscattering events screened with green ellipse, and 'R' is Rayleigh waves encompassed by light yellow lines fanning out and varying apparently with offset due to layered medium giving rise to strong dispersive phenomenon and tunnels and collapses resulting in propagation velocity changing with offset. In addition, there must be some side scattering energy not differentiable. As a result, Rayleigh waves might not be easy to differentiate in the raw field record because of interference of different wave types.

Although Rayleigh waves appear to be predominant here, they were not very clear, probably because the signal to noise ratio was not sufficiently good. Their counterparts in frequency wavenumber domain, or *f-k* domain, are displayed in Figure 6.7.

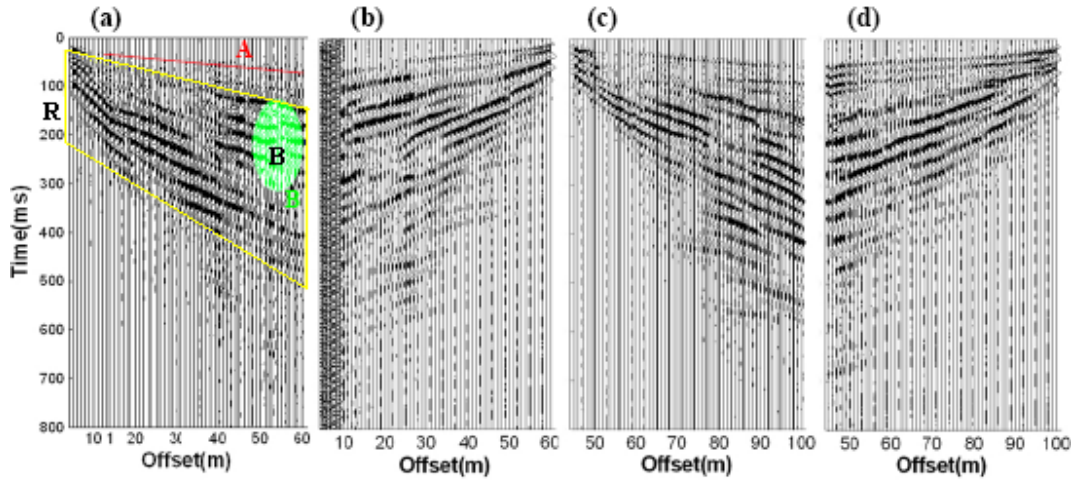

Figure 6.6 Seismic records from Stellarton field: (a) segment #1 forward stacked data, (b) segment #1 reverse stacked shots, (c) segment #2 forward stacked shots, (d) segment #2 reverse stacked data. The far field in (b) was full of noise because of the 12th channel malfunction.

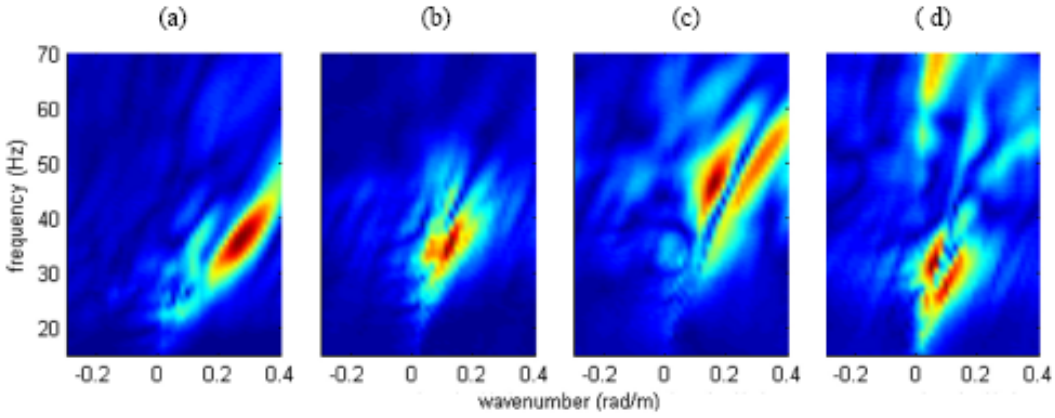

Figure 6.7 *f-k* spectra corresponding to Figure 6.4

Generally, most energy is concentrated in a small frequency range for all these records. On the other hand, each frequency component covers a range of wavenumber resulting in flat shape images in *f-k* domain. This indicates interference of different wave types or

wave modes existed. It was also noticed that the first segment was in a relatively intact shape and in a frequency range of 20 and 50 Hz, while the second segment was more spread out indicating a higher mode of Rayleigh waves.

After initial examination of the raw field data in time-space domain and frequency-wavenumber domain, the processing strategy for individual waveform pre-processing and MASW waveform analysis was composed of two main stages. The first dealt with data processing methods that emphasized the direct Rayleigh Waves in each record. The second dealt with wavelet transform technique for dispersion curve estimation, which derived wave velocities vs. depth along the seismic lines, or shear velocity field imaging (SVF).

The first pre-processing step was the removal of noise or isolation of Rayleigh waves from the dataset. It consists of some operating filters in both space - time (*x*-*t*) domain and frequency-wavenumber (*f*-*k*) domain. The preprocessing includes windowing the Rayleigh wave, muting noise in *x*-*t* domain, windowing the Rayleigh wave in *f*-*k* domain, or *f*-*k* filtering, and lowpass filter. This processing would significantly enhance Rayleigh waves. The results from the pre-processing were shown in Figure 6.8 corresponding to Figures 6.6 and 6.7.

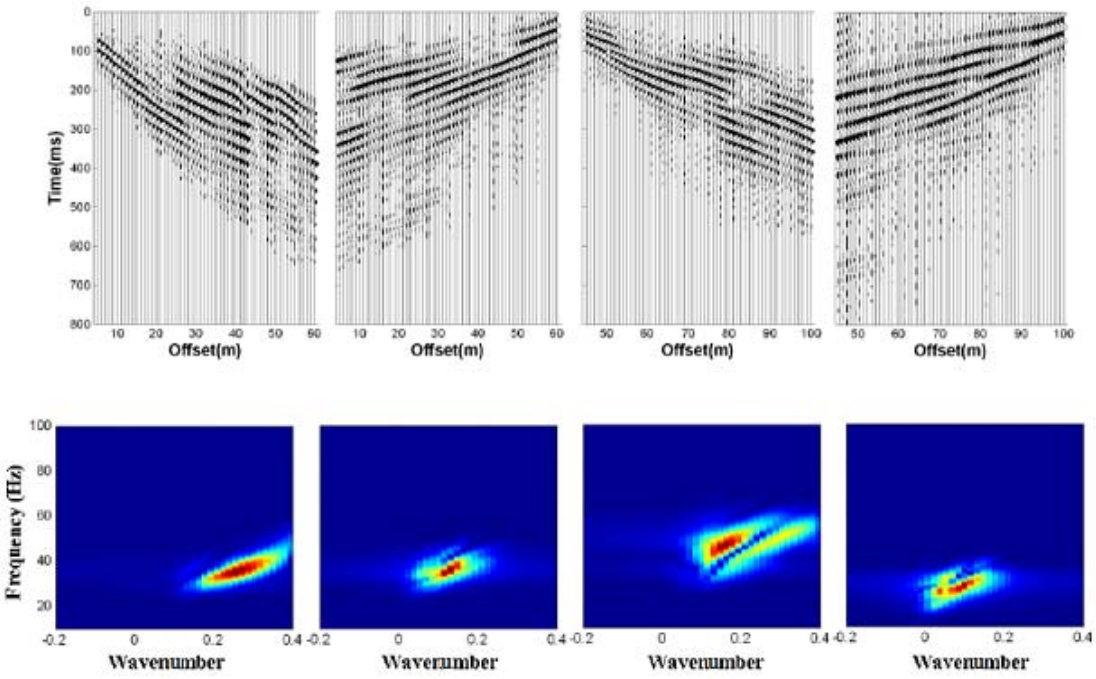

Figure 6.8 Counterparts of Figures 6.6 and 6.7 after preprocessing (same range 0-70Hz as in Fig 6.5)

The next step is dispersion estimation using continuous wavelet transforms, and then the shear velocity field (SVF) is obtained using an assumed penetration depth to wavelength ratio of one third and an estimated Rayleigh wave velocity of 91 to 96 % of the shear wave velocity. To minimize uncertainty, the average of forward SVF and backward SVF of a segment is the final SVF image for this segment. Finally, two SVF images are obtained for the two segments of the 100-metre survey line. The SVF images are shown in Figure 6.7b in comparison with the geological section (a) for interpretation.

Interpretation

When we examine Figure 6.9 and compare the SVF images with the geological section of this site, four low velocity zones can be identified respectively at 10 to 20 metre, 36 to 42

metre, 61 to 66 metre, and at the far end. The first 3 zones matched the geological section. The last one was not seen in the section (Figure 6.9a) because the overburden had not been removed. In addition, the weaker zone at around 30 m also well represents the collapse at the same location of geological section.

Refraction processing was also applied to the Stellarton data. Reverse refraction profiles were picked up in Figure 6.10a, b, a' and b'. Then the plus-minus technique was applied (c and c') to determine the bedrock profile (d and d').

Refraction image only gave very rough picture of this bedrock, and did not well match SVF in these tunnel locations. Two reasons are proposed for this mismatch: the first reason was that the bedrock was not intact, but remarkably disturbed by extensive mining activities through tunnelling and subsequent sag or collapse; the other reason was that we did not exclusively acquire refraction data. The principal purpose of Stellarton field trial was Rayleigh wave acquisition. As expected, all seismic data were predominant in Rayleigh waves. As a result, the refraction was so weak that it was difficult to pick up. Processing has been done to mask Rayleigh waves to enhance refraction, but it did not work well. The plus-minus technique apparently gave some wrong results because the final forward time elapse, T_f reading at rightmost, and final reverse time elapse, T_r reading at leftmost, did not equal each other.

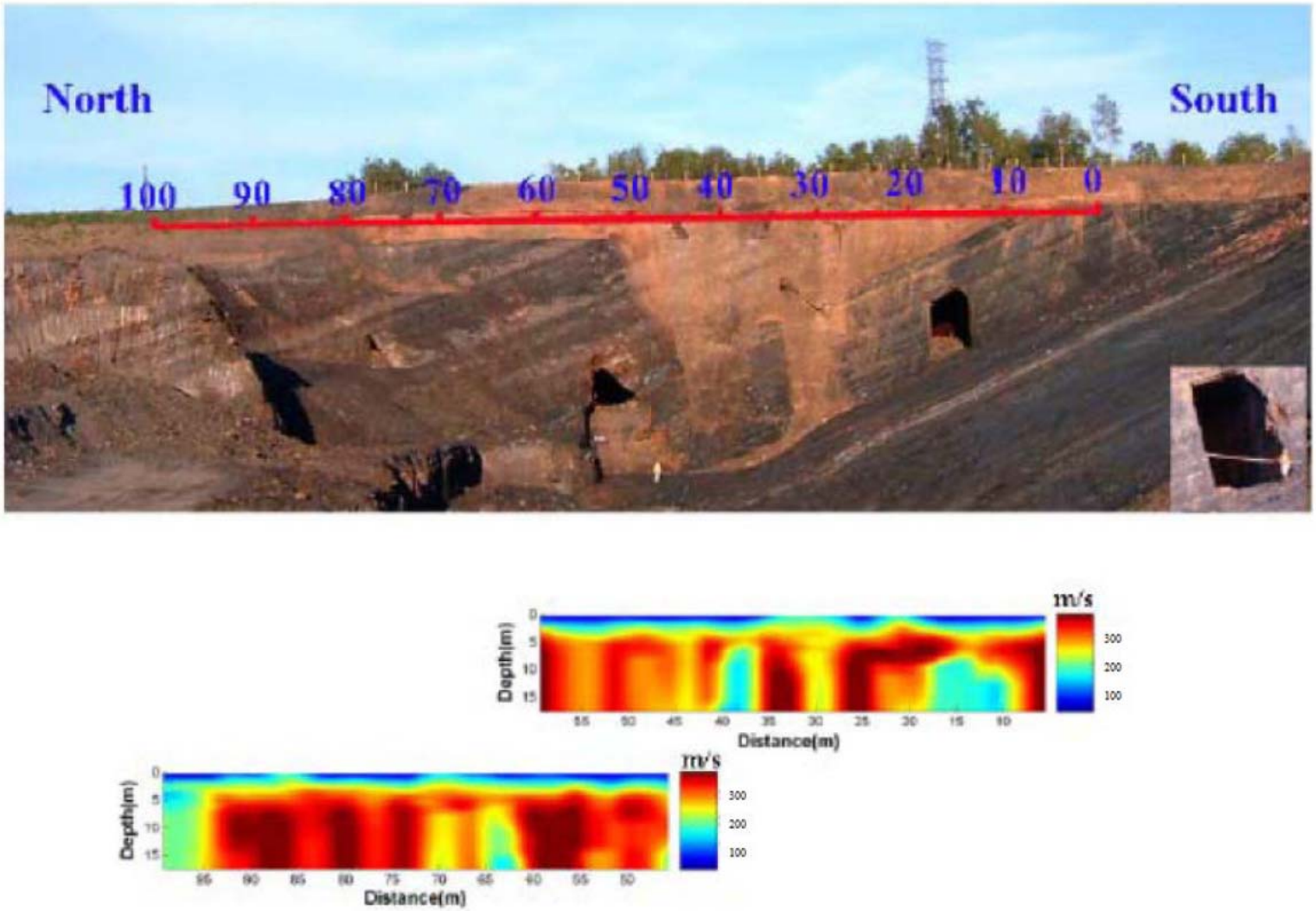

Figure 6.9 The geological section of imaging targets (a) and SVF image (b): the right bottom in (a) is the photo of me measuring the size of the tunnel in south end. The width was 5.7 m

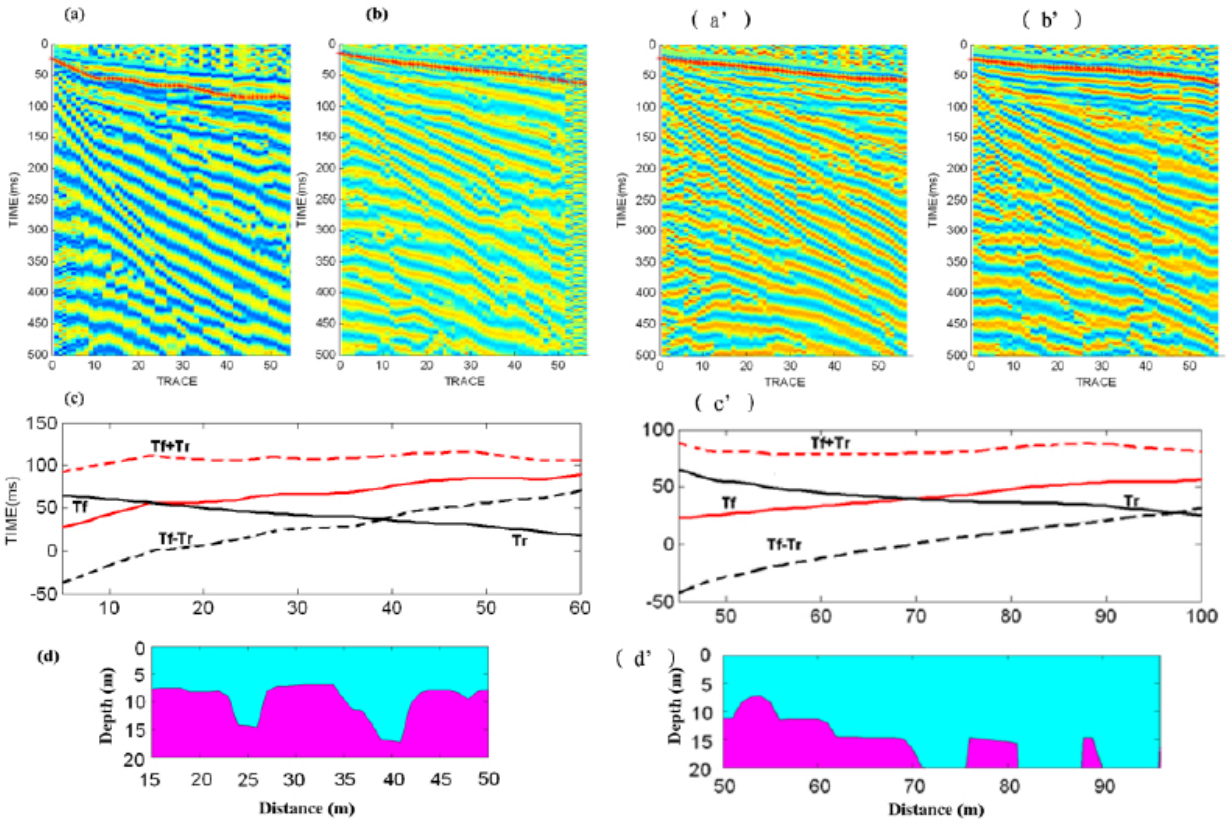

Figure 6.10 Refraction bedrock imaging: the left column (from a to d) was from the first segment data and the right column (from a' to d') was the second segment data. T_f = forward time elapse, T_r= reverse time elapse

Waverley Gold District

Field Introduction

The Waverley Gold District is about 20 km north of Halifax. Two chains of lakes transverse the district from north to south. These lakes lie on the course of two nearly parallel faults about 1700 m apart, and offer a fine illustration of the dependence of geographical outline on geological structure. The district is divided into two portions,

called East and West Waverley. East Waverley lies to the east of the chain of lakes and West Waverley lies to the west. West Waverley was the focus for this field trail.

Figure 6.11 is a sketch of plan view (a) and a cross-section (b) of West Waverley. In addition to the two parallel faults, this district is geographically characterized by a major anticline, whose axis is slightly tilted and is nearly perpendicular to the two faults. The outcrop of veins is that of a series of concentric semi-ellipses, much flattened or compressed at the sides, and with a northerly bend at its western extremity. The present geographical and geological characteristics of this area were caused by several movements. These movements may be summarized as follows (Hind 1869):

1st. The great East and West overturn anticline.

2nd. The low north and south cross anticline which produced a fracture in the strata 1700 m from one wall to another, as well as

3rd. An upthrow of 200 m on the east side, with a thrust to the north of 170 m, and on the west side an upthrow of 260 m, and a thrust to the south of 60m.

4th. One squeeze of the strata between the walls of the break to the extent of 120 m, by lateral pressure, probably from west to east, and causing—

5th. An upthrow of the crown of the arch, resulting from the lateral pressure, to the extent of 500 m.

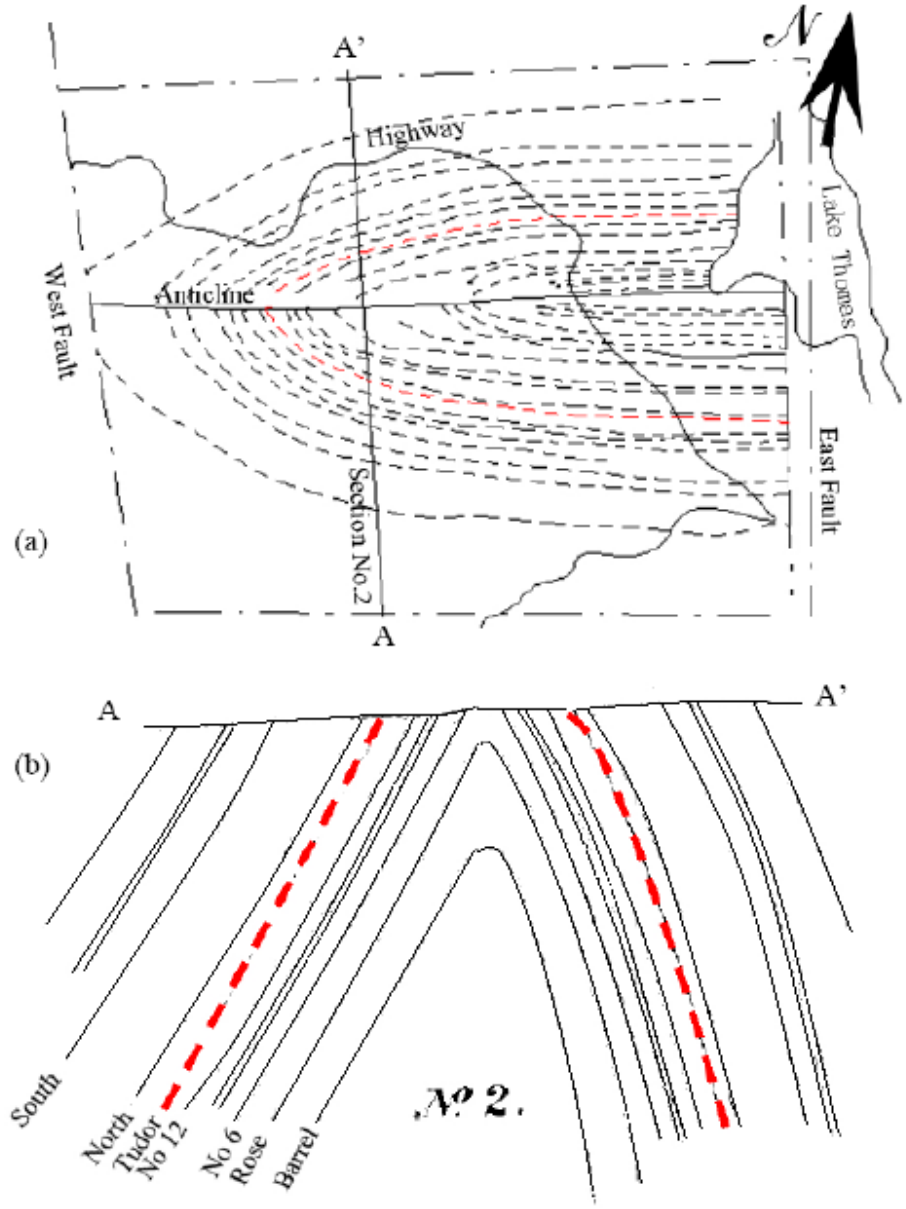

Figure 6.11 Sketch of plan view of West Waverley (a) shows the anticline, the two faults and the outcrop of leads of quartz, and one cross section (b) shows the different groups of leads, with some of the characteristic rocks with which each group is associated. The black dashed lines represent leads and the red dashed line stands for Tudor Lead to be detected (after Hind 1869).

In Nova Scotia, gold occurs as vein (lode) deposits and occurrences, modern placers, paleoplacers and as disseminated gold in various rock types. The vein or lode deposits are

predominantly associated with the Meguma Group slates and greywackes of the southern mainland including the Waverley Gold District. Virtually all of the established gold districts are vein deposits in the Meguma Group rocks. The bedrock consists of steeply dipping, low-grade metamorphosed greywackes and slates, with gold occurring in near-vertical quartz veins. Figure 6.11b also shows the different groups of leads, with some of the characteristic rocks with which each group is associated. From 1862 to1938, total gold production was 73,353 oz, from 161,876 tons of crushed quartz.

To summarize, the strata at Waverley are an elongated elliptical dome, whose long axis runs nearly east-west (N80°E). This geological domain experienced a series of disturbances of considerable magnitude in structure and disruption from extensive mining activities during three "Gold Rush" periods (Hind 1869), and so has a complicated topographical and geological structure.

Field Trial and Selection of Surveying Lines

In West Waverley, there are few rock exposures because the overburden composed of gravels and clays varies from a metre to 16 metres in depth. Also a few boulders of granite, derived from a range some kilometres to the north, are scattered here and there. Dense trees and bushes make accessibility difficult. There are some paths in the wooded area. Close to these paths, openings which are evidence of ground subsidence over abandoned mines were identified and marked by Nova Scotia Department of Natural Resources (NSDNR).

Based on accessibility, ground condition, openings close to veins as evidence of old mine workings and minimum length requirement for multichannel data acquisition, three locations were finally selected for this seismic investigation. The three lines (1, 2, and 3) are shown in Figure 6.12. All the three lines are within 150 m of the reach of the anticline and extend to about 35 metres long.

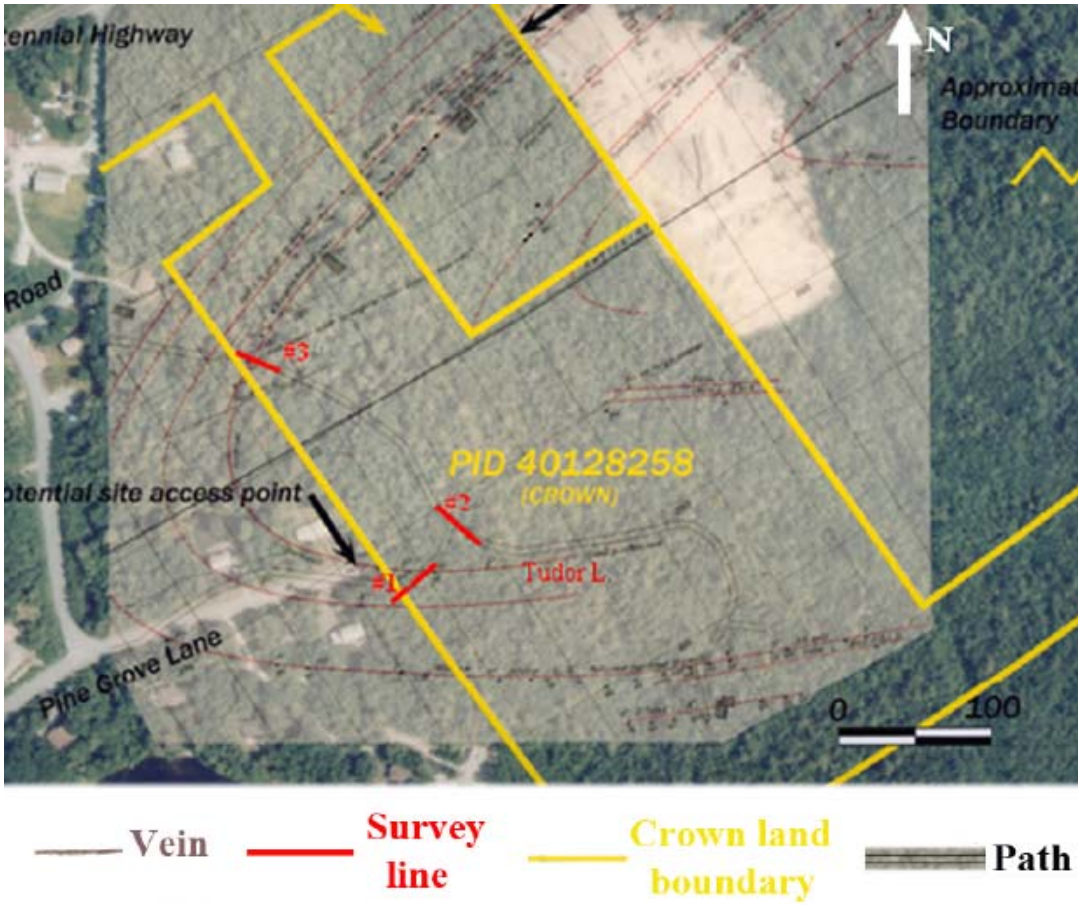

Figure 6.12 Aerial photo of Waverley shows paths in the woods and outcrop of leads. Black dots on leads are openings marked by NSDNR (scanned from hardcopy)

Lines #1 and #3 cross the Tudor Lead around the bend of the vein. According to records, two shafts were developed by North American Gold Mining Company to mine Tudor

vein to a depth of 40 m in the south and 80 m in the north. On opposite sides of line#1 there are two openings on Tudor Lead (Figure 6.13) due to mine subsidence. The direction of line#1 running southwest-northeast was defined as forward direction with stations from 0 to 38 at a spacing of 1 metre. So northeast-southwest was reverse direction.

Figure 6.13 Two openings in Tudor Lead are on the opposite sites of line#1

The geological section of line#1 is shown in Figure 6.14. There is gold deposit of Tudor Lead in formations with an apparent dip of about 45 degree because the line was not perpendicular to the lead. Tudor Lead in the south of anticline has a width range from 5 to 40 cm and this gold bearing vein was mined to a depth of from 10 to 40 m.

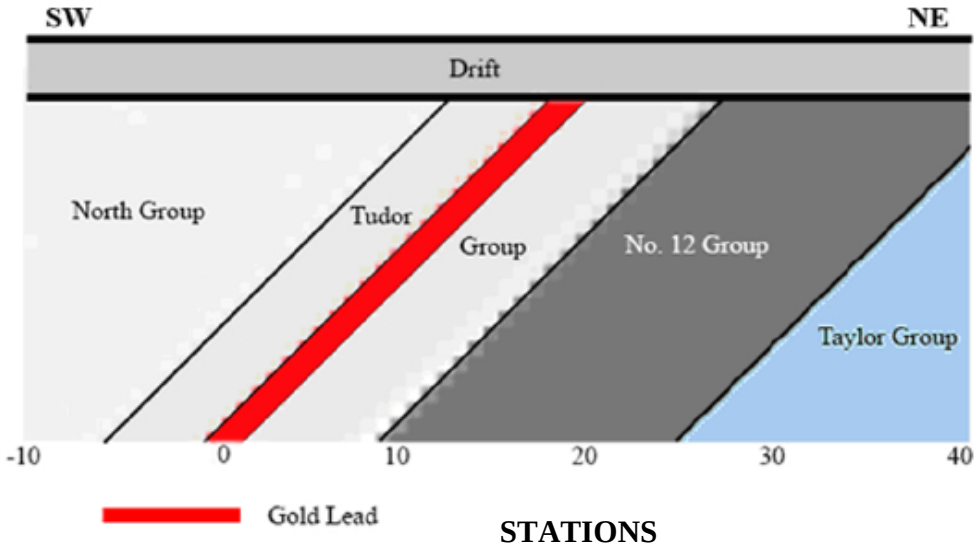

Figure 6.14 Geological section of line#1 showing gold deposit of Tudor Lead in deeply dipping formations. Tudor Lead in the south of anticline with a width range of 5 and 40 cm and mined to a depth range of 10 to 40 m.

Line#3 is over the same gold deposit of Tudor Lead in the same geological formations as line#1, but it is approximately perpendicular to the lead and situated in the north of the major anticline, so the dipping is toward north at 60 to 65 degree. The lead is about 40 cm wide and workings for it reached an average depth of 80 m. Line #3 intersected an obvious continuous subsidence at stations between 12 and 20 (Figure 6.15). Because the Tudor Lead in the north part was mined almost as twice deep as in the south of anticline, subsidence was more serious and clear and developed along the lead course. Similar to line #1, the direction of line#3 running northwest-southeast was defined as forward direction and this line.

Figure 6.15 Subsidence almost perpendicularly intersecting line#3 at stations between 12 and 20: Matthew Halliday stood there for a reference of the size and depth of this subsidence

For Line#2, southeast-northwest was defined as forward direction. The formations are the Taylor and Rose Groups on the south side of the major anticline and with a dip toward south of about 50 degrees. This line at station between 7 and 11 almost perpendicularly intersects a ditch nearly parallel to the major anticline. Because no veins exist or mine workings are recorded, it is not known what caused the ditch.

Data Acquisition

To cover the planned lines, stations were set at each metre from 0 to 38 (stations), 3 geophone positions were used to form a 34-channel record. The first geophone kept at

same position 5 m from source, the second geophone was 1 metre to 3 metre after the first one from position 1 to position 3, and all other geophones were 3 metres apart and would be moved 1 metre forward with position increase.

The superposition of the three arrangements would form a 34-channel line for seismic data record with 1 metre spacing from 5th station to 38th station. These configurations are shown in Figure 6.16.

However, because not all these survey lines of both forward and reverse directions are necessarily 38 metres long, for shorter lines, the last geophone might be set at the same station for all three positions, that is, only 30 channels would be displayed on a shot record.

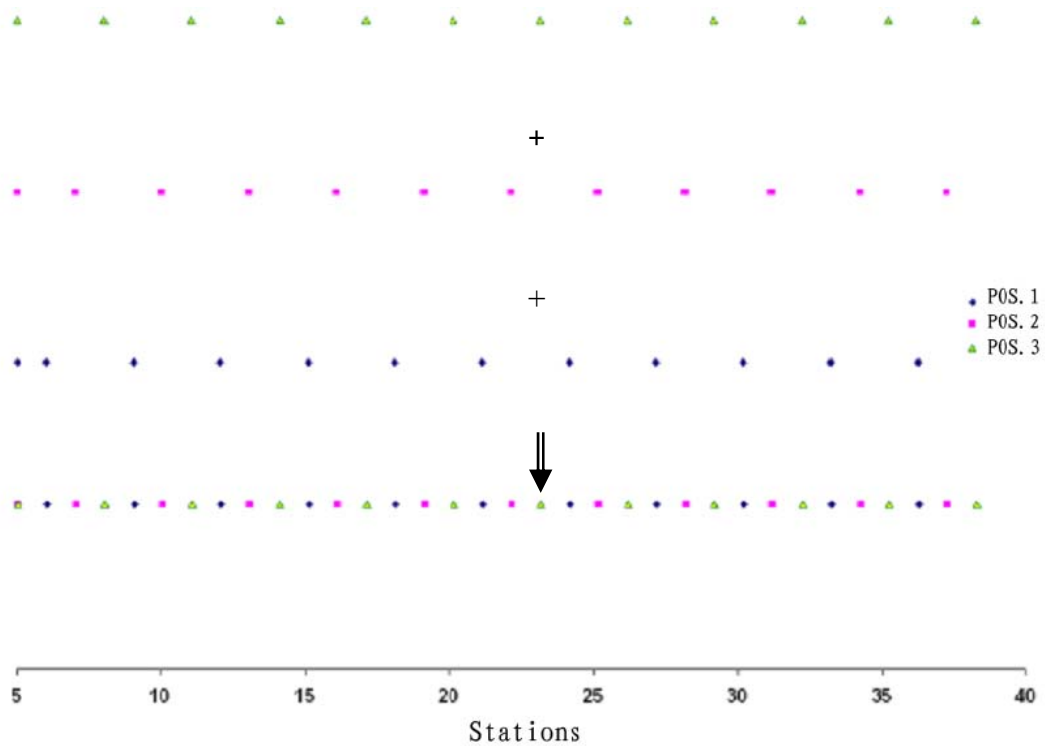

Figure 6.16 Geometrical arrangement of the 3 geophone positions. All geophones of each later arrangement move 1m farther from source than previous position but keeping the first geophone fixed. Finally a 34-channel array forms from superposition of 3 geophone positions

For reverse shots, the same geometrical configurations and corresponding superposition were used as forward shots. Sampling frequency was set at 500 Hz, and recording length was 0.6 second. For each position, 10 shots were applied for stacking.

Data Processing and Interpretation

The processing strategy applied to West Waverley data was similar to that applied to the Stellarton data. For line #1, both sledgehammer and weight drop were used as source for comparison (Figures 6.17 and 6.18) and back scattering energy was also enhanced to display the location of the potential mined workings (Figure 6.19). Figures 6.20 shows results for line #2 and Figure 6.11 shows results for line #3.

Raw field seismic sections (a and d), processed seismic sections (b and e) and their corresponding *f-k* displays (c and f) and SVF image (bottom) are shown in Figures 6.17, 6.18, 6.20 and 6.21. The field records both in *x-t* and *f-k* domains show a very complicated pattern as evidence of the history of geological structure and mining activities during periods of "Gold Rush". Some coherent noise might be present in the records: side scattering energy due to reflection or diffraction form near side variation, back scattering energy from lateral discontinuity in line, low frequency reverberations associated with loose rocky drift of the ground and high frequency reverberations associated with hard stiff quartz. As discussed in sections 3.2 and 3.4.3, the scattering energy appeared in negative quadrant in *f-k* plans of raw field data.

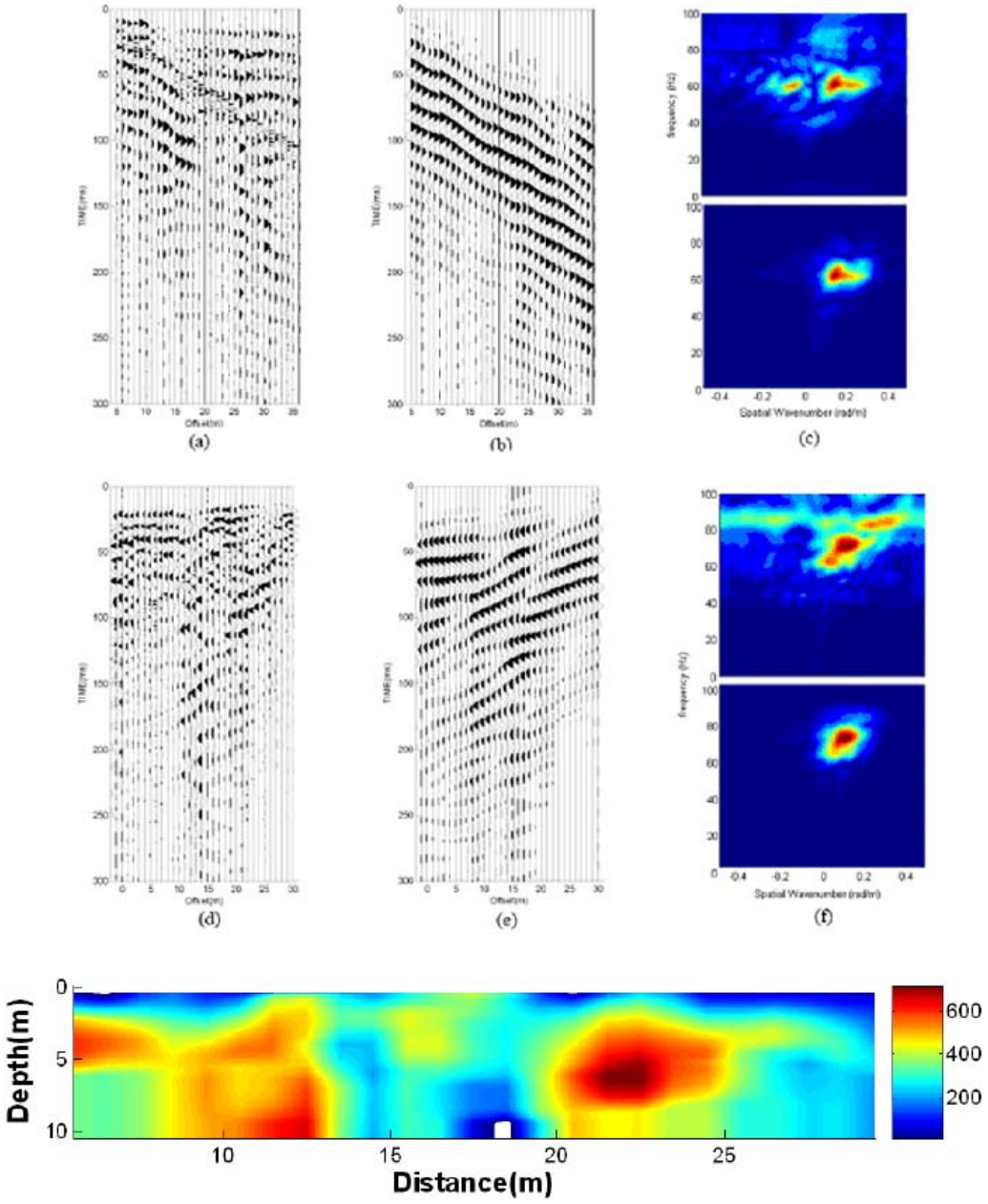

Figure 6.17 Line 1 using sledge hammer as source. Top row is for forward direction: (a) raw record, (b) processed record, (c)*f-k* displays before and after processing; second row is for reverse direction: (d) raw record, (e) processed record, (f)*f-k* displays before and after processing; bottom is SVF image.

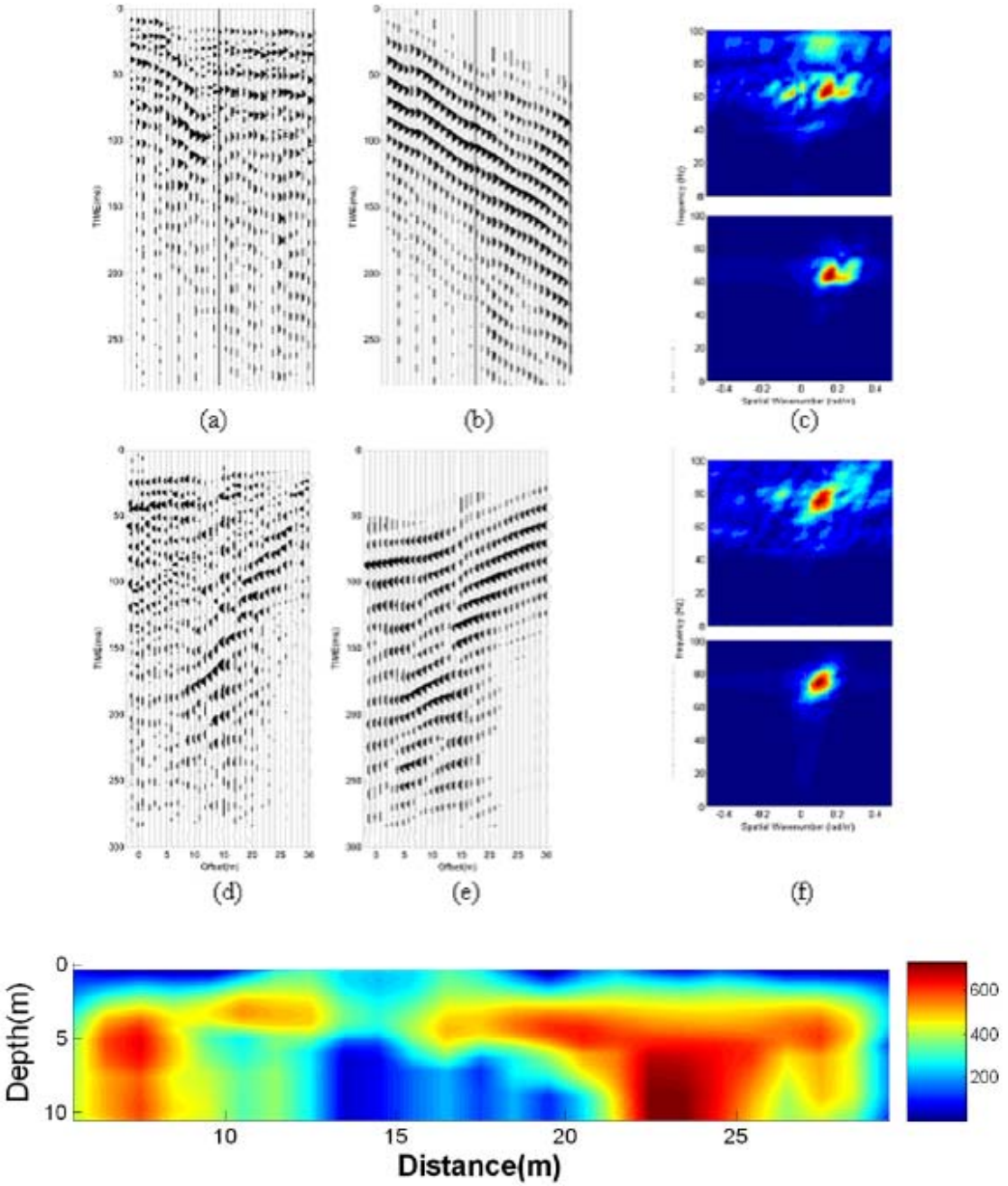

Figure 6.18 Line1 using weight drop as source. Top row is for forward direction: (a) raw record, (b) processed record, (c)*f-k* displays before and after processing; second row is for reverse direction: (d) raw record, (e) processed record, (f)*f-k* displays before and after processing; bottom is SVF image.

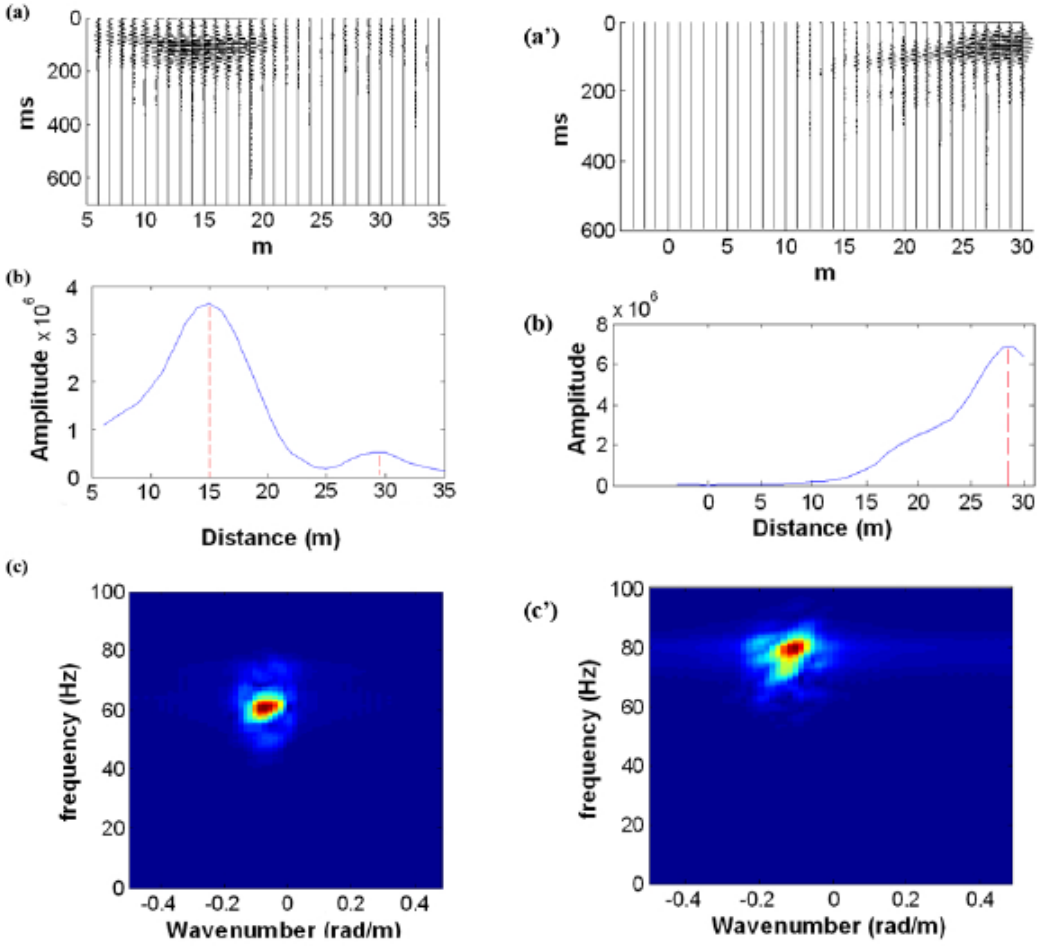

Figure 6.19 Back scattering analysis of Figure 6.15a, forward raw seismic data with hammer source (left column a, b and c), and of Figure 6.16d backward raw seismic data with weightdrop source (right column a', b' and c'): a and a' are seismic section, b and b' are the amplitude maxima of a and a', and c and c' are *f-k* spectra of a and a'.

First, consider line #1 from Figures 6.17 to 6.19. The first two groups of figures (Figures 6.17 and 6.18) show direct Rayleigh waves with a hammer source and a weight drop source respectively, and the third group (Figure 6.19) is back scattering images of the

same data as Figure 6.17a (forward shot with a hammer source) and Figure 6.18d (reverse shot using weight drop).

SVF images of both Figures 6.17 and 6.18 (bottom) display a weak section at a location between 14 and 20 m. The sharp contrast of shear velocity was caused by an anomaly in this survey line. Because the anomalous zone has a much slower shear velocity than its background, it indicates a weak zone or cavity under this location on line #1. This coincides well with Figures 6.13 and 6.14 where the Tudor Lead at this location on line #1 was mined.

However, when the back-scattered energy was examined, it revealed an anomaly. The back scattering energy distributed in negative quadrant, was detected using *f-k* filter. Figure 6.19 displays back scattering analysis of Figures 6.17a, the forward raw seismic data with a hammer source (left column a, b and c), and of 6.18d, the reverse raw seismic data with a weightdrop source (right column a', b' and c'). Back scattering events in this case were usually difficult to pick up because of strong interference with other seismic events (Figures 6.17 and 6.18). It is also difficult to display them in far field due to quick energy absorption after wave propagation in weak zones. However, an endeavor was made to process these two datasets. The result is shown in Figure 6.19. The top two seismic sections respectively display the back scattering events in the middle and the end of line #1 from forward shot and backward shot. The middle row displays the amplitude maxima of back scattering in every channel and shows two peaks at 15 and 28 m, which agree with the SVF images for direct Rayleigh waves. However, the anomaly at around 28 does need further field validation through physical approaches.

It is noted that it would be hard to tell which source, either hammer or weightdrop, is better for this line because both sources gave very similar results. However, the hammer is easier and more convenient to move and operate. So I prefer a sledgehammer to be source for field test using Rayleigh waves.

Consider line #2 (Figure 6.20) using a hammer source. This group of images has the same pattern seismic sections in the top and *f-k* spectra in the middle row before and after processing so increases confidence in the reliability of the seismic data. The processed data kept fundamental characteristics of the raw field data, which are supposed to be those of Rayleigh waves, after removal of noise.

The SVF image displayed a generally higher (compared to Stellarton Coalfield) shear velocity section with less variation. Because there is no gold-bearing vein or mine recorded, this line would be undisturbed. However, the unexplained ditch nearly perpendicular to line #2 at the location between stations 7 and 11 was displayed in the SVF image at stations between 8 and 11 m. In addition, considering that the layers covered by this line are sandwiched strata (Figure 6.11), there might be secondary faults caused by the major twisted anticline (only about 100 m from the line), so there would be some shear velocity contrast. As a result, lateral variations would be visible in the SVF image but are not strong.

Finally considering line #3 (Figure 6.21). The SVF image displays two different zones in this line. The section between 5 and 15 m has low shear velocity and the other section after 20 m has a high shear velocity. Because the strata here have a northward dipping (dip toward left in SVF image) of about 65 degrees with 40-cm-thick gold-bearing lead

and mining went down to a depth of 80 m, the affected area would be much wider in the subsurface. This phenomenon agrees well with the SVF image. The subsidence caused by mining was shown in Figure 6.15.

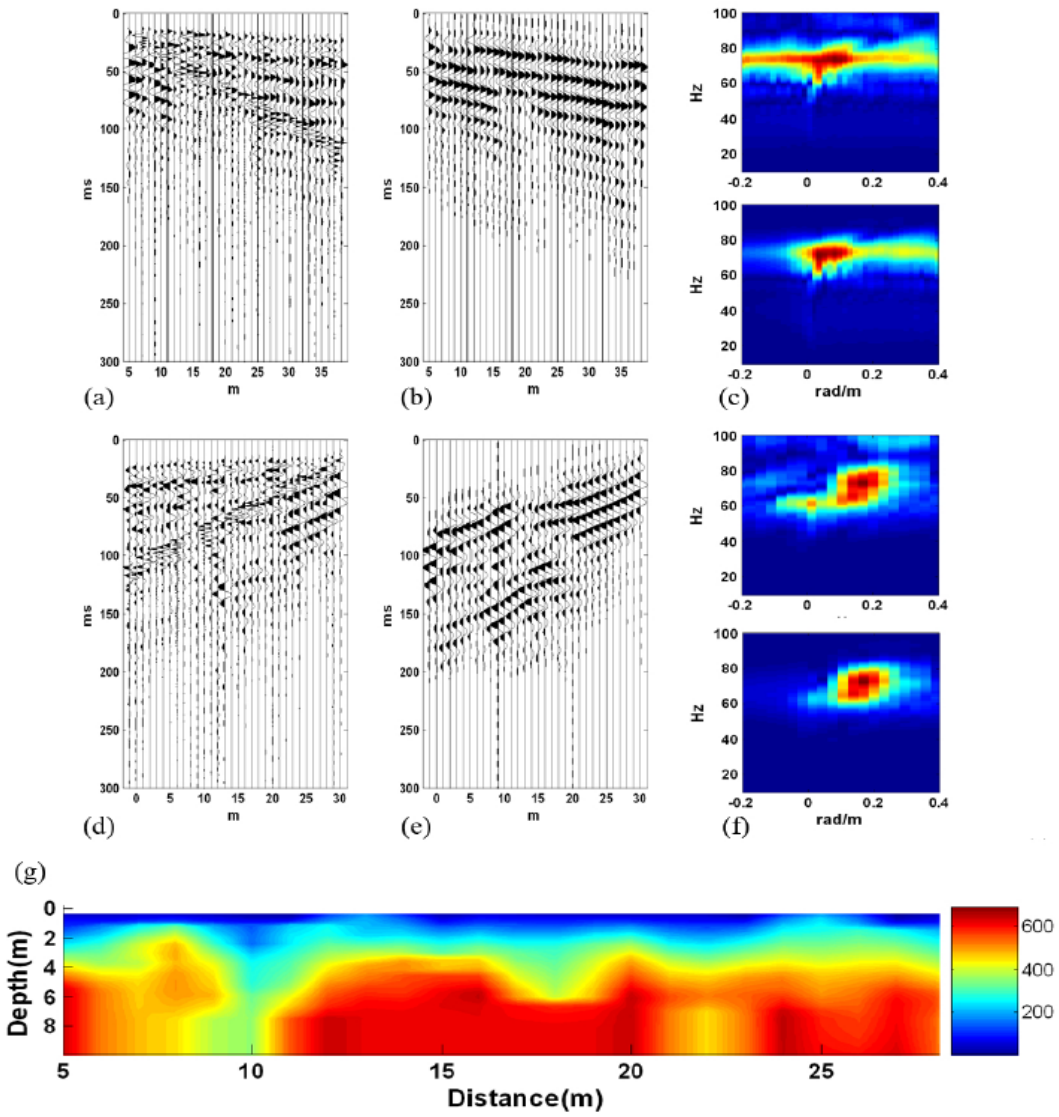

Figure 6.20 Line#2 using a sledge hammer as source. Top row is for forward direction: (a) raw record, (b) processed record, (c)*f-k* displays before and after processing; second row is for reverse direction: (d) raw record, (e) processed record, (f)*f-k* displays before and after processing; bottom is SVF image (g).

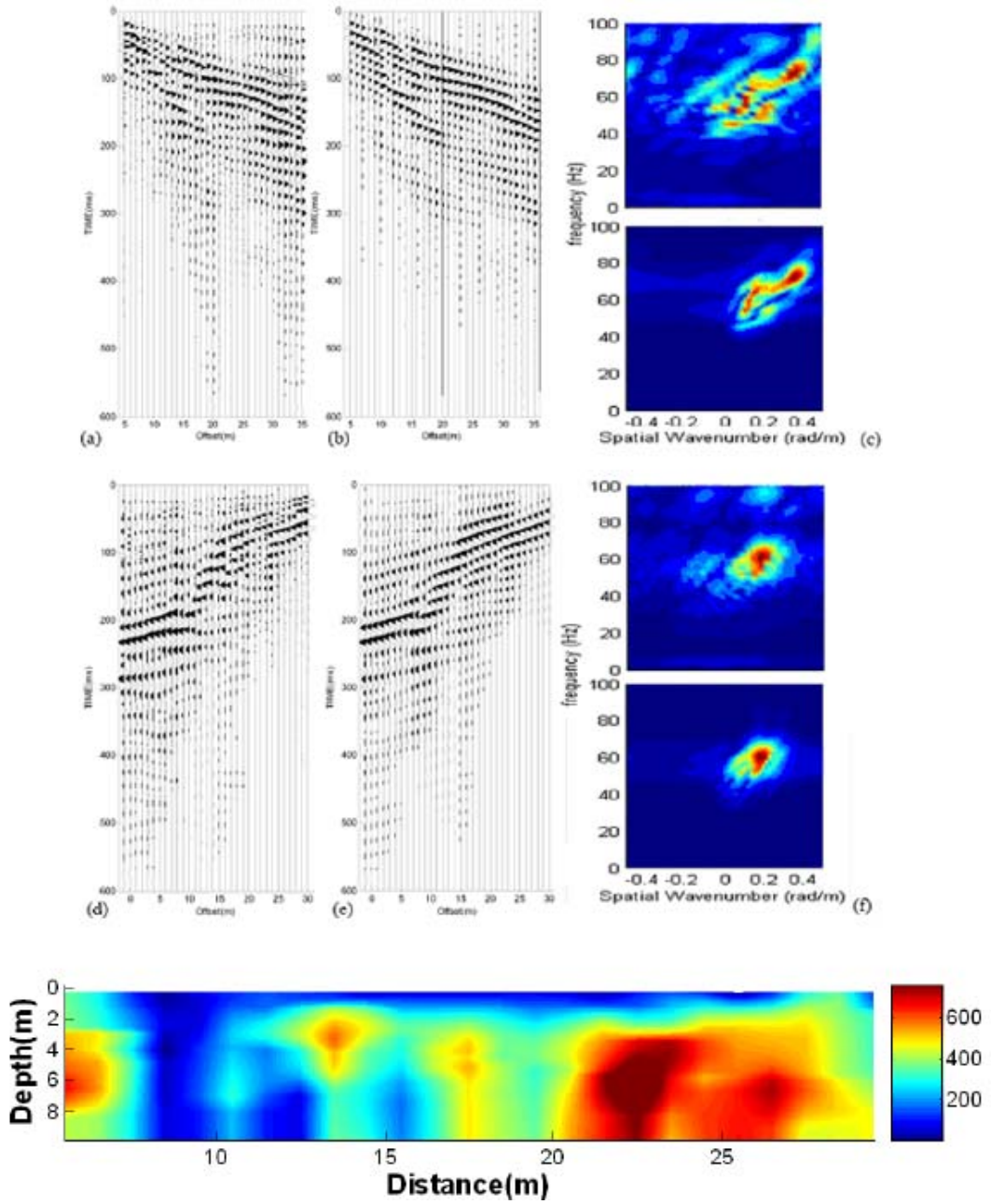

Figure 6.21 Line#3 with sledge hammer as source: Top row is for forward direction: (a) raw record, (b) processed record, (c)*f-k* displays before and after processing; second row is for reverse direction: (d) raw record, (e) processed record, (f)*f-k* displays before and after processing; bottom is SVF image

Liverpool

The Liverpool site is in the town of Liverpool, NS, just south of the Mersey River and north of Henry Hensy Drive (Figure 6.22).

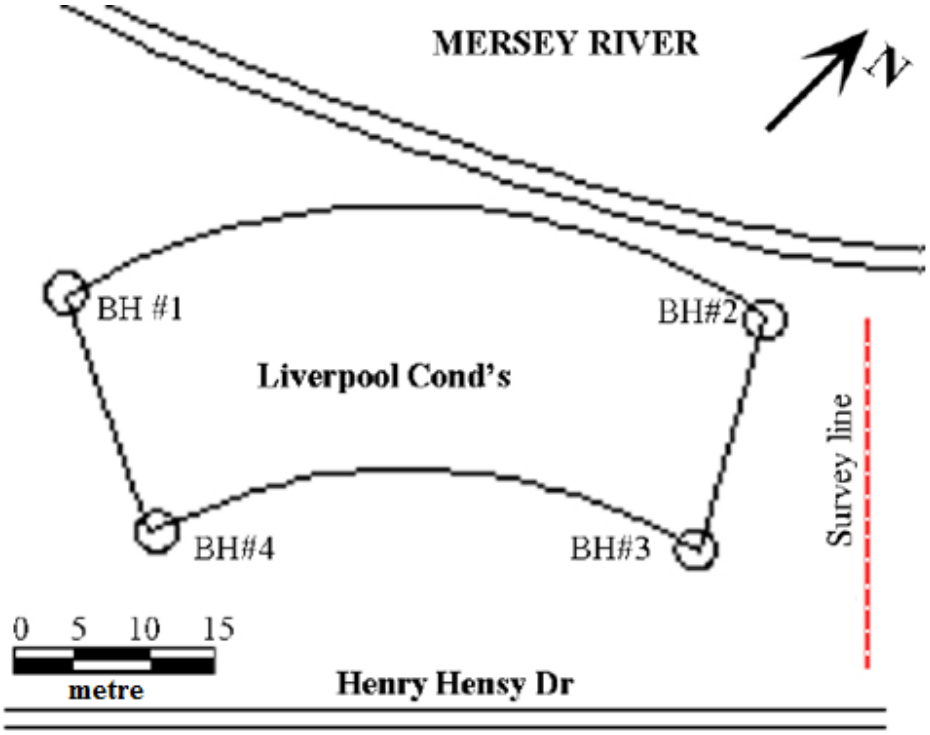

Figure 6.22 Plan sketch of Liverpool geotechnical site

It is fan shaped running along the river bank and is a relatively simple field of nearly horizontal strata. This site is about 20 m by 40 m and is a field which has a foundation under construction for Liverpool Condominiums. Inspec-Sol drilled four holes to depths ranging from 22 to 26 m in September 2006. These holes were located at the four corners

of the construction site. The borehole logs showed that the field is composed of three nearly horizontal layers. The top layer is fill which is loose to compact dark brown gravel and sand, some silt and boulders. The second layer is native soil which is loose to compact grey sand and silt with some gravel and organics. The second layer is underlain by mainly igneous bedrock.

The field trial was done on Sunday, December 28, 2006 in a flurry at a low temperature of -10 °C. Constrained by the size of this site, a 38-metre- long line was set nearly perpendicular to the river (Figure 6.22). Boreholes #2 near the river and #3 near Henry Hensy Drive are close to the two ends of the survey line. Three geophone positions were used in the same way as Waverley to form this 38-metre-long line, so the spacing was also 1 m. The source near Henry Hensy Drive, which would generate waves propagating towards the river, was set as forward direction, and the source near the river, which would generate waves propagating towards Henry Hensy Drive, was set as backward direction. Based on in-site testing, the sampling frequency was set at 1000 Hz and the record window length was set at 600 ms.

The seismic sections (Figure 6.23) are regular and do not show much dispersion. This could be due to this site having less velocity variation with depth (section 3.1). The SVF image (Figure 6.23 bottom) showed a velocity range between 100 to 300 m/s. The SVF image also gave two different sections in this line: one is before 20 m and the other is after 20 m. The first section has some lateral variation and lower shear velocity whereas the second section is more consistent and regular with a higher velocity. The third observation is the apparent layers from the SVF image. The top very low velocity layer should be top soil, then down to the layer of fill whose shear velocity gradually increases

with depth from 2m to 4 m. Next, the underlying native soil layer is very thin about 2 m thick and its velocity increases with depth. Finally, an irregular bedrock surface was displayed at an average depth of about 6 m. Because no layered model was used in inversion, there was no sharp contrast in the SVF image for layer interface determination.

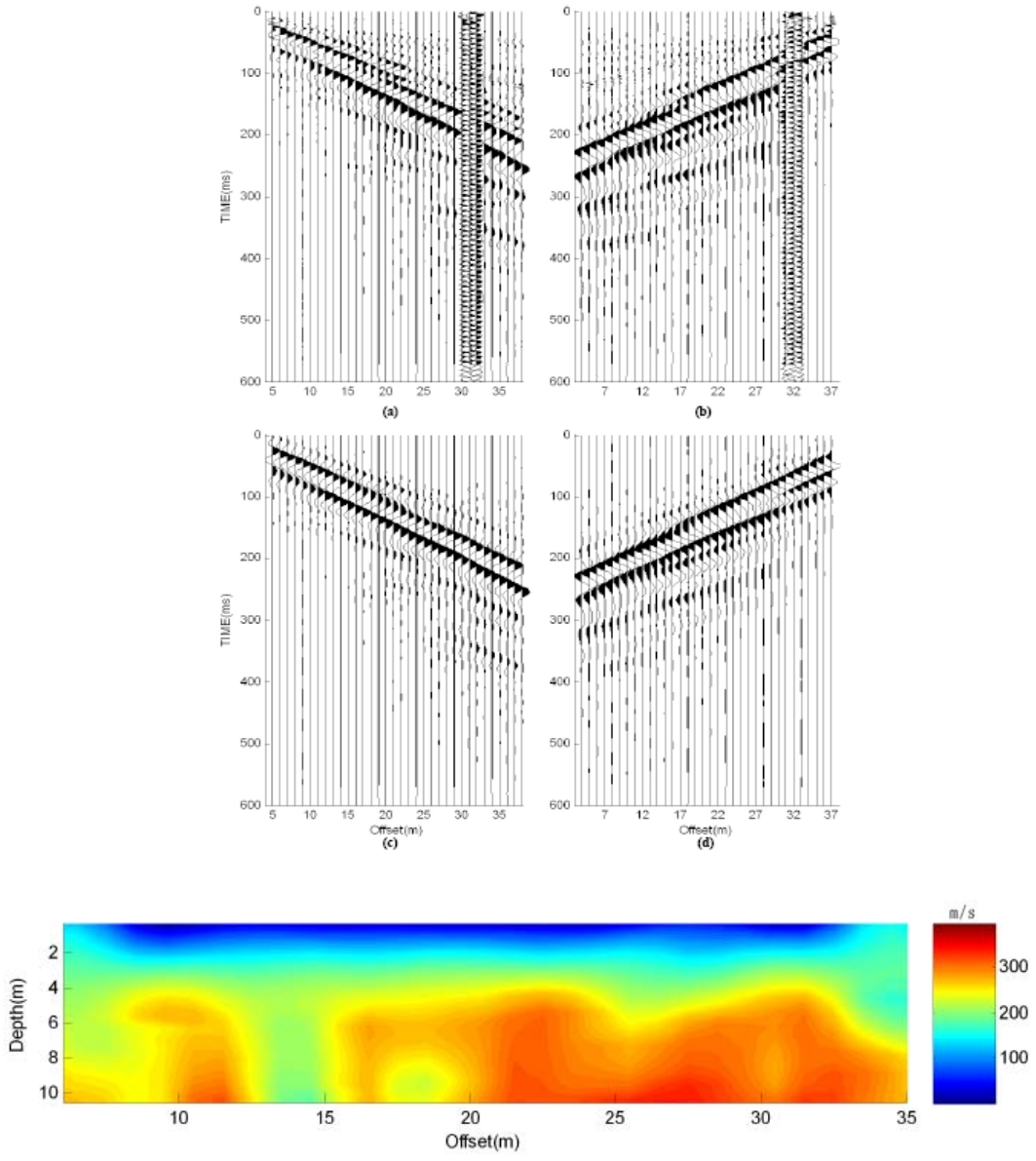

Figure 6.23 Liverpool imaging: Top row is for raw records in forward direction (a) and in backward direction (b), middle row is processed records (c) and (d), and bottom is SVF image

Now consider the refraction image in Figure 6.24. To enhance refraction events, a similar filtering strategy was used to remove most Rayleigh waves to yield seismic sections with remarkable refractions standing out (a, b). Then the refraction events could approximately be picked up in the seismic sections (crosses in black). The Plus-minus technique (c) was used to produce the bedrock profile (d)

The bedrock profile indicates an irregular bedrock surface at a depth ranging from 5.5 m at 10 to 9 m at 27 m. From the borehole logs, the bedrock has a tendency of gradual rise from northwest to southeast (Figure 6.23 and Table 6.1). Considering the survey line location related to these boreholes, the bedrock profile is reasonable.

Table 6. 1 Summary of strata from borehole logs

BH No.	1	2	3	4
Fill Depth (m)	0 - 3	0 - 3	0 - 4.5	0 - 4.2
Native Soil (m)	5 -8.8	3 - 7.6	4.5 - 6.7	4.2 - 8.1
Bedrock (m)	8.8 -	7.6 -	6.7 -	8.1 -

Finally, the SVF image, refraction bedrock profile and the two boreholes are sketched together for comparison in Figure 6.25.

First, the two different sections of the SVF image were well explained by the two boreholes. Borehole #3 describes the bedrock as “fractured igneous rock, medium fine grained, very poor quality” while borehole #2 labels the bedrock “undifferentiated igneous rock, medium fine grained, grey gneiss, and excellent quality”.

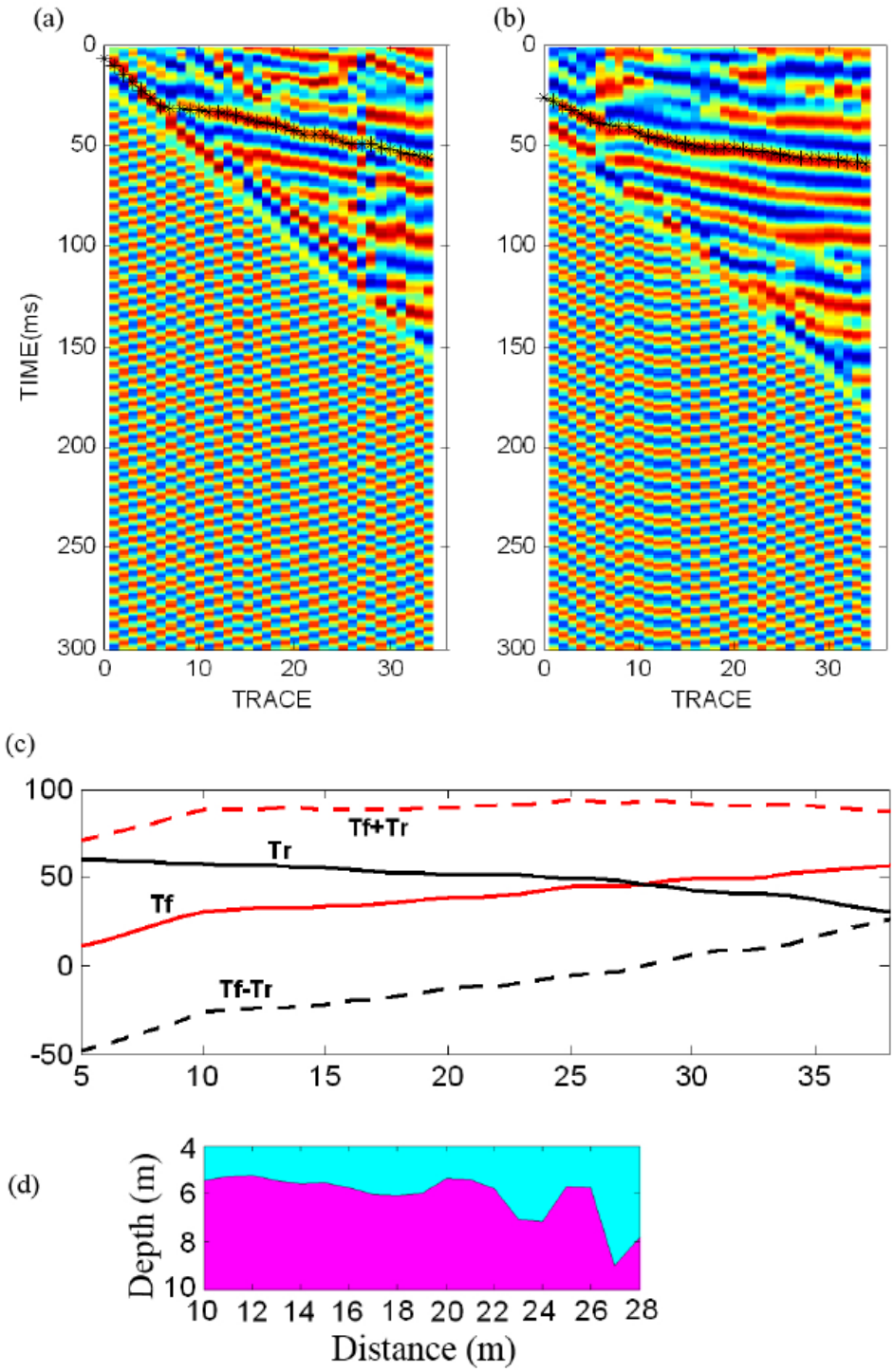

Figure 6.24 Refraction processing: refraction picking (a) and (b), plus-minus technique for estimation of velocity and bedrock depth (c), bedrock profile (d)

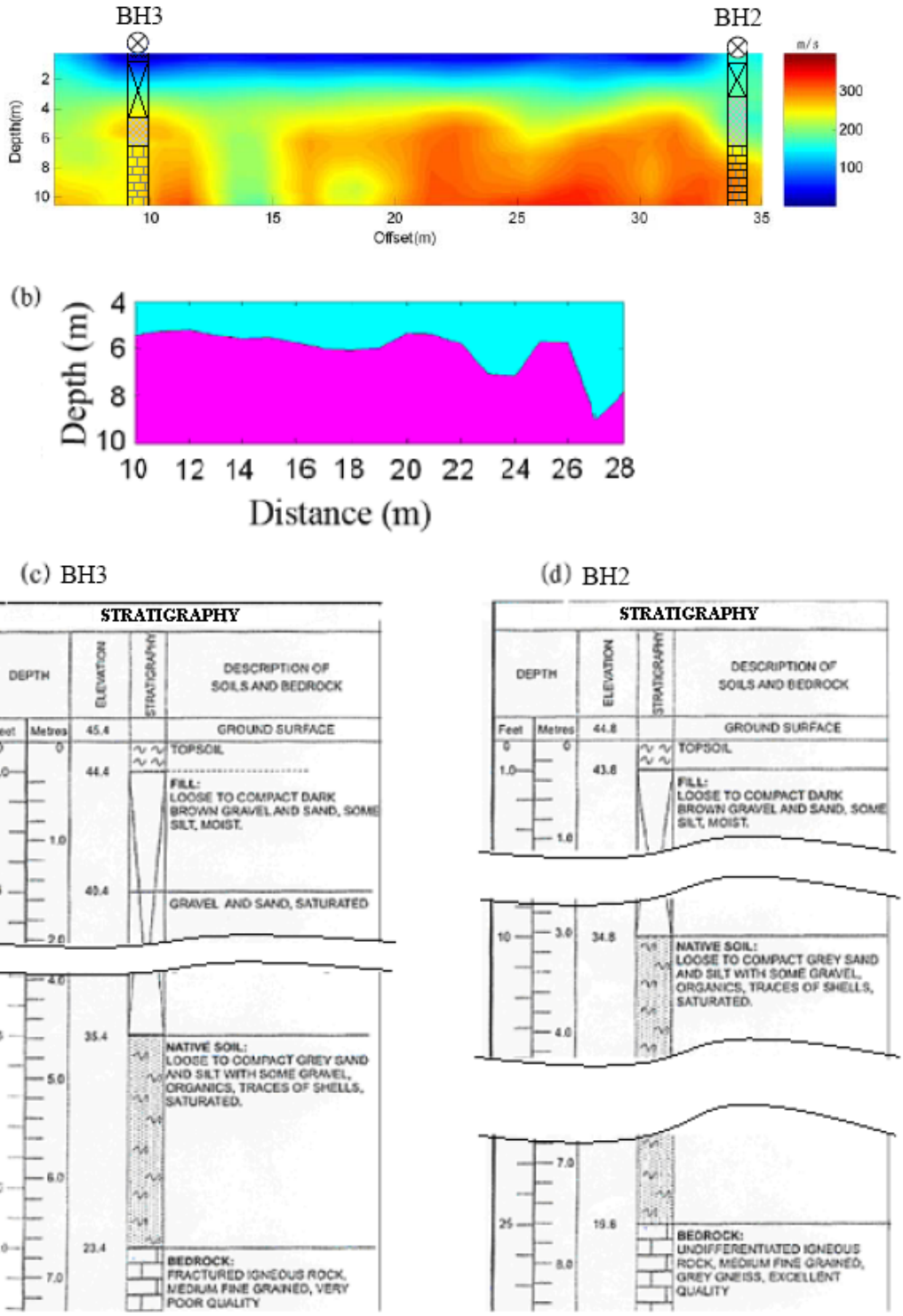

Figure 6.25 Interpretation for Liverpool site: (a) SVF image, (b) Refraction bedrock profile, (c) borehole #3 log, (d) borehole #2 log (Courtesy Inspec-Sol for bore logs). (the depth scale is different in a and b)

Secondly, the boreholes indicated the fill and native soil vary with depth from loose to compact, so their velocities will gradually increase with depth. Except that the velocity of bedrock is relatively constant, the velocity from fill to native soil continuously increases without sharp jump, so gave rise to difficulty in differentiation of these two layers.

The refraction here was manually picked up and inevitably involved in uncertainty to some extent. The refraction might present general information, which agrees with the SVF image, but the local details could be incorrect.

Discussion

The three fields represented three typical scenarios: horizontal formation, moderately dipping formation, and steeply dipping formation. Images from data processing of these field tests showed once again that the real world is rarely as simple as theoretical world,. The environment of the field consists of topography, geological formation, geology structure, imprints of human activities, weather conditions, etc. Besides, data acquisition equipment, geometrical parameters, acquisition system parameters and field operations all impact the quality of field data. Most importantly, it is necessary that, in the acquired seismic data, the expected energy type has to be much more than any other types of energy and accounts for major percentage. It is the first step of success to acquire high quality data. Successful processing depends on field data quality.

The filtering strategy introduced in this study works well and is successful in isolating Rayleigh waves, refractions or back scattering energy. The filtered data maintained the typical characteristics of the energy types after removing most other wave energy as

noise. The filtering operation introduced here is convenient and straightforward, and the filtering effect is noticeable for all these data.

It is helpful to make comparison of SVF images from direct Rayleigh waves with refraction bedrock profile and back scattering images. The surface wave method can be a principal technique applied to various geology formations whereas refraction and back scattering can be complementary methods. Comparison and field validation would improve confidence if the difference between them can be explained.

CHAPTER 7: CONCLUSION

The objectives of this research have been fundamentally achieved through literature review, theory, methodology development and field investigations. A filtering strategy was introduced and successfully applied to field seismic data. Pair-channel analysis of multichannel seismic data was introduced for reliable calculation of dispersion curves through a new wavelet technique to yield shear velocity field (SVF) images. The SVF images inverted from dispersion curves present a straightforward display of the subsurface structure. This allows subsurface anomalies to be localized because of the strong contrast with their surroundings. Evaluation of refractions and back scattering energy were also conducted in this research. Comparison of the seismic images showed that anomalies were approximately coincident with the presence of open holes on the surface, surface subsidence patterns, and known tunnels.

This research evaluated shortcomings of both SASW and MASW techniques in practical applications, especially for media with significant lateral variations. Based on the evaluation, pair-channel analysis of seismic data using wavelets was introduced to yield better solutions. Fundamentally, the SASW requirement for high coherence functions only results in good images for media without lateral variation, while MASW techniques, generally using transforms for multichannel analysis, cannot detect local features.

The deficiency in Fourier Transform for detection locally in time was also evaluated because this technique only uses one smooth sinusoidal wavelet.

Currently, since multichannel data acquisition makes it more efficient to acquire field data, most researchers prefer multichannel transform algorithms to pair-channel processing on the acquired data, they even go so far to discard basic pair-channel analysis even though it can interpret more details of local spatial information. In other words, the multichannel transform techniques could miss potentially important data buried in the multichannel seismic data resulting from the lateral local difference in the media. Pair-channel analysis using the wavelet technique can detect spatial changes in the

multichannel seismic data and localize any frequency anomaly in time. Therefore it is a worthwhile endeavor to conduct pair-channel analysis for multichannel data to overcome shortcomings of SASW and MASW, and to take advantages of the quick field data acquisition of MASW. The pair-channel analysis of multichannel seismic data developed in this research is therefore efficient for anomaly localization.

This research also includes system development. Our hardware was developed based on Seistronix seismograph. The hardware system consists of two 12-channel systems, a series of hammers of different weights, one 12 kg weightdrop, and one 60-metre-long reverse source cable. The system is portable and adaptable to allow quick field data acquisition. The reverse data acquisition not only allows the system to collect Rayleigh waves, but also to conveniently collect refraction data if necessary. Meanwhile, the software was also well developed, beginning with data format conversion, demultiplexing, superposition of different positions to form a long line with enough channels and geometry combination to yield the final seismic data, and then displaying these data in many different ways including 2D varying area method, global attenuation method, local average method and colour method and 3D display method. A rich and convenient filtering package has been developed in this thesis. I also believe the SVF imaging technique has given vivid and dramatic effects in the field data processing.

Another contribution is Rayleigh wave database construction. All field trial, raw field data, processed data and results, reports have been archived, which is important for future study and practical application.

In addition, after several years of field work, we have built a regular and routine operational procedure from field reconnaissance, line selection, line surveying, preparation for seismic investigation and field seismic data acquisition. This allows field work to be efficient and effective.

The field tests predict the promising applications in the following aspects:

i) Geohazard in environmental and civil engineering,

ii) Slope stability analysis in mining engineering,

iii) Highway hazard assessment in transportation, and

iv) Roof assessment for ground control in underground mining.

Recommendations for future work include:

(i) numerical modeling,

(ii) inversion techniques, and

(iii) 3-D surface wave survey.

REFERENCES

Aki, K., Richards, P.G., 2002. *Quantitative Seismology*, University Science Books, Sausalito, CA.

Alrifaiy, I. A., 1990. Land Subsidence in the Aldahr Residential Area in Kuwait: A Case History Study, Quarterly Journal of Engineering Geology, 23, 33746.

Al-Shayea, N., 1994. *Detection of Subsurface Cavities Using the Spectral-Analysis-of-Surface-Waves Method*, Doctor of Philosophy Dissertation, Department of Civil and Environmental Engineering, University of Michigan

Aminnedjad, B. and Butt, S. D., 2003, Imaging Abandoned Underground Mines and Assessing Geotechnical Hazards Research Project, Phase 1 Final Report – Assessment of State of the Art for Nondestructive Geophysical Imaging Technology, unpublished report, 2003.

Avar, B. B. And Luke, B. A., 1999. Roadside application of seismic surface waves over abandoned mines, Proceedings of the Symposium on the Application of Geophysics to Engineering and Environmental Problems - SAGEEP '99, Oakland, California, March 14-18, EEGS, 31-40.

Ballard R.F. 1964. Determination of soil shear moduli at depth by in situ vibratory techniques, Waterways Experiment Station, Miscellaneous Paper No. 4-691, December 1964.

Bates, J. L. E., 1987. Gold in Nova Scotia, Nova Scotia Dept. of Mines and Energy

Biot, M. A., 1956.The theory of propagation of elastic waves in a fluid saturated porous solid: I. Low frequency range, J. Acoust Soc Am., vol. 28

Bishop, I., Styles, P., Emsley, S. J. and Ferguson, N. S., 1997. The detection of cavities using the microgravity technique: case histories from mining and karstic environments in

Modern Geophysics in Engineering Geology, Mccann, Fenning, & Reeves (Eds), Geol. Soc. of London Special Publication No 12, 155168.

Bohlen, T. and Saenger, E. H., 2006. Accuracy of heterogeneous staggered-grid finite-difference modeling of Rayleigh waves, Geophysics 71, T109.

Brown, G.C. and Mussett, A.E., 1981. The inaccessible Earth, George Allen & Unwin, London, UK

Buchwald, V.T. 1961. Rayleigh waves in transversely isotropic media, Quarterly Journal, Mech. and Appl. Math, vol. 14.

Burger, H., 1992. Exploration Geophysics of the shallow subsurface, Prentice Hall, Inc.

Butler, D. K, 1984. Microgravimetric and gravity gradient techniques for detection of subsurface cavities, Geophysics, Vol. 49, No. 7, pages 1084-1096.

Butt, S. D., Xu C. Q, Vance M. D., and Corbett G.C., 2005. Imaging steeply-dipping near-surface abandoned mine workings using surface seismic waves, CIM Bulletin, Vol. 98.

Calder, J. H., Gillis, K. S., MacNeil, D. J., Naylor, R. D. and Campbell, N. W., 1993, One of the greatest treasures -The geology and history of coal in Nova Scotia, Canadian Cataloguing Publishing Data

Castagna, J.P., Batzle, M.L. and Eastwood, R.L., 1985. Relationship between compressional wave and shear wave velocities in clastic silicate rocks: Geophysics, Vol. 50.

Chamon, N. and Dobereiner, L. 1988. An example of the uses of geophysical methods for the investigation of a cavern in sandstones, Bulletin of The International Association Of Engineering Geology, No. 38, Paris, 3743.

Chiang, C. M. and Mostafa, A. F., 1981. Wave induced responses in a fluid filled poro-elastic solid with a free surface boundary layer theory, Geophysics J R Astr Soc, Vol 66, pages 597-631.

Chik, Z., T. Islam, M.M. Mustafa, H. Sanusi, S.A. Rosyidi and M.R. Taha, 2009. Surface wave analysis using morlet wavelet in geotechnical investigations. J. Applied Sci., 9: 3491-3501.

Coduto, Donald P. 2001. Foundation design – principles and practices (second edition), Prentice Hall, Inc.

Colley, G. C. 1963. The detection of caves by gravity measurements, Geophysical Prospecting, 11, 110.

Nkemzi, D., 1997. A new formula for the velocity of Rayleigh waves, Wave Motion 26, pages 199-205.

Daniels, J. 1988. Locating caves, tunnels and mines, geophysics: The Leading Edge of Exploration, 7, No. 3, 327.

Dunkin, J W., 1965. Computation of model solutions in layered elastic media at high frequencies, Bull Seisim Soc Am.

Emsley, S. J., Summers, J. W. and Styles, P., 1992. The detection of subsurface mining related cavities using the microgravity technique, Proc. Conf. Construction over Mined Areas, Pretoria, South Africa.

Ewing, W.M., Jardetzky, W.S., Press, F., 1957, Elastic waves in layered media, McGraw Hill Book Co. Inc., New York.

Fajklewicz, Z. 1976. Gravity vertical gradient measurements for the detection of small geologic and anthropogenic forms, Geophysics, 41, 101630.

Ferguson, N. S. and Styles, P. 1992. The detection and delineation of subterranean cavities by the microgravity method and subsequent image enhancement, Annales Geophysicae, vol. 10.

Forbriger, T., 2003. Inversion of shallow-seismic wavefields: ii. inferring subsurface properties from wavefield transforms, Geophysical Journal International June 2003, Vol. 153, No. 3, 735-752.

Foti, S., 2000. Multistation methods for geotechnical characterization using rayleigh waves, Ph.D. Dissertation, Ingegneria Geotecnica, Universuty Deli Studi.

Fountain, L. S., 1977. Detection of subsurface cavities by surface remote sensing techniques: in fundamental concepts in emg signal acquisition, Geophysics, 33, 838-842.

Ghatge, S. L., 1993. Microgravity method for detection of abandoned mines in New Jersey, Bulletin of The Association of Engineering Geologists, 30, 7985.

Graff , K.F., 1975. Wave motion in elastic solids, Dover, New York.

Grand, T., 1993. Gravity measurement for cavity detection, Scintrex Technical Information [online].

Grandjean, G. and Leparoux, D., 2004. The potential of seismic methods for detecting cavities and buried objects: experimentation at a test site, Journal of Applied Geophysics, Volume 56, Issue 2, June 2004, Pages 93-106.

Gritto, R. and Majer E.L., 2000. Seismic mapping of subsurface cavities, conference proceedings of the annual symposium on The Application of Geophysics to Engineering and Environmental Problems (SAGEEP), Arlington, VA, 1215-1244.

Gucunski, N. and Shokouhi, P., 2004. Detection and characterization of cavities under the airfield pavements by wavelet analysis of surface waves, presented for the 2004 FAA Worldwide Airport Technology Transfer Conference, Atlantic City, New Jersey.

Gucunski, N. and Woods, R. D., 1991. Instrumentation for SASW testing: geotechnical special publication No. 29: recent advances in instrumentation, data acquisition, and testingin soil dynamics, American Society Of Civil Engineers, New York.

Harkrider, D G., 1964. Surface waves in multilayered elastic media, Bull. seism soc A., vol. 52(2).

Haskell, N.A., 1953. The dispersion of surface waves on multilayered media, Bulletin of the Seismological Society of America, vol. 43 (1).

Hind, H. Y.,1869. Report on the Waverley gold district with geological maps and sections, Annand (References in Halifax Public Libraries, Call #: 557.16/H662r, Format: Non-circulating).

John, P. 1961. Rayleigh waves in a porous, elastic, saturated solid, J. Acoustical Society of America, 33(7):625-630.

Jones, R.B., 1962. Surface wave technique for measuring the elastic properties and thickness of roads: theoretical development, British J. of Applied Physics, vol. 13.

Knopoff, L., 1964. A matrix method for elastic wave problems, Bull Seisim Soc Am., 54(1): 431-438.

Lai, C.G. and Rix, G.J., 1999. Inversion of multi-mode effective dispersion curves, Pre-Failure Deformation Characteristics of Geomaterials, Jamiolkowski M., Lancellotta R. and Lo Presti D. eds, Balkema, Rotterdam.

Leparoux, D., Bitri, A., Grandjean, G., 2000. Underground cavities detection: A new method based on seismic Rayleigh waves, EJEEG, Vol. 5.

Liu, Y., 2001, Surface wave sounding guide, Beijing Research Institute of Hydropower and Geophysical Surveying.

Louie, J. L., 2001. Faster, Better: Shear wave velocity to 100 metres depth from refraction microtremor arrays, Bulletin of The Seismological Society Of America, Vol. 91, No.2 (April), 347-364.

Lyness, D. 1985. The Gravimetric detection of mining subsidence, Geophysical Prospecting, 33.

Malischewsky, P.G., 2000. Comment to "A new formula for the velocity of Rayleighwaves" by D. Nkemzi, [Wave Motion 26 (1997), 199-205],Wave Motion 31, pages 93-96.

Manning, P. M. and Margrave, G. F., 1999. Rayleigh wave modeling by finite difference, SEG Expanded Abstracts.

Miller, R. D., Park, C. B., Ivanov, J. M., Xia, J., Laflen, D. R., and Gratton, C., 2000, MASW to investigate anomalous near-surface materials at The Indian Refinery in Lawrenceville, Illinois, Kansas Geology Survey Open-File Report 2000-4, Lawrence, Kansas.

Miller, R. D., Xia, J., Park, C. B., 1999. Using MASW to map bedrock in Olathe, Kansas. Kansas Geology Survey open-file report 99-9, Lawrence, Kansas.

Mokhtar, T. A., Herrmann, R. B. and Russell, D. R., 1988. Seismic velocity and Q model for the shallow structure of the Arabian shield from short-period Rayleigh waves, Geophysics 53, 1379.

Mussett, A.E. and Khan, A. M., 2000. Looking into the Earth: An introduction to geological geophysics, Published by Cambridge University Press, October 2000.

Nasseri-Moghaddam, A., Cascante, G., Phillips, C., and Hutchinson, J, 2004. A new quantitative procedure to determine the location and embedment depth of a void with surface waves, SAGEEP Proceedings, page1582.

Nasseri-Moghaddam, A., Cascante, G., Phillips, C., and Hutchinson, J. 2007. Effects of underground cavities on Rayleigh waves-field and numerical experiments, Soil dynamics and earthquake engineering, 2007, vol. 27, pages 300-313.

Nazarian, S. and Desai, M. R., 1993. automated surface wave method: field testing, Journal of Geotechnical Engineering, V. 119*,* P. 1094-1111.

Nazarian, S., and Stokoe II, K. H., 1984. In situ shear wave velocities from spectral analysis of surface waves, Proceedings of The World Conference on Earthquake Engineering, V. *8,* San Francisco, Calif., July 21-28.

Nazarian, S., and Stokoe, K.H. II, 1985, In-situ determination of elastic moduli of pavement systems by spectral-analysis-surface-waves method (practical aspects), research report 368-1F, Center for Transportation Research, the University of Texas At Austin, Texas.

Neumann, R., 1967. La gravimetrie de haute precision application aux recherches de cavities, Geophysical Prospecting, 15, 11634.

Oppenheim, A. V. and R.W. Schafer. discrete-time signal processing, Englewood Cliffs, NJ: Prentice-Hall, 1989.

Owen, T. E., 1983. Detection and mapping of tunnels and caves, Development in Geophysical Exploration Methods, Volume 5, 1612-58.

Park, H.C. and Kim, D. –S., 2001. Evaluation of the dispersive phase and group velocities using harmonic wavelet transform, NDT & E International, Vol.34, No. 7.

Park, C.B., Miller, R.D., Xia, J., 1999. Multichannel analysis of surface waves, Geophysics, Vol. 64, No. 3.

Patterson, D. A, J.C. Davey, A.H. Cooper, & J.K. Ferris, 1995. The investigation of dissolution subsidence incorporating microgravity geophysics at Ripon, Yorkshire, Quarterly Journal of Engineering Geology, 28, 8394.

Phillips, W. J., 2005. Graduate course note -- Wavelets and Filter Banks. Dept. of Engineering Mathematics, Dalhousie University.

Pullan, S.E., 1990,Recommended standard for seismic (/radar) files in the personal commuter environment: Geophysics, 55,no. 09, 1260-1271.

Qiu, E. R., Class notes -- Mining Technology, Henan University of Technology, 1986.

Rabiner, L. R.. and Gold, B., 1975. Theory and application of digital signal processing. Englewood Cliffs, NJ: Prentice-Hall.

Rahman, M. and Barber, J.R., 1995. Exact expressions for the roots of the secular equation for Rayleigh waves, ASME, J. Appl.Mech. vol.62, pp250-252.

Rayleigh, L. 1887. On waves propagated along the plane surface of an elastic solid, Proceedings of the London Mathematic Society, Vol.17.

Richart, F.E., Wood, R.D., Hall, J.R., 1970. Vibration of soils and foundations, Prentice-Hall, New Jersey.

Rix, G.J., 1988. Experimental study of factors affecting the spectral-analysis-of-surface-wave method, PhD dissertation, University of Texas.

Rosebaum, J. H., 1964. A note on the computation of Rayleigh wave dispersion curves for layered elastic media, Bull seismic soc Am., 54(3).

Royer, D., 2001. A study of the secular equation for Rayleigh waves using the root locusmethod, Ultrasonics 39, 223-225.

Ryall, P. J.C., 2004. Graduate class notes of Applied Geophysics. The Earth Science, Dalhousie University.

Schmitz-Hübsch H., Schuh H. 1999, Seasonal and Short-Period Fluctuations of Earth Rotation Investigated by Wavelet Analysis, Technical Report Nr. 1999.6-1, Department of Geodesy and Geoinformatics, Universität Stuttgart : ”Quo vadis Geodesia ...?”, Festschrift for Erik W. Grafarend on the occasion of his 60th birthday, F. Krumm, V.S. Schwarze (Eds), 421-431.

Schröder, C. T. and Scott, W. R. Jr. 2001. On the complex conjugate roots of the Rayleigh equation: The leaky surface wave, J. Acoust. Soc. Am. Vol. 110, pages. 2867-2877.

Schwab, F. A. and Knopoff, L. 1984. Seismic surface waves, Methods in computational physics, Academic press, Inc., San Diego, 11: 87-180.

Sheriff, R.E., Geldart, L.P., 1995. Exploration seismology, Cambridge University Press.

Szelwis, R. and Behle, A., 1984. Shear-wave velocity of the weathering zone from multimodal Rayleigh waves, SEG Expanded Abstracts.

Tajuddin, M., 1984. Rayleigh waves in poroelestic half space, J. accoust soc Am., 75(3):682-684.

Tallavo, F., Cascante, G., and Pandey, M. 2009. Experimental and numerical analysis of MASW tests for detection of buried timber trestles. Soil Dynamics and Earthquake Engineering, Vol. 29, pages 91-102

Tejero, A., Chavez, R.E., Urbieta, J. and Flores-Marquez, E.L., 2002. Cavity detection in the southwestern hilly portion of mexico city by resistivity imaging, Journal of Environmental and Engineering Geophysics, Vol. 7, No. 3, Pp. 130–139.

Telford, W. M., Geldart, L.P. and Sheriff, R.E., 1990. Applied geophysics, Cambridge University Press.

Terzaghi, Karl 1939. Soil mechanics – a new chapter in engineering science, Proceedings of te institute of civil engineers, vol.12.

Thomson, W. T, 1950.Transmission of elastic waves through a stratified solid medium, J. Appl. PHYS., vol. 21.

Vogelaar, B.B.S.A., 2001. Cavity detection: a feasibility study towards the application of seismic surface wave stack methods for the identification and localization of underground voids, Ph.D. thesis, University of Utrecht, Netherlands.

Ward, S. H., 1990. Resistivity and induced polarization methods, Geotechnical and Environmental Geophysics, Vol. 1.

Wolfe, P.J., Richard, B.H., Hauser, E.C., Hicks, J.D., 2000. Identifying potential collapse zones under highways, Proceedings of the Symposium on Application of Geophysics to Environmental and Engineering Problems (SAGEEP).

Xia, J., Chen, C., Li, P.H. and Lewis, M.J., 2004. Delineation of a collapse of feature in a noisy environment using a multichannel surface wave technique, Geotechnique 54, No. 1, 17-27.

Xia, J., Miller, R. D., Park, C. B., Ivanov, J., Tian, G., Chen, C., 2004. Utilization of high-frequency Rayleigh waves in near-surface geophysics, The Leading Edge vol. 23.

Xia, J., Miller, Richard D., and Park, C. B., 1999. Estimation of near-surface wave velocity by inversion of Rayleigh waves. Geophysics, 64, 691-700.

Xia, J., Nyquist, J. E., Xu, Y., Roth, M. J .S., Miller, R. D., 2007. Feasibility of detecting near-surface feature with Rayleigh-wave diffraction, Journal of Applied Geophysics, Vol. 62, Issue 3, Page 244-253.

Xu, C.Q. and Butt S.D., 2006. Evaluation of MASW techniques to image steeply dipping cavities in laterally inhomogeneous terrain, Journal of Applied Geophysics, Volume 59, Issue 2, Pages 106-116.

Xu, C. Q., Butt, S. D., Ryall, P. J.C., 2008. Seismic Rayleigh wave method for localizing and imaging subsurface cavities in extensively exploited districts, Proceedings EEGS Annual Meeting 2008, pp. 662-678.

Xu Y., Xia, J. and Miller, R. D., 2005. Finite-difference modeling of high-frequency Rayleigh waves, Technical program with biographies, SEG, 75th Annual Meeting, Houston, TX (2005), pp. 1057–1060.

Yilmaz, Ö ., 1987. Seismic data processing, Society of Exploration Geophysics.

Yilmaz, Ö ., 2001. Seismic data analysis, Society of Exploration Geophysicists

Yuhr, L., Benson R. and Butler, D., 1993. Characterization of karst features using electromagnetics and microgravity: a strategic approach, Proceedings of the SAGEEP, San Diego, California.

Zhang, S. X., Chan, L. S, Xia, J., Tam, K. and Huang, R., 2002. Anisotropy induced dispersion behaviors of Rayleigh waves, SEG Int'l Exposition and 72nd Annual Meeting,Salt Lake City, Utah, October 6-11.

APPENDIX A 1D FOURIER & 2D FOURIER

Fourier Transform is based on Fourier series, by which a given time series can be expressed as the summation of infinite sinusoids of different frequencies. Hence, a time series can approximately be broken into a number of sinusoids of different frequencies, which is referred to as Fourier analysis. Figure A.1 is an example showing the summation of sinusoids of different frequencies ranging from 1 to 32 Hz with a constant phase delay -0.2 s yields a time series (top), or a signal. This is the process of synthesis.

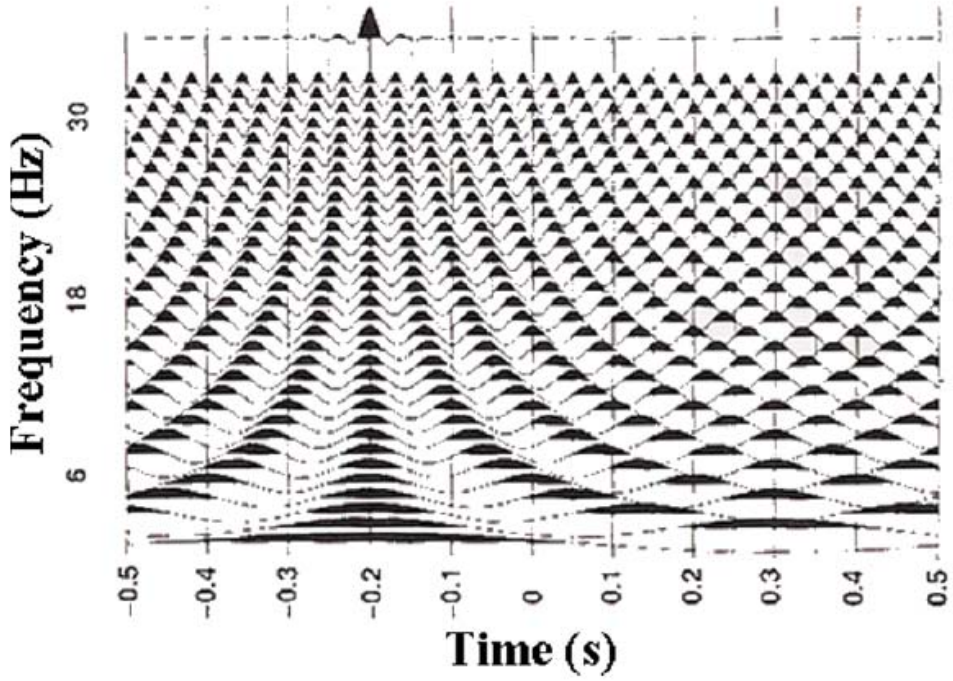

Figure A. 1 Summation of a discrete number of sinusoids of the same peak amplitude and with a -0.2 constant time delay yields a band limited symmetric wavelet (top)

The Fourier Transform *X(f)* of the continuous function *x(t)* with a single variable *t,* is defined by:

$$X(f) = \int_{-\infty}^{\infty} x(t) e^{-i 2 \pi f t} dt$$

and Inverse Fourier Transform (IFT) can be expressed as

$$x(t) = \int_{-\infty}^{\infty} X(f) e^{i 2 \pi f t} df$$

where $i^2 = -1$, e = natural exponent, which is defined:

$$e^{j\phi} = \cos(\phi) + j \sin(\phi)$$

Generally, $X(f)$ is a complex function and can be expressed as two other functions: frequency - amplitude spectrum function $A(f)$, and phase spectrum function $\phi(f)$:

$$X(f) = A(f) e^{i \phi(f)}$$

where:

$$A(f) = \| X(n) \| = \left[X_{real}^{\ 2}(f) + X_{imag}^{\ 2}(f) \right]^{1/2}$$

$$\phi(f) = \tan^{-1}\left[X_{imag}(f) / X_{real}(f) \right]$$

Considering two functions *x(t)* and *y(t)*, some basic theorems are listed in following table. These properties are very useful in various application of Fourier transform.

Fourier Transform Theorems

Operation	Time Domain	Frequency Domain
Addition	$x(t)+y(t)$	$X(f)+Y(f)$
Multiplication	$x(t)y(t)$	$X(f)*Y(f)$
Time Scale	$x(at)$	$X(f/a) / \|a\|$
Linearity	$ax(t)+by(t)$	$aX(f)+bY(f)$
Time Shift	$x(t-t_0)$	$exp(-i2pt_0f)X(f)$
Time Reversal	$x(-t)$	$X(-f)$
Convolution	$x(t)*y(t)$	$X(f)Y(f)$
Autocorrelation	$x(t)*x(t)$	$\|X(f)\|^2$
Derivative	$dx(t)/dt$	$ifX(f)$

The 2-D Fourier transform $P(k, f)$ of wave field $p(x, t)$ is given by

$$P(k,f) = \iint p(x,t) e^{(ikx - i2\pi ft)} dxdt$$

And $p(x, t)$ can be reconstructed from $P(k, f)$ by 2-D inverse Fourier transform:

$$p(x,t) = \iint P(k,f) e^{(-ikx + i2\pi ft)} dkdf$$

Essentially, 2-D Fourier transform is two steps of 1-D Fourier transform conducted respectively over the two variables *x* and *t*, or their Fourier pairs *k* and *f*.

Reference:

Yilmaz, O. Seismic data processing, SEG 1988.

APPENDIX B TRANSFORM TECHNIQUES: τ-P AND KGS METHOD

Slant-slowness (ω-p) transform

The use of the ω-p transform for the analysis of dispersive waves has been proposed by McMechan and Yedlin (1981) for the use of the slant stack to image dispersive waves in general. The basic concept is essentially the same as 2-D Fourier transform: to represent a wavefield of data as the superposition of a series of functions. Thus, as the Fourier transform is based on harmonics, the τ-p transform or slant stack represents the collected data as the superposition of straight-line events. Based on the concept, we have,

$$p = \frac{1}{V} \quad \text{and} \quad \tau = t - px \tag{B.1}$$

where V = wave propagation velocity.

According to the algorithm proposed by McMechan and Yedlin, the successive application of a slant stack and of a 1D discrete Fourier transform take the original data into the frequency-slowness domain, where dispersion curves can be identified.

The slant stack or τ-p transform is defined in such a way that it allows the decomposition of a wavefield into its plane components:

$$U(\tau, p) = \int_{-\infty}^{\infty} u(\tau + px, x)dx \tag{B.2}$$

where τ is the delay time and p is the ray parameter.

It is observed that the τ-p transform can be easily computed using the two-dimensional Fourier transform, i.e. the f-k spectrum (Buttkus, 2000). The frequency-wavenumber

representation $U(\omega,k)$ of a general wave field $u(x, t)$ is given by:

$$\begin{aligned} U(\omega,k) &= \iint u(x,t)e^{-i(\omega t-kx)}dxdt \\ &= \iint u(x,t)e^{-i\omega(t-px)}dxdt \end{aligned} \qquad \text{(B.3)}$$

Substituting $k = \omega/V = \omega p$ into (B.3) to get:

$$\begin{aligned} U(\omega,\omega p) &= \iint u(x,t)e^{-i\omega(t-px)}dxdt \\ &= \iint u(x,\tau+px)e^{-i\omega\tau}dxd\tau \end{aligned} \qquad \text{(B.4)}$$

Substituting Equation (B.2) into (B.4) to get,

$$U(\omega,k) = \iint U(\tau,p)e^{-i\omega\tau}d\tau$$

and its inverse Fourier transform is:

$$U(\tau,p) = \iint U(\omega,k)e^{-i\omega\tau}d\omega \qquad \text{(B.5)}$$

Equation (B.5) shows that the *t-p* transform can be determined by first transforming the wavefield $u(x,t)$ into the *f-k* domain and then calculating for each *p*-value the 1D inverse Fourier transform along a straight line $k = \omega p$.

The KGS Wavefield Transformation

The KGS wavefield transformation method provides images of dispersion curves directly from the recorded wavefields of a single shot gather. With this method, different modes are separated with higher resolution even if the shot gather consists of a relatively small number of traces collected over a limited offset range. The steps can be summarized as follows for a Multichannel Record (Shot Gather) $u(x,t)$:

1. FFT $u(x,t)$ along the time axis — $U(x,w)$:

$$U(x,w) = \int u(x,t) e^{iwt} dt . \qquad (1)$$

$U(x,w)$ can then be expressed as the multiplication of two separate terms:

$$U(x,w) = P(x,w)A(x,w), \qquad (2)$$

where $P(x,w)$ and $A(x,w)$ are phase and amplitude spectrum, respectively. In $U(x,w)$, each frequency component is completely separated from other frequencies and the arrival time information is preserved in the phase spectrum $P(x,w)$. Then, $P(x,w)$ contains all the information about dispersion properties, while $A(x,w)$ contains the information about all other properties such as attenuation and spherical divergence. Therefore, $U(x,w)$ can be expressed as follows:

$$U(x,w) = e^{-i\Phi x} A(x,w), \qquad (3)$$

where $\Phi = w / c_w$, w = frequency in radian, and c_w = phase velocity for frequency w.

3. Applying the following integral transformation to $U(x,w)$ in (3) we obtain $V(w,\phi)$:

$$\begin{aligned} V(w,\phi) &= \int e^{i\phi x} \left[U(x,w) \Big/ \left| U(x,w) \right| \right] dx \\ &= \int e^{-i(\Phi-\phi)x} \left[A(x,w) \Big/ \left| A(x,w) \right| \right] dx. \end{aligned} \qquad (4)$$

The integral transformation in (4) can be thought of as the summing over offset of wavefields of a frequency after applying offset-dependent phase shift determined for an assumed phase velocity c_w ($=w/\phi$) to the wavefields in (3). This process is identical to applying a slant stack to the equivalent time-domain expression of $U(x,w) \Big/ \left| U(x,w) \right|$ for a single frequency. To insure equal weighting during analysis of wavefields from different offsets, $U(x,w)$ is normalized with respect to offset compensating for the effects of attenuation and spherical divergence. Therefore, for a given w, $V(w,\phi)$ will have a maximum if

$$\phi = \Phi = w / c_w \qquad (5)$$

because $A(x,w)$ is both real and positive. For a value of ϕ where a peak of $V(w,\phi)$ occurs, the phase velocity c_w can be determined. If higher modes get appreciable amount of energy, there will be more than one peak.

Dispersion curves result from transforming of $V(w,\phi)$ to obtain $I(w,c_w)$ through changing the variables such that $c_w = w/\phi$. In the $I(w,c_w)$ wavefields, there will be peaks along the c_w-axis that satisfy (5) for a given *w*. The locus along these peaks over different values of *w* permits the images of dispersion curves to be constructed.

References

OZ Yilmaz, 1988. Seismic data processing, SEG.

McMechan G.A.and Yedlin M.J., 1981, Analysis of dispersive wave by wave field transformation, Geophysics, 46, 869-874

Buttkus B., 2000, Spectral analysis and filter theory in applied geophysics, Springer, Berlin, 667 pp

KGS Workshop, Spring 2005.

APPENDIX C COMPARISON OF WAVELETS IN MATLAB WAVELET TOOLBOX

This is a typical example to illustrate efficiency and accuracy of local event detection using different wavelets in Matlab toolbox.

The background is defined as summation of two harmonic functions as variable time t, respectively having a frequency of 500 Hz and 1000 Hz. That is:

$$x = \cos(2*\pi*f_1*t) + \cos(2*\pi*f_2*t)$$

Now, two events are given as two impulses which have a wide range of frequencies within a very short time 2.5 ms and the two impulses have a magnitude of 3.

To record these events, the sampling frequency will be set high enough, let's say 8000 Hz. The recorded signal can be displayed respectively in time domain and frequency domain (see figure in next page).

Only the background is displayed whereas it is difficult to tell the two events in both domains.

The question is: how can display the two events in the background?

The CWT calculation was used for different wavelets to yield a group of spectra, which were displayed for comparison and evaluation. Most wavelets are only good in either

time or frequency while only Complex Morlet wavelet yielded good localization in both domains.

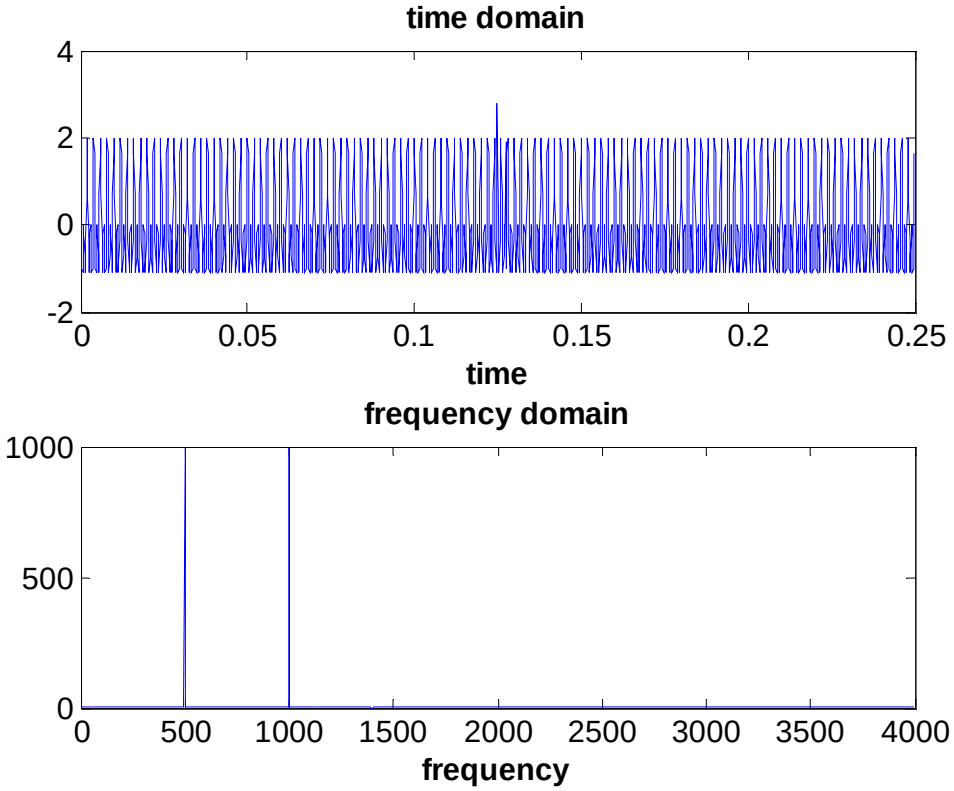

The following table lists most wavelets in Matlab toolbox.

SYMBLE	WAVELET NAME
haar	Haar
db	Daubechies
sym	Symlets
coif	Coiflets
bior	BiorSplines
rbio	ReverseBior
meyr	Meyer
dmey	DMeyer
gaus	Gaussian
mexh	Mexican_hat
morl	Morlet
cgau	Complex Gaussian
shan	Shannon
fbsp	Frequency B-Spline
cmor	Complex Morlet

The following two group figures show the effect of the different wavelets in localization of the two impulses from the surrounding.

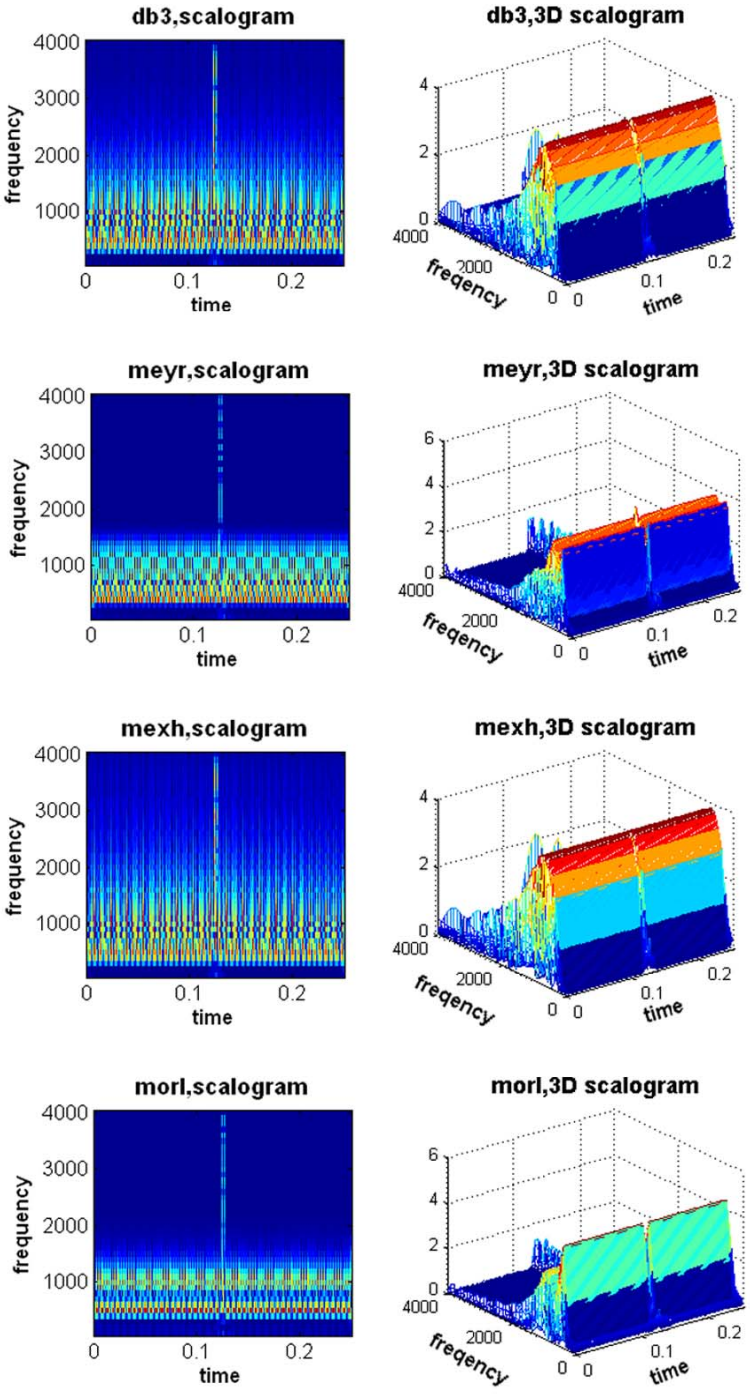

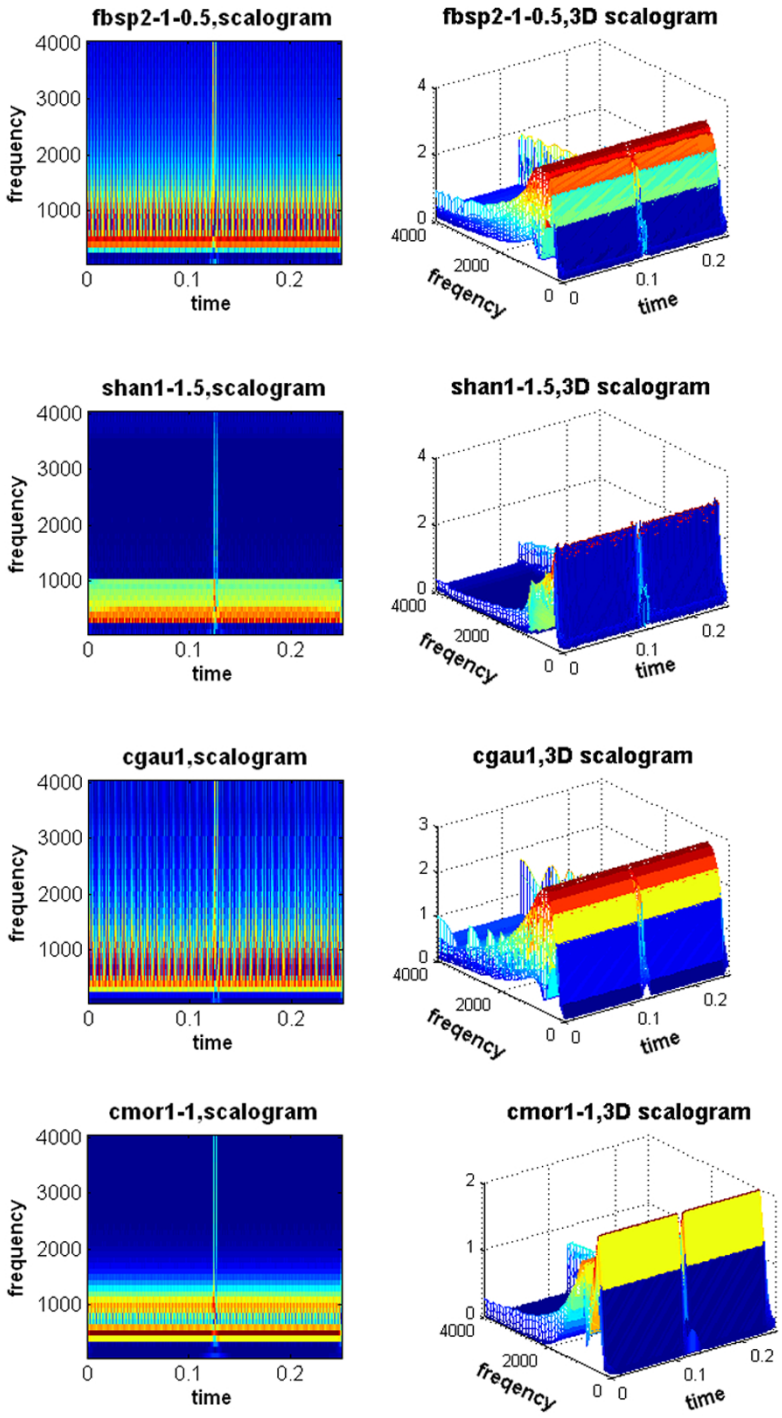

It is easy to see that Complex Morlet (cmorl) yielded the best localization both in time and frequency.

APPENDIX D MAIN ROGRAMS IN MATLAB

D1. Waveform Display

D1.1 dispvar.m

```
% this produce display in varied areas enhancing wavelets
clear;myt=clock;
close all;
clc
[dat,datpath]=uigetfile('*.txt;*.1st;*.frq;*.fkf;*.mut;*.cmb','Select a file:');
s=[datpath,'\' dat];
S=load(s);
[N,channel]=size(S);
offset=S(1,:);
spacing=abs(offset(5)-offset(4));%spacing=offset(5)
dx=offset(5)-offset(4);
tim=S(2:end,1);
%st=max(tim)*1e-3;
N=N-1;channel=channel-1;
S(1,:)=[];
xx=zeros(N,channel);
for m=1:channel
   xx(:,m)=S(:,m+1)/max(S(:,m+1))+m;
end
```

```
%plot(xx(10:end,1:channel),S(10:end,1),'k-');axis([0 channel+1 0 max(S(:,1))]);box off;axis ij;

%title(['Waveform of ',upper(dat)]);xlabel('m');ylabel('ms');grid off;

%for m=1:channel

%    c=m;

%    x=xx(:,m);y=S(:,1);

%    hold on;vari_area_dspl(x,y,c);

%end


figure;

plot(xx(:,1:channel),tim,'k-');set(gcf,'position',[20 70 400 500]);

%set(gcf,'position',[20 70 200 250])

grid off;axis([0 channel+1 0 round(length(tim)/3)]);box on;axis ij;

set (gca,'FontWeight','bold','Fontsize',12)

%title([upper(dat(1:6))],'fontweight','bold');

xlabel('m','Fontsize',14,'FontWeight','bold');ylabel('ms','Fontsize',14,'FontWeight','bold');


minx=min(offset(2:end));maxx=max(offset(2:end));

if dx>0

xv=minx:5:maxx;

set(gca,'XTick',xv-minx+1)

set(gca,'XTickLabel',xv)

else

xv=maxx:-5:minx;

set(gca,'XTick',1:5:maxx+1);
```

```
set(gca,'XTickLabel',xv);set(gca,'xdir','reverse')
end

for m=1:channel
    c=m;
    x=xx(1:round(length(tim)),m);y=tim(1:round(length(tim)));
    hold on;vari_area_dspl(x,y,c);
end
ylim([0 700])
set(gcf,'color',[1,1,1])
etime(clock,myt)

function vari_area_dspl(x,y,c)
% variable area filled and plot
% x,y are the prop,value pairs, c is a scalar
% x must me monotonic
% Permission needed to use the program from the author
% Users must refer to 'Programmed by Chao Qiang Xu, Mining Engineering of Dalhousie University'
n=1;
while n<round(length(x)*0.95);
   nstart=n;
   if x(nstart)<c
      while x(n)<c & n<round(length(x)*0.95)
         n=n+1;
      end
```

```
    else
        x(n)=c;
      while x(n)>=c & n<round(length(x)*0.95)
           n=n+1;
      end
      x(n)=c*(1-eps);
      area(x(nstart:n),y(nstart:n),'Facecolor',[0 0 0]);
    end
end
```

D.1.2 3Ddisplay.m

D2. Stacking

D 2.1 stack.m

```
% This program stacks several shot gathers of the same configuration to increase SNR
%shot gather for reference
[refgthr,datpath]=uigetfile('*.txt','Select a shot gather for reference:');
s=[datpath,'\' refgthr];
refmat=load(s);
tim=refmat(2:end,1);offset=refmat(1,2:end);
refseis=refmat(2:end,2:end);
 [nr nc]=size(refseis);
%define stack matrix
stackmat=refmat;%initial stack defination
```

```
%plot reference shot gather

clear s,clear refmat

plot(refseis(:,1)./max(refseis(:,1))+1,1:nr,'k-',...

   refseis(:,5)*2./max(refseis(:,5))+5,1:nr,'k-
',refseis(:,10)*5./max(refseis(:,10))+10,1:nr,'k-');

axis ij;title('Reference','fontweight','bold');grid on;ylim([0 150])%ylim([0 round(nr/4)])

legend('reference','Location','SouthEast');

%shot gather for stacking

stckyn='Yes';ysacc=2;

while ~isempty(stckyn)

  tstr=char({'Stacking shot  ',num2str(ysacc)})';

  [shotgthr,datpath]=uigetfile('*.txt',tstr);

  s=[datpath,'\' shotgthr];

  shotmat=load(s);clear s;

  shotseis=shotmat(2:end,2:end);

  hold on;

  tobestack=plot(shotseis(:,1)./max(shotseis(:,1))+1,1:nr,'r-',...

    shotseis(:,5)*2./max(shotseis(:,5))+5,1:nr,'r-
',shotseis(:,10)*5./max(shotseis(:,10))+10,1:nr,'r-');

  %axis ij;title('Reference','fontweight','bold');grid on;

  Hf=gcf;

  labtxt=uicontrol(Hf,'Style','text',...

                   'units','pixels',...

                   'Position',[10 3 80 15],...

                   'HorizontalAlignment','left',...

                   'String','Time Shift:','Fontweight','Bold');
```

```
yn='Yes';
while ~isempty(yn)
  Hu2=uicontrol(Hf,'Style','text',...
                'units','pixels',...
                'Position',[100 3 60 15],...
                'HorizontalAlignment','left','Style','edit');

  input('','s');
  figure(Hf)
  vshift=str2num(get(Hu2,'string'));
  [ntobestack bestckseis]=rfrefresh(nr,nc,refseis,shotseis,vshift,tobestack);
  tobestack=ntobestack;
  yn=questdlg('Keep shifting with this shot gather?');
  yn=findstr(yn,'Yes');
  figure(Hf)
end
stackmat(2:end,2:end)=stackmat(2:end,2:end)+bestckseis(:,:);
figure(Hf);hold on;
stkh=plot(stackmat(2:end,2)./max(stackmat(2:end,2))+1,1:nr,'b-',...
  stackmat(2:end,6)*2./max(stackmat(2:end,6))+5,1:nr,'b-
',stackmat(2:end,11)*5./max(stackmat(2:end,11))+10,1:nr,'b-');
stckyn=questdlg('Continue with another shot gather?');
stckyn=findstr(stckyn,'Yes');
delete(stkh),delete(tobestack);
figure(Hf)
```

```
  ysacc=ysacc+1;
end
hold on;
plot(stackmat(2:end,2)./max(stackmat(2:end,2))+1,1:nr,'b-',...
    stackmat(2:end,6)*2./max(stackmat(2:end,6))+5,1:nr,'b-
',stackmat(2:end,11)*5./max(stackmat(2:end,11))+10,1:nr,'b-');
f=[datpath,'\',refgthr(1:6) '.stk'];
dlmwrite(f,stackmat,'delimiter', ' ')
msgbox('Exit stacking.')
%set(Hu,'visible','off')  %  make sure text box disappears
%delete(Hu)
```

D3 Shot Line Combination

D3.1 combin.m

```
%combine common shot gather(CSG) to form 1m spacing survey
numshotstr=inputdlg('Shot Number for Combination:','');
numshot=str2num(char(numshotstr));
[firstshot,datpath]=uigetfile('*.txt','First Shot:');
s=[datpath,'\' firstshot];
firstmat=load(s);
tim=firstmat(2:end,1);offset=firstmat(1,2:end);
firstseis=firstmat(2:end,2:end); [nr1 nc1]=size(firstseis);
```

```
combseis=zeros(nr1,nc1*numshot); [nrcomb nccomb]=size(combseis);
combseis(:,1:numshot:nccomb-numshot+1)=firstseis(:,:);
for shotcount=2:numshot
   tstr=char({'Shot No ',num2str(shotcount)})';
   [shot,datpath]=uigetfile('*.txt',tstr);
   s=[datpath,'\' shot];
   shotmat=load(s);
   shotseis=shotmat(2:end,2:end);
   combseis(:,shotcount:numshot:nccomb-numshot+shotcount)=shotseis(:,:);
end
combmat=zeros(nrcomb+1,nccomb+1);
combmat(2:end,1)=tim;
combmat(1,2:end)=(0:nccomb-1)+offset(1);
combmat(2:end,2:end)=combseis;
f=[datpath,'\',firstshot(1:6) '.cmb'];
dlmwrite(f,combmat,'delimiter', ' ')
msgbox('Exit shot combination!')
```

D4 Filtering

D4.1 frqzfltr.m

```
%first perform filtering in frequency
clear;close all;
clc
```

```
 [dat,datpath]=uigetfile('*.txt;*.stk;*.1st;*.frq;*.fkf;*.mut;*.cmb','Select a file:');
s=[datpath,'\' dat];
S=load(s);
%S(2:10,2:end)=0;S(end-10:end,2:end)=0;
[N,channel]=size(S);
st=max(S(:,1))*1e-3;
fs=1/(S(5,1)-S(4,1))*1000;
x=zeros(N,channel);
xx=zeros(N,channel);
x(1,:)=S(1,:);x(:,1)=S(:,1);
xx(1,:)=S(1,:);xx(:,1)=S(:,1);
cutoff={'Cut-off frequency:'};
answer=inputdlg(cutoff,'');
ncut=char(answer(1));ncut=str2num(ncut);
[b,a]=butter(9,ncut/(fs/2));
x(2:end,2:end)=filtfilt(b,a,S(2:end,2:end));
for m=2:length(x)-50;
      x(m,2:end)=x(m,2:end)-mean(x(m:m+50,2:end));
end


%for m=2:channel;
%    y=fft(x(2:end,m));
%    compressy=y;
%    ind=find(abs(y)<0.05*mean(abs(y)));
%    compressy(ind)=zeros(1,length(ind));
```

```
%    x(2:end,m)=ifft(compressy);
%end

newf=[datpath,'\',dat(1:6) '.frq'];
dlmwrite(newf,x,'delimiter', ' ')
for m=2:channel
   xx(2:end,m)=x(2:end,m)*0.8/max(abs(x(2:end,m)))+m-1;
end
colordef white;
plot(xx(2:end,2:channel),xx(2:end,1),'k-');axis([0 channel 0 xx(N,1)/2]);box on;axis
ij;grid on;
title(['Waveform of  ',upper(dat(1:6)) ' lowpass filter']);
%for m=2:channel
%     c=m-1;
%      hold on;vari_area_dspl(xx(2:end,m),xx(2:end,1),c);
%end
```

D4.2 fkfilter.m

```
%fkfilter used to pick up most energy components
clear;close all;
clc
[dat,datpath]=uigetfile('*.txt;*.1st;*.frq;*.fkf;*.mut','Select a file:');
s=[datpath,'\' dat];
S=load(s);
[M,N]=size(S);
```

```
if ~isinteger(M);
  S(end,:)=[];% to make the record lengrh even in SubSeis
  [M,N]=size(S);
end
tim=S(:,1);S(:,1)=[];
spacing=S(1,:);S(1,:)=[];
delx=abs(spacing(10)-spacing(9));
st=max(tim)*1e-3;
T=linspace(0,st,M-1)';delt=T(5)-T(4);%scanning period;
m=M-1;n=N-1;


%[x,y] = meshgrid(hamming(n),hamming(m));  tracemask = x.*y; clear x; clear y;
%traces = tracemask.*S;clear S; % smooth out some rough edges for ffting later, applied
twice.


traces=S;clear S;% instead of two lines above


M = pow2(nextpow2(m)); N = pow2(nextpow2(n));
fnyq = 1/(2*delt); delf = 2*fnyq/M;
freqs = -fnyq:delf:fnyq - delf;
knyq = 1/(2*delx); delk = 2*knyq/N;
ks = -knyq:delk:knyq-delk;
newtraces1 = zeros(M,N);
indxy = [(M-m)/2+1  m+(M-m)/2  (N-n)/2+1  n+(N-n)/2 ]; % Index corners of data
within newtraces
newtraces1((M-m)/2+1:m+(M-m)/2,(N-n)/2+1:n+(N-n)/2) = traces;
```

```
clear traces

%imagesc(newtraces1);

z=fft2(newtraces1);z=fliplr(z);

%z = fft(newtraces1);z=z';z=fft(z);z=z';

z = fftshift(z);

figure;set(gcf,'position',[20 70 1000 650])

imagesc(ks,freqs,abs(z));colormap(jet);ylim([0 100]);grid off;

hold on;pcolor(ks,freqs,double(abs(z)));

shading
interp;colormap(jet);set(gca,'YDir','normal');xlim([min(ks),max(ks)]);ylim([freqs(M/2+1)
,100])

ylabel('frequency (Hz)'); xlabel('Spatial Wavenumber (radians/m)')

title(['Zoom if necessary then press any key to begin picking, end picking by double
click'],'FontWeight','bold')

pause


[mask,xi,yi] = roipoly;

mask(1:M/2,1:N) = fliplr(flipud(mask(M/2+1:M,1:N)));

% mask(M/2+1:M,1:N) = fliplr(flipud(mask(1:M/2,1:N)));

mask=single(mask);

kernel = fspecial('average',[30 7]);  %Smooth the edges of the filter

mask = conv2(mask,kernel,'same');


z = mask.*z;

z = fftshift(z); %z=z';z=ifft(z);z=z';newtraces = real(ifft(z));

z=fliplr(z);newtraces = real(ifft2(z));
```

```
newtraces = newtraces(indxy(1):indxy(2),indxy(3):indxy(4));
%figure;imagesc(newtraces)
newtraces=[spacing' newtraces']';
newtraces=[tim newtraces];

f=[datpath,'\',dat(1:6) '.fkf'];
dlmwrite(f,newtraces,'delimiter', ' ')
close all;
msgbox('Exit fkfilter pick.')
```

D4.3 xtfilter.m

```
%first perform filtering in x-t domain
clear;close all;
clc
[dat,datpath]=uigetfile('*.txt;*.stk;*.1st;*.frq;*.fkf;*.mut;*.cmb','Select a file:');
s=[datpath,'\' dat];
S=load(s);
%S(2:10,2:end)=0;S(end-10:end,2:end)=0;
[N,channel]=size(S);st=max(S(:,1))*1e-3;fs=1/(S(5,1)-S(4,1))*1000;
x=zeros(N,channel);
xx=zeros(N,channel);
x(1,:)=S(1,:);x(:,1)=S(:,1);
xx(1,:)=S(1,:);xx(:,1)=S(:,1);
cutoff={'Cut-off frequency:'};
answer=inputdlg(cutoff,'');
```

```
ncut=char(answer(1));ncut=str2num(ncut);
[b,a]=butter(9,ncut/(fs/2));
x(2:end,2:end)=filtfilt(b,a,S(2:end,2:end));
for m=2:length(x)-50;
      x(m,2:end)=x(m,2:end)-mean(x(m:m+50,2:end));
end
%for m=2:channel;
%   y=fft(x(2:end,m));%   compressy=y;
%   ind=find(abs(y)<0.05*mean(abs(y)));
%   compressy(ind)=zeros(1,length(ind));
%   x(2:end,m)=ifft(compressy);
%end
newf=[datpath,'\',dat(1:6) '.frq'];
dlmwrite(newf,x,'delimiter', ' ')
for m=2:channel
   xx(2:end,m)=x(2:end,m)*0.8/max(abs(x(2:end,m)))+m-1;
end
colordef white;
plot(xx(2:end,2:channel),xx(2:end,1),'k-');axis([0 channel 0 xx(N,1)/2]);box on;axis
ij;grid on;
title(['Waveform of  ',upper(dat(1:6)) ' lowpass filter']);
%for m=2:channel
%    c=m-1;
%     hold on;vari_area_dspl(xx(2:end,m),xx(2:end,1),c);
%end
```

D5 SV Imaging

D5.1 imgSV.m

```
%This program  applies to waveforms containing majority of Rayleigh waves and produces  shear velocity field mapping

% complex Gaussian wavelet proved to an suitable wavelet basis used for time delay estimation

clear;close all;

myt=clock;

clc

[dat,datpath]=uigetfile('*.txt;*.frq;*.fkf','Select a file:');

s=[datpath,'\' dat];

S=load(s);

offset=S(1,:);

scacing=abs(offset(5)-offset(4));%spacing=offset(5)

dx=offset(5)-offset(4);

[N,nchannel]=size(S);

tim=S(2:end,1)*1e-3;

nsection=nchannel-2;% get out of time column.

st=max(S(:,1))*1e-3;

N=N-1;

T=linspace(0,st,N)';

t=T(4)-T(3);%scanning period;

fs=1/t;
```

```
%lat_answer=inputdlg('Later Varation Consideration (Y/N)?','');

%latyn=char(lat_answer);

%wname_str={'cgau1','cgau2','cgau3','cgau4','cgau5','cmor1-1.5','cmor1-1','cmor1-
0.5','cmor1-0.1',...

%    'shan1-1.5','shan1-1','shan1-0.5','shan1-0.1','shan2-3','fbsp2-1-0.5'};

%[wname_s,ok] = listdlg('PromptString','Select a complex wavelet:',...

%                'SelectionMode','single',...

%                'ListString',wname_str);

%switch wname_s

%    case 1

%       wname='cgau1';%Q=0.2880;

%    case 2

%      wname='cgau2';%Q=0.4160;

%    case 3

%        wname='cgau3';%Q=0.5120;

%    case 4

%        wname='cgau4';%Q=0.5120;

%    case 5

%        wname='cgau5';%Q=0.6000;

%    case 6

%        wname='cmor1-1.5';%Q=1.5040;

%    case 7

       wname='cmor1-1'; %Q=0.9920;

%    case 8

%        wname='cmor1-0.5';%Q=0.5120;

%    case 9
```

```
%       wname='cmor1-0.1';%Q=0.128;
%    case 10
%       wname='shan1-1.5';%Q=1.0240;
%    case 11
%       wname='shan1-1';%Q=0.5120;
%    case 12
%       wname='shan1-0.5';%Q=0.0320;
%    case 13
%       wname='shan1-0.1';%Q=0.3840;
%    case 14
%       wname='shan2-3';%Q=2.0160;
%    case 15
%       wname='fbsp2-1-0.5';%Q=0.5120;
%end
Q = centfrq(wname);
ncwt=64;
v=[];thita=[];
FKcheck(S);set(gcf,'position',[20 70 1000 650]);ylim([5 100])
%simplezoom;
[xw,yf,button] = ginput(2);
freqzlower=min(yf);
freqzupper=max(yf);
freq=linspace(freqzlower,freqzupper,ncwt);
scale=Q*fs./freq;
vh=VcheckForSVFM(S);
```

```
prmpinp={'maximum velocity limit:'};
answer=inputdlg(prmpinp);
vh=str2num(char(answer));
%vh=vh*1.2;% to be shear velocity
error=1;
for m=2:nchannel-1;
   x=S(:,m);y=S(:,m+1);
   c1 = cwt(x,scale,wname);
   c2 = cwt(y,scale,wname);
   amp1=abs(c1);amp2=abs(c2);amp1(:,end-200:end)=0; amp1(:,1:100)=0;
   thita1=angle(c1);thita2=angle(c2);
       [maxa1,indN1]=max(amp1');% over frequency or scale
       [maxa2,indN2]=max(amp2');
       tg1=tim(indN1);tg2=tim(indN2);tph2=ones(length(scale),1);

       for nt=1:length(scale);
          tmpthita1=thita1(nt,:);
          timp1=find(tim==tg1(nt));          thi1=tmpthita1(timp1);
          tmpthita2=thita2(nt,:);
          timp2=find(tim==tg2(nt));          thi2=tmpthita2(timp2);

          if thi1<thi2;
             timpd=min(find(tmpthita2(timp2:end)<thi1))+timp2-1;
             if ~isempty(timpd)
                tph2(nt)=interp1(tmpthita2(timp2:timpd),tim(timp2:timpd),thi1,'spline');
```

```
            else
                dn=find(min(tmpthita2(indN2(nt):end)));
                %if isempty(dn),dn=0;end
                tph2(nt)=tim(indN2(nt))+t*dn;
            end
        end
        if thi1==thi2;
            tph2(nt)=tg2(nt);
        end
        if thi1>thi2;
            timpb=max(find(tmpthita2(timp2:-1:timp1)>thi1));
            if ~isempty(timpb)
                tph2(nt)=interp1(tmpthita2(timpb:timp2),tim(timpb:timp2),thi1,'spline');
            else

dn=find(max(tmpthita2(min(indN1(nt),indN2(nt)):min(indN1(nt),indN2(nt)))));
                if isempty(dn),dn=0;end
                tph2(nt)=tim(indN1(nt))+t*dn;
            end
        end
        dtph(nt)=tph2(nt)-tg1(nt);
    end
    dtph((find(dtph==0)))=eps;
    v(:,m-1)=1.1*spacing./abs(dtph);
    lam(:,m-1)=0.5*v(:,m-1)./freq';
end
```

```
wavel=linspace(spacing/pi,spacing*nsection/pi,length(scale))';%pi,length(scale))'
close all;
for nloop=4:5
for i=1:nsection
   %lamtemp=(lam(:,i)-mean(lam(:,i)))./std(lam(:,i));
   %a= polyfit(lamtemp,v(:,i),2);v1(:,i)=polyval(a,wavel);
   [a err mu]=polyfit(lam(:,i),v(:,i),3);
   [v1(:,i),delerr(:,i)]=polyval(a,wavel,err,mu);
   v1(find(isnan(v1(:,i))))=0;
   v1(find(v1(:,i)<error),i)=0;
   v1(find(v1(:,i)>vh),i)=vh;
end
%if latyn=='N'|latyn=='n'
%  for i=1:length(scale)
%   v1(i,:)=smooth(v1(i,:),nsection,'moving');
% end
%else
  for i=1:length(scale)
    v1(i,:)=smooth(v1(i,:),round(nsection/nloop),'loess');
   end
%end

yval=wavel;%assume maximum wavelength is 15 metre,depth=1/3 wavlength
if dx>0
   xval=offset(2:end-1)+0.5;
```

```
else
    xval=offset(2:end-1)-0.5;
end
vc=linspace(0,max(max(v1)),200)';%global outer limit for velocity contour
savefile = [datpath, dat(1:4) num2str(nloop)-3];
save(savefile, 'xval','yval','v1')
figure('Color',[1 1 1]);colordef white;set(gcf,'position',[20 540 800 180]);
[c,h]=contourf(xval,yval,v1,vc);
xlim([min(xval) max(xval)]);ylim([min(yval) max(yval)])
shading flat;
colormap(jet);
set(gca,'YDir','reverse')
colorbar%gray plot
xlabel('Dist(m)');ylabel('Depth(m)');title(['Shear-Velocity Mapping'],'FontWeight','bold');
end
%3D
%figure('Color',[1 1 1]);surfc(xval,yval,v1);view(2);set(gcf,'position',[20 360 800 180]);
%xlabel('STN');ylabel('Depth(m)');title(['Shear-Velocity Mapping'],'FontWeight','bold');
%xlim([min(xval) max(xval)]);ylim([min(yval) max(yval)]);
%set(gca,'YDir','reverse')
%shading interp;colorbar
%enlwavel=linspace(min(wavel),max(wavel),500);dy1=enlwavel(3)-enlwavel(1);
%enlx=linspace(1,nsection,500);dx1=enlx(3)-enlx(1);
%enlv1=interp1(wavel,v1,enlwavel,'spline');
%v2=interp1(1:nsection,enlv1',enlx,'spline');v2=v2';
```

```
%dvhv=diff(diff(v2)')';[nr1 ncl1]=size(dvhv);

%scdhv=diff(diff(dvhv)')';[nr2 ncl2]=size(scdhv);

%xd1=linspace(1,nsection,ncl1);wavel1=linspace(min(wavel),max(wavel),nr1);

%figure;surfc(xd1,wavel1,dvhv);set(gcf,'position',[20 180 800 200]);

%xlim([min(xval) max(xval)]);ylim([min(yval) max(yval)]);colorbar;view(2)

%xlabel('STN');ylabel('Depth(m)');title(['Shear-Velocity Changing in Depth and
Offset'],'FontWeight','bold');

%grid off;shading interp;set(gca,'ydir','reverse');

%xd2=linspace(1,nsection,ncl2);wavel2=linspace(min(wavel),max(wavel),nr2);

%figure;surfc(xd2,wavel2,scdhv);set(gcf,'position',[20 0 800 200]);

%xlim([min(xval) max(xval)]);ylim([min(yval) max(yval)]);colorbar;view(2)

%xlabel('STN');ylabel('Depth(m)');title(['Shear-Velocity Changing (2nd order) in Depth
and Offset'],'FontWeight','bold');

%grid off;shading interp;set(gca,'ydir','reverse');

etime(clock,myt)




%END OF CODE
```